

THESIS

EVALUATION OF FLOW AND SCALAR TRANSPORT CHARACTERISTICS OF
SMALL PUBLIC DRINKING WATER DISINFECTION SYSTEMS USING
COMPUTATIONAL FLUID DYNAMICS

Submitted by

Jordan M. Wilson

Department of Civil and Environmental Engineering

In partial fulfillment of the requirements

For the Degree of Master of Science

Colorado State University

Fort Collins, Colorado

Spring 2011

Master's Committee:

Advisor: S. Karan Venayagamoorthy

Timothy K. Gates

S. Ranil Wickramasinghe

ABSTRACT

EVALUATION OF FLOW AND SCALAR TRANSPORT CHARACTERISTICS OF SMALL PUBLIC DRINKING WATER DISINFECTION SYSTEMS USING COMPUTATIONAL FLUID DYNAMICS

This study focuses on the evaluation of flow and scalar transport characteristics of small disinfection systems, primarily through computational fluid dynamics (CFD) as well as physical conservative tracer studies. Original research was performed on a pipe loop, series of pressurized tanks, and two separate open surface tank contact systems and a case study was performed on a baffled tank system. The flow dynamics for each of these respective disinfection systems were evaluated using CFD. The flow dynamics govern the transport of any quantity (e.g., a passive scalar, conservative tracer, or chlorine-containing species) through the system visualized through plotting the effluent concentration (e.g., passive scalar for computational models and conservative tracer for physical experiments) through time forming what is commonly referred to as a residence time distribution (RTD), or flow-through, curve. Physical experiments provided validation for the CFD models that give a more complete view of hydraulic efficiency thus overcoming the common "black-box" approach to contact tank design using only the theoretical detention time (TDT) (defined as the system volume V divided by the volumetric flow rate Q). The differing geometries of contact tank systems yield

significantly different flow paths with varying degrees of separation, recirculation, inlet and outlet effects, and wall effects prompting the need for the evaluation of hydraulic efficiency to be unique to the system. Yet current practice evaluates the hydraulic efficiency of disinfection contact tank systems based on the *TDT* and the rising limb of the RTD curve, designated by the United States Environmental Protection Agency (USEPA) as baffle factor (*BF*).

Research presented in this study using CFD models and physical tracer studies shows that evaluation methods based upon *TDT* tend to overestimate, severely in some instances, the actual hydraulic efficiency as obtained from the systems' flow and scalar transport dynamics and subsequent RTD curves. The main objectives of this study were to determine the systems' respective hydraulic efficiencies and to analyze an alternative measure of hydraulic efficiency, the ratio t_{10}/t_{90} , where t_{10} and t_{90} are the time taken for 10 and 90 percent of the input concentration to be observed at the outlet of a system. The pipe loop system was dominated by advection and thus showed little variance in the values of *BF* and t_{10}/t_{90} . Analysis of the series of pressurized tank systems showed significant regions of turbulent mixing and recirculation corresponding to a system that was much less efficient than the pipe loop system. *BF* values for the pressurized tank systems were nearly 100 percent greater than t_{10}/t_{90} values as a result of a system behavior further from plug flow. The open surface tank systems exhibited the most uneven flow paths and lowest efficiencies seen in this study with *BF* and t_{10}/t_{90} values differing by at least 100 percent. These systems exhibited significant degrees of short-circuiting and recirculation largely due to their inlet and outlet configurations. Finally, the baffled tank system showed an increase in system efficiency with the number of baffles

(e.g., increase in advective forces) and a corresponding decrease in the variance between BF and t_{10}/t_{90} values.

Overall, the research presented in this thesis provides an extensive evaluation for the flow and scalar characteristics of the described small public drinking water disinfection systems allowing for the development of t_{10}/t_{90} as a more representative evaluation of hydraulic efficiency

ACKNOWLEDGMENTS

Foremost, I would like to recognize my advisor, Dr. Karan Venayagamoorthy for his influence in my decision to attend Colorado State University for my graduate studies without whom this thesis would not exist. I also appreciate the challenges and encouragement he has presented over the past three semesters making me a better researcher, and more importantly a better person. I also give special acknowledgement to my committee members, Dr. Timothy Gates and Dr. Ranil Wickramasinghe, for their insights and support.

Grateful acknowledgement is given to the Colorado Department of Public Health and Environment (CDPHE) Water Quality Control Division, USA (Program Engineers: Tyson Ingels, Melanie Criswell, Gordon Whittaker and Sharon Williams) for their support on this project and to Fort Collins Water Treatment Facility (Water Production Manager: Lisa Voytko , and Ken Morrison) for the use of their pilot pipe loop facility.

I would also like to thank the members of my research group, Qing Xu, Hyeyun Ku, and Zach Elliot, for their support. I especially thank Qing Xu for the use of her data and figures for the baffled tank system. I also thank Taylor Barnett and Tim Sellers for their exceptional work running many of the physical tracer studies over the summer and for their development of the hydraulic model for the series of pressurized tank system.

Finally, I would like to give special thanks to my family for their support in moving away from home for the first time and pursuing graduate studies. Without my

parents' sacrifices over the years to support my academic endeavors, I can truly say that I would not be pursuing a graduate degree. Finally, I am deeply indebted to Paige Griffin for her never-ending support and encouragement over the past three semesters.

TABLE OF CONTENTS

CHAPTER 1: INTRODUCTION	1
1.1 Project Scope	7
1.2 Organization of Thesis	9
1.3 New Contributions	10
1.4 Research Publications	11
1.5 Units	11
CHAPTER 2: LITERATURE REVIEW	12
2.1 Small Public Water Systems	12
2.2 Contact Tank Design	13
2.3 Disinfection and Log Inactivation	14
2.4 Tracer Studies	16
2.4.1 Pulse Input Tracer Study	17
2.4.2 Step Input Tracer Study	18
2.5 Hydraulic Efficiency and Residence Time Distribution (RTD) Curves	20
2.6 Flow Modeling and Computational Fluid Dynamics	24
2.7 Turbulence and Turbulence Models	26
2.7.1 Direct Numerical Simulations (DNS)	27
2.7.2 Large Eddy Simulations (LES)	28
2.7.3 Reynolds-Averaged Navier-Stokes (RANS) Equations	28
2.7.4 Two-Equation Turbulence Models	30
2.8 Scalar Transport Modeling	31
2.9 Modeling Software	32
2.9.1 Workbench	32
2.9.2 FLUENT	33
CHAPTER 3: EVALUATION OF FLOW AND SCALAR TRANSPORT CHARACTERISTICS	34
3.1 Introduction	34

3.2 CFD Modeling	35
3.2.1 Pipe Loop System Configuration.....	35
3.2.1.1 Pipe Loop System Computational Model Setup.....	36
3.2.1.2 Pipe Loop System FLUENT Setup.....	37
3.2.1.3 Pipe Loop System Results and Conclusions.....	39
3.2.2 Pressurized Tank System Configuration.....	43
3.2.2.1 Pressurized Tank System Computational Model Setup.....	45
3.2.2.2 Pressurized Tank System FLUENT Setup.....	46
3.2.2.3 Pressurized Tank System Results and Conclusions.....	46
3.2.3 Open Surface Tank System Configuration	58
3.2.3.1 Open Surface Tank System Computational Model Setup	59
3.2.3.2 Open Surface Tank System FLUENT Setup	60
3.2.3.3 Open Surface Tank System Results and Conclusions	61
3.2.4 Baffled Tank System.....	74
3.2.4.1 Baffled Tank System Configuration.	75
3.2.4.2 Baffled Tank System FLUENT Setup	75
3.2.4.3 Baffled Tank System Results and Conclusions	76
3.3 Conclusions.....	78
CHAPTER 4: EVALUATION OF HYDRAULIC EFFICIENCY OF DISINFECTION SYSTEMS BASES ON RESIDENCE TIME DISTRIBUTION CURVES.....	81
4.1 Introduction.....	81
4.2 Experimental Methods	83
4.3 Comparison of scalar transport results for CFD models and physical tracer studies	85
4.3.1 Pipe Loop System	85
4.3.2 Pressurized Tank System	86
4.3.3 Open Surface Tank Systems	91
4.3.4 Baffled Tank System.....	94
4.4 Discussion.....	96
CHAPTER 5: SUMMARY AND CONCLUSIONS	99
5.1 Summary of Research.....	99
5.2 Major Conclusions	100
5.3 Recommendations.....	101
REFERENCES	102
APPENDIX A.....	105

APPENDIX B	109
APPENDIX C	116
APPENDIX D	124
APPENDIX E	131
APPENDIX F	143
APPENDIX G	149
APPENDIX H	155

CHAPTER 1: INTRODUCTION

Civilizations have always situated themselves near water sources because of its necessity for life. Lacking any knowledge of waterborne illnesses, people generally consumed water in its raw state. Water treatment processes originated around 4000 B.C. when Greeks began using rudimentary charcoal filters, exposure to sunlight, boiling, and straining to improve taste and odor. Egyptians followed suit by using alum to remove suspended particles around 1500 B.C. (HDR 1999). Around 300 B.C. centralized water distribution systems began to appear in Roman and Jordanian cities (Hansen and Ortloff 2005). As civilizations developed and spread throughout the eastern and western worlds, they continued to only improve the aesthetic quality of water lacking knowledge about the biological and chemical contaminants. The nineteenth century saw numerous epidemics (e.g., cholera and typhoid) which were eventually linked to water sources (Borchardt & Walton 1971 and Letterman 1999). As a result, London passed the first law requiring water filtration in 1852 (Borchardt & Walton 1971) but scientific proof would not be offered on these waterborne illnesses until later in the century (e.g., Pasteur's particulate germ theory of disease) (Letterman 1999).

The United States followed a similar pattern of developing water distribution systems that only treated the aesthetic qualities of water. By 1900, over 3000 water supply systems were estimated in the country leading to a similar spread of epidemics seen during the nineteenth century in London. It was not until 1912 that the first water-

related sanitation law was enacted prohibiting the use of a common cup on carriers of interstate commerce, such as trains (McDermott 1973). Shortly thereafter in 1914, the United States Public Health Service Standards (USPHS), originally a part of the Department of the Treasury, issued the first drinking water standards limiting the e-coli and total bacteria allowed in drinking water on interstate carriers (Borchardt & Walton 1971). The USPHS standards were eventually expanded to municipal supply facilities and updated several times until the establishment of the Safe Drinking Water Act (SDWA) in 1974.

The SDWA completely changed the monitoring of drinking water systems through forming a cooperative between local, state, and federal agencies covering chemical and microbial contaminants. Under this new legislation, the United States Environmental Protection Agency (USEPA) established national drinking water standards, conducted research, and oversaw the implementation of the SDWA. The first set of National Interim Primary Drinking Water Regulations (NIPDWRs) was promulgated in 1975 and took effect in 1977. Over the years, numerous amendments have been made to the SDWA and NIPDWRs in order to regulate differing or new contaminants, contaminant levels, sources, and other water quality issues (Letterman 1999).

One such addition that the USEPA has made is the Ground Water Rule which gives stricter regulatory oversight for ground water systems (USEPA 2009). Systems that can demonstrate 4-log inactivation of viruses are exempt from the triggered source water monitoring; however, systems with susceptible groundwater sources and new systems

will be required to demonstrate 4-log inactivation of viruses or they will have to install a system upgrade with an approved design.

Currently, the Water Quality Control Division of the Colorado Department of Public Health and Environment (CDPHE) determines the disinfection log inactivation using the protocol described in the *Long Term 1 Enhanced Surface Water Treatment Rule (LT1ESWTR) Disinfection Profiling and Benchmarking Technical Guidance Manual* (USEPA 2003). The Water Quality Control Division is responsible for monitoring and reporting the quality of Colorado's waters including water pollution issues, surface and groundwater quality, and ensuring public water systems provide safe drinking water. The USEPA document has a general baffle factor (*BF*) description chart (see Table 1 below) and some example baffling configurations (seen in Figures 1.1, 1.2, and 1.3). Baffle factor is the ratio of t_{10} , that is the time for 10 percent of the inlet concentration to be observed at the outlet, to theoretical detention (or retention) time (*TDT*) defined as the system volume V divided by the flow rate Q .

Table 1.1 Baffling Factors from LT1ESWTR Disinfection Profiling and Benchmarking Technical Guidance Manual (USEPA 2003).

Baffling Condition	<i>BF</i>	Baffling Description
Unbaffled (mixed flow)	0.1	None, agitated basin, very low length to width ratio, high inlet and outlet flow velocities.
Poor	0.3	Single or multiple unbaffled inlets and outlets, no intra-basin baffles.
Average	0.5	Baffled inlet or outlet with some intra-basin baffles.
Superior	0.7	Perforated inlet baffle, serpentine or perforated intra basin baffles, outlet weir or perforated launders.
Perfect (plug flow)	1.0	Very high length to width ratio (pipeline flow), perforated inlet, outlet, and intra-basin baffles.

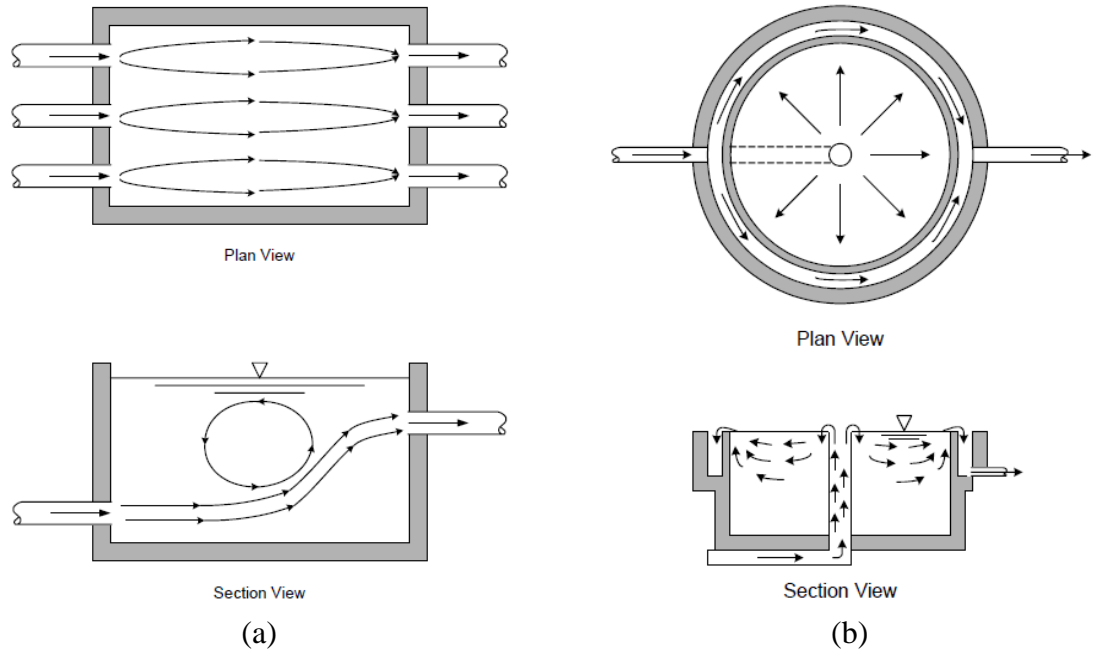


Figure 1.1 Poor Baffling Conditions for (a) rectangular and (b) circular contact basins (USEPA 2003).

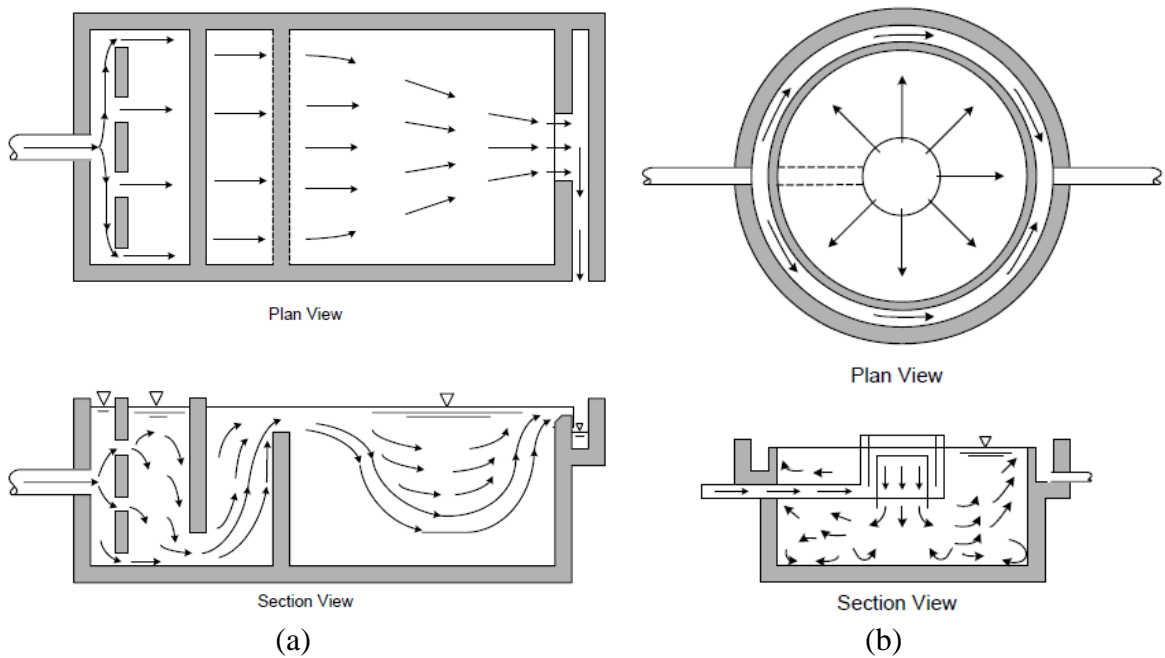


Figure 1.2 Average baffling conditions for (a) rectangular and (b) circular contact basins (USEPA 2003).

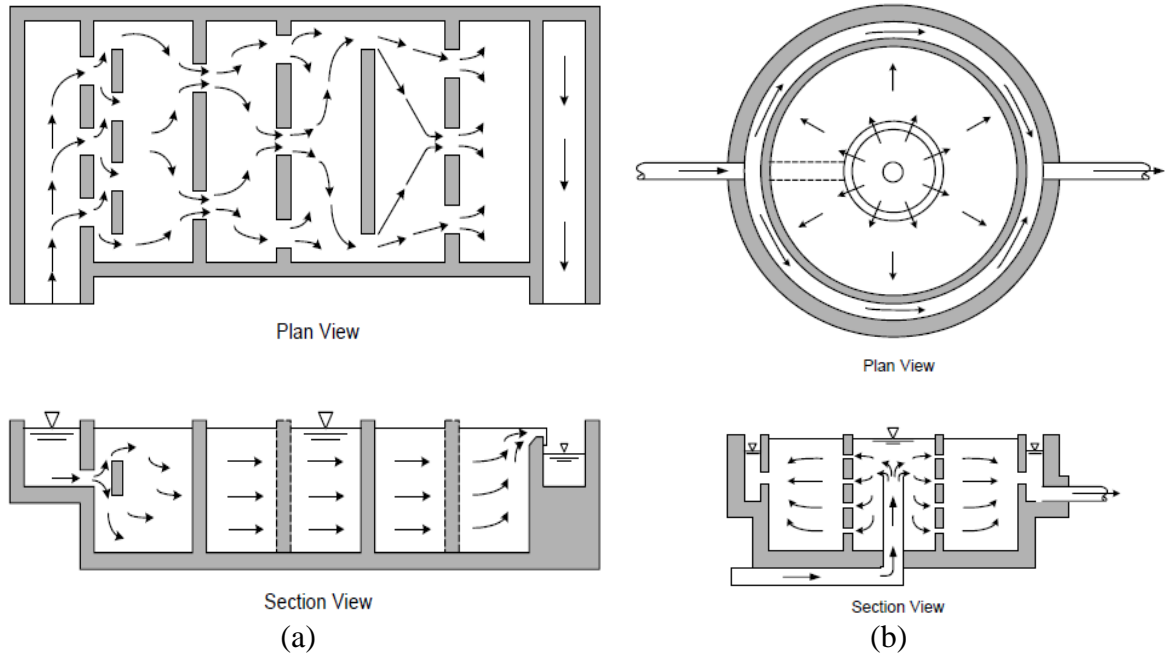


Figure 1.3 Superior baffling conditions for (a) rectangular and (b) circular contact basins (USEPA 2003).

The contact basin baffle factor, BF , is a potentially imprecise factor in the log inactivation calculation mainly due to the lack of financial and technical resources allocated for these small systems. The USEPA baffling conditions also have limited applicability for the contact tanks configurations utilized by many small public water systems in Colorado and do not address multiple small tanks in series or large open surface tanks. Figure 1.4 shows a schematic for an example small public water system.

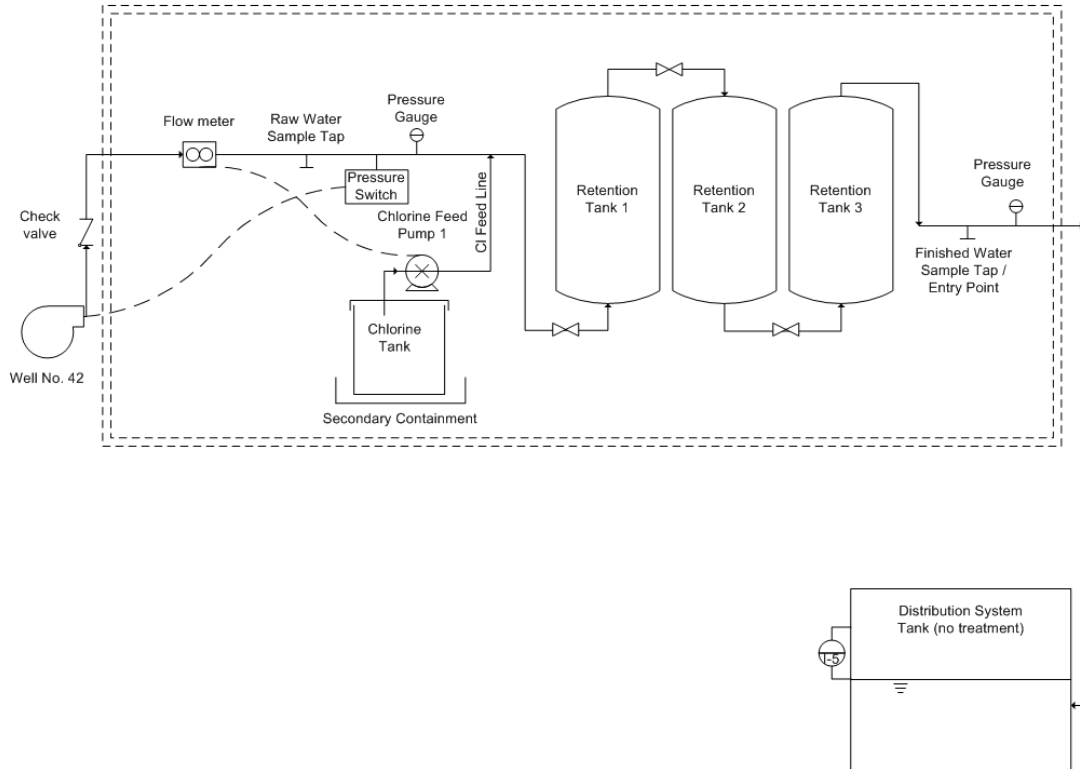


Figure 1.4 Schematic for an example small public water system

Furthermore, *BF* is an inherently flawed parameter that is commonly accepted as a system's hydraulic mixing efficiency (discussed extensively in chapter 4). In brief, the hydraulic mixing efficiency describes a system's effectiveness at disinfecting a water supply through providing an adequate contact time for the applied disinfectant to neutralize contaminants. While this definition of efficiency is not thought of in the traditional engineering sense, it is not the purpose of this thesis to challenge the convention used in the disinfection community.

Traditionally, contact tank design has taken a black box approach wherein *TDT* was evaluated the same for any and every system. Thus, the volume and flow rates of a pipe loop contactor (e.g., see Figures 3.1 and 3.2) and an unbaffled tank can be arranged

such that both have the exact same *TDT* but even a basic understanding of fluid dynamics shows that the flow differs significantly between these two systems. Most contact tanks have uneven flow paths with regions of recirculation or stagnation, known as dead zones (Wang & Falconer 1998). Dead zones rely on the much slower process of diffusion to distribute a disinfectant, causing particles in the contact tank to reside longer than the *TDT*. The problem with the *TDT* formulation is that this value is a prediction based on idealized plug flow conditions rather than the actual flow dynamics of the tank. Plug flow defines a fluid that moves in a constant plug with no mixing. The further the flow in the tank departs from plug flow (e.g. the more recirculation, turbulence, and stagnation fluid particles encounter), the further the actual detention time is from the *TDT* (Kothandaraman *et al.* 1973).

In recent years, the proliferation of computational fluid dynamics (CFD) has allowed a more insightful approach to disinfection system design and analysis. Research performed on a number of small public water system prototypes shows that a true measure of hydraulic efficiency must include the complete flow dynamics of the system which dictate a tracer's concentration from the inlet to outlet through time (Stamou & Noutsopoulos 1994) and can be depicted through use of a residence time distribution (RTD), or flow through (FTC), curves.

1.1 Project Scope

The majority of work presented in this study represents the second phase of a four phase project for the Water Quality Control Division of CDPHE. The first phase of this project was largely completed by Qing Xu for her Master's thesis entitled *Internal*

Hydraulics of Baffled Disinfection Contact Tanks Using Computational Fluid Dynamics.

The scope of work of this second phase includes:

1. Prepare a written preliminary Phase 2 Research Plan and provide an oral presentation to the Division project team that includes, but is not limited to the following elements:
 - a. Identifying potential “pre-engineered” tank configurations to evaluate in Phase 3. The Division project team will select 3 configurations to be studied further in Phase 3.
 - b. Performing tracer studies at a number of existing and/or new water treatment systems. The Division project team will identify appropriate systems and make arrangements for the use of the system’s facilities. The tracer study procedure will need to be clearly outlined in this research plan.
 - c. Performing CFD modeling of the process at the existing treatment plants where tracer studies are to be performed.
 - d. Comparing tracer studies to modeling results and assessing the adequacy of the modeling software to predict actual field performance.
 - e. Using CFD modeling, to evaluate the effect of various parameters on the baffling factor for each “pre-engineered” tank configuration. The parameters to be evaluated include, but are not limited to:
 - i. Flowrate
 - ii. Tank dimensions

- iii. Inlet/outlet velocities
 - iv. Inlet/outlet configuration
2. Prepare a final Phase 2 Research Plan addressing all comments and feedback from the Division project team.
 3. Once the Phase 2 Research Plan is approved by the Division project team, Phase 3 can begin.

Phase 3 involves the development of pre-engineered small disinfection systems. While this thesis includes some of the phase 3 development (primarily in appendix H), it is beyond the scope of this study.

1.2 Organization of Thesis

Chapter 2 provides a literature review which discusses traditional contact tank design, a brief introduction to the disinfection process, various evaluation methodologies of hydraulic efficiency and their shortcomings, system evaluation using experimental methods (e.g., tracer studies), residence time distribution (RTD) curve formulation and interpretation, flow and transport modeling, and modeling software. Chapter 3 describes the hydrodynamics and scalar transport for the systems of interest, a pipe loop, series of pressurized tanks, open surface tanks, and a baffled tank. Original research is performed on the first three of these systems while the baffle tank is analyzed as a case study. Chapter 4 analyzes the hydraulic efficiency of these systems from RTD curves using the USEPA's *BF* methodology and proposes a better measure of hydraulic efficiency.

Chapter 5 provides conclusions on this research and gives recommendations for continuing research as part of CDPHE's project scope.

Appendix A contains the derivation of the Reynolds-Averaged Navier-Stokes equations. Appendix B gives the details of the numerical schemes utilized in FLUENT as well as the user defined function to describe the passive scalar transport. Appendix C presents the results of the grid independence studies for each of the computational models. Appendix D contains the hydraulic model developed to analyze the pressure losses through the pressurized tank systems. Appendix E contains a standard operating procedure (SOP) developed for conservative step-input tracer studies on small systems. Appendix F contains a standard operating procedure (SOP) developed for conductivity studies on small systems. Appendix G contains additional results for the pressurized tank systems. Finally, appendix H contains sample 'pre-engineered' disinfection systems using series pressurized tank systems.

1.3 New Contributions

The presented research has led to the following contributions:

- 1) Validity of using CFD for analysis of passive scalar transport through small public water systems (e.g., a pipe loop system, series of pressurized tank systems, and open surface tank systems)
- 2) A more representative measure of hydraulic mixing efficiency based on the ratio of t_{10} to t_{90} in contrast to the idealized BF formulation used by the USEPA
- 3) Preliminary "pre-engineered" systems that meet the appropriate 4-log inactivation based on CFD analysis and disinfection calculations

1.4 Research Publications

This thesis contains portions of a peer-reviewed journal publication by Wilson and Venayagamoorthy (2010) in the journal *Environmental Science and Technology* pertaining to the hydraulic efficiency of disinfection systems.

Portions of this thesis have also been accepted for presentation to the 13th Annual Water Distribution Systems Analysis (WDSA) Symposium at the 2011 World Environmental and Water Resources (EWRI) Congress of the American Society of Civil Engineers (ASCE). An article entitled "Hydraulics and mixing efficiency of small public water disinfection systems," will also be published in the conference proceedings. A portion of the work found in chapter 3, in addition to some additional research on the inlet configurations of the open surface tanks, is under preparation for submission to the *ASCE Journal of Hydraulic Engineering*.

A talk entitled "Optimizing the hydraulic efficiency of disinfection contact basins for small drinking water systems," was also presented at the 2010 Rocky Mountain Section of the American Water Works Association (RMSAWWA) Annual Conference, 12-15 September 2010 Keystone, CO.

1.5 Units

The International System of Units (SI) is used throughout this document for consistency and use in comparing results with those obtained in FLUENT.

CHAPTER 2: LITERATURE REVIEW

2.1 Small Public Water Systems

Approximately 94 percent of the 156,000 public water systems in the United States serve fewer than 3,300 people. These systems are classified as small public water systems. In Colorado, small public water systems constitute approximately 75 percent of the state's total water systems. While all public water systems are required to meet the same quality requirements, these small systems face technical, managerial, and financial difficulties oftentimes not present in much larger government-supported municipal facilities (USEPA 2010). Figure 2.1 shows some of the considerations in the planning process for these small systems.

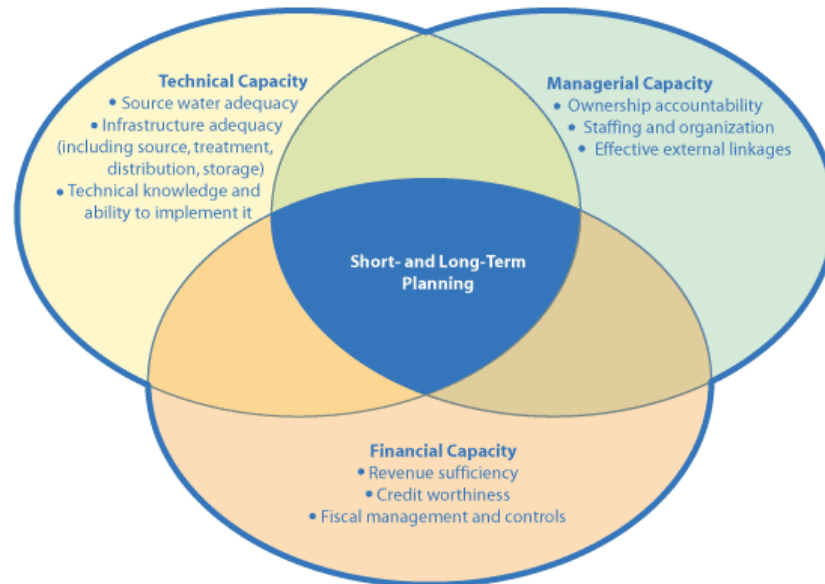


Figure 2.1 Short- and Long-Term Planning Considerations for Small Public Water Systems (USEPA 2010).

The most crucial of these aspects is the technical capacity to deliver clean water which is frequently lacking for these small systems. Currently, 94 percent of the Safe Drinking Water Act (SDWA) annual violations are attributed to small systems. Nearly 77 percent of these are for Maximum Contaminant Level (MCL) violations, often directly related to microbiological violations (USEPA 2000). A majority of these systems lack the financial capacity to perform a thorough hydraulic study and instead rely on visual determination of *BF* for use in disinfection calculations based on the USEPA guidelines found in the *LTIESWTR Disinfection Profiling and Benchmarking Technical Guidance Manual* (USEPA 2003). This methodology is inherently flawed, the details of which will be discussed extensively in chapter 4. The presented research will increase the technical knowledge of these small systems through dissemination of results via CDPHE's regulatory oversight, journal articles, and this thesis.

2.2 Contact Tank Design

The objective of a contact tank is to provide an adequate contact time between the supply water and disinfectant to ensure inactivation of microbial pathogens and bacteria. The design and operation of chlorine contact tanks has been largely based on the generic volume displacement criterion, or *TDT* (Trussell & Chao 1977, Wang & Falconer 1998, and Kothandaraman *et al.* 1973). Using this volume displacement criterion assumes plug flow through the tank idealizing the complex flow dynamics (e.g., separation, recirculation, inlet and outlet effects, and wall effects). Without the sophisticated numerical and CFD tools available today, designing contact tanks using plug flow criteria

was logical given that most chemical reactions are more efficient in plug flow (Trussell & Chao 1977).

In practice, it is difficult to achieve a perfect plug flow system, or plug flow reactor (PFR) (Wang & Falconer 1998 and Teefy 1996). The opposite extreme in hydrodynamics from perfect plug flow is complete mixing often represented as a continuous-flow stirred tank reactor (CSTR) model. Most systems operate somewhere between these two extremes of flow dynamics (Teefy 1996).

2.3 Disinfection and Log Inactivation

While the research in this project focused on the flow dynamics and hydraulic efficiency of small public water disinfection systems, it is important to have a basic understanding of the disinfection process. Chlorine was first introduced as a disinfectant in the early 20th century throughout many American cities and resulted in a significant reduction in waterborne diseases such as typhoid (Letterman 1999). Chloramination, the process of disinfection from the combination of ammonia and chlorine, followed shortly behind chlorine for use in disinfection and has recently regained popularity due to concerns over organic by-products from chlorine (Wolfe *et al.* 1984 and Singer 1994). Numerous other disinfectants (e.g., ozone, chlorine dioxide, UV radiation, and surfactants) have been used over the years but chlorination remains the most widely used disinfectant in small public water systems due to its reliability and relative ease of use. It is important to note the disinfection capabilities of chlorine are greatly influenced by solution strength, age, temperature, pH, and presence of metal catalysts (Gordon *et al.*

1993, 1995). Figure 2.2 shows the available fraction of free chlorine as a function of pH for a temperature of 20°C.

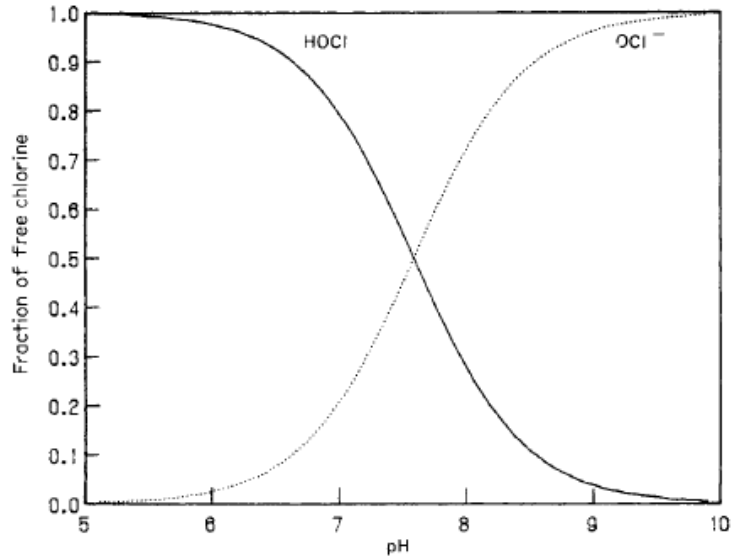


Figure 2.2 Fraction of free chlorine as a function of pH for water at 20° C (Letterman 1999).

As observed in Figure 2.2, chlorine disassociates into hypochlorous acid (HOCl) and hypochlorite (OCl⁻) as pH increases. There is an exponential decrease in the available fraction of free chlorine in the form of hypochlorous acid as pH increases. Hypochlorous acid is much more effective at disinfection as compared to hypochlorite and for this reason, inflows must have a pH less than 10 for small systems in the state of Colorado as determined by CDPHE.

Similarly, the available fraction of free chlorine decreases as temperature decreases. To evaluate the effectiveness of disinfection against viruses and Giardia per the USEPA requirements, the log inactivation protocol is used. Standards currently state that systems must meet 3-log inactivation for Giardia and under the recently promulgated Ground Water Rule (GWR), 4-log inactivation for viruses, that is 99.9 and 99.99 percent inactivation, respectively (USEPA 2009). Log tables, such as those given in the

LTIESWTR Disinfection Profiling and Benchmarking Technical Guidance Manual, are used to compute a system's required contact time based on temperature and pH. The following equations demonstrate the 3- and 4-log inactivation for Giardia and viruses.

$$\frac{CT}{CT_{99.9}} \geq 3, \quad (2.1)$$

$$\frac{CT}{CT_{99.99}} \geq 4, \quad (2.2)$$

where CT is the product of the chlorine residual C and the contact time T , also referred to as t_{10} , $CT_{99.9}$ is the contact time for 3-log inactivation, and $CT_{99.99}$ is the contact time for 4-log inactivation. The quotient of the left-hand side of equations 2.1 and 2.2 must be greater than 3 and 4, respectively, to meet the log inactivation requirements.

2.4 Tracer Studies

A tracer study is conducted in water treatment facilities to investigate the hydraulic efficiency of the contact tank system. The tracer test is a simple concept wherein a conservative (nonreactive) tracer (e.g., fluoride, lithium, or rhodamine WT) is introduced into a system and the change in concentration is observed in the effluent over time until it reaches a steady-state. Plotting this change in concentration over time yields the so called residence time distribution (RTD) or flow-through curve (FTC). The USEPA recommends that a tracer study be conducted at two to four different flow rates on the same system for consistency (USEPA 2003). There are two methods of conducting tracer studies, primarily pulse (or slug) input and step (or continuous feed) input.

2.4.1 Pulse Input Tracer Study

A pulse input tracer study involves placing a known mass of conservative tracer instantaneously upstream of the contact tank inlet where it must be completely mixed with the influent stream. Generally, the mixing time required should be less than 1 percent of the *TDT*. Sampling in pulse input tracer studies should occur early on to ensure the fast-moving rising limb is captured. The RTD curve produced from this testing method exhibits a rising limb as the concentration increases, a maximum, and a falling limb as the tracer leaves the system. Figure 2.3 shows a RTD curve for a pulse input tracer study performed on an arbitrary disinfection system with time normalized to the *TDT*.

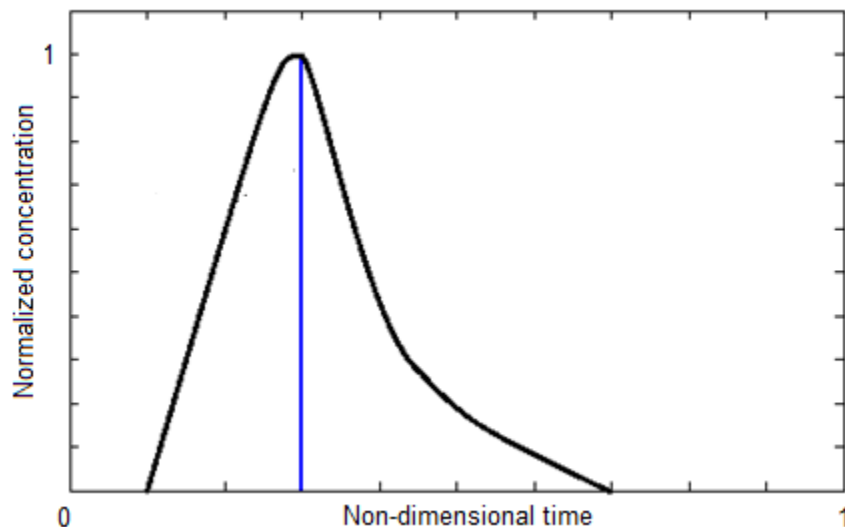


Figure 2.3 RTD curve for a pulse input tracer study for an arbitrary disinfection system as compared to a step impulse function.

Normalization of the tracer concentration and time allows for comparison of the behavior of different systems. While the pulse input method is easier to perform in most

circumstances, the results require more extensive analysis for interpretation. Table 2.1 presents the advantages and disadvantages of pulse input tracer studies (Teefy 1996).

Table 2.1 Summary of advantages and disadvantages of pulse input tracer study.

Advantages	Disadvantages
Less chemical is needed for pulse input than for a step input	Danger of missing the peak if sampling frequency is not correct
Mean residence time, recovery rate, and variance can be determined more readily	More mathematical manipulation of results is needed to obtain t_{10}
Chemical addition can be simple in some situations	Cannot repeat the test easily (no receding curve available)
	Difficult to determine the amount of tracer that should be added for the test

2.4.2 Step Input Tracer Study

In comparison, a step input tracer study is performed by feeding a conservative tracer at a constant rate into the system until the concentration reaches a steady state in the effluent stream. An advantage of the step input method is the possibility to obtain results from the increasing mode as the tracer is constantly fed into the system and the receding mode after steady state is reached and the tracer input is discontinued. These studies can be performed using existing chemical feed equipment or by constructing a temporary input system as long as the feed rate is constant for the increasing mode and the system flow rate remains constant through both modes. Sampling for step input tracer studies should occur at regular intervals and ensure that steady state is captured. Again, plotting the normalized concentration against the normalized time as seen in Figures 2.4(a) and (b) displays the nature of the system for both increasing and receding modes.

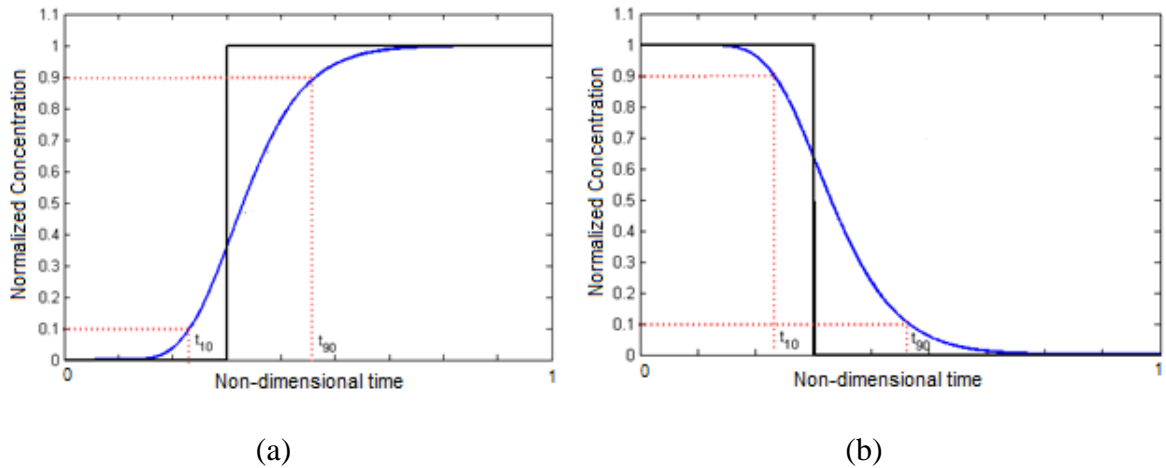


Figure 2.4 (a) rising RTD curve and (b) receding RTD curve for a step input tracer study for an arbitrary disinfection system as compared to a step impulse function.

While these plots for pulse and step input tracer studies display the same information about the systems, t_{10} can be more easily interpreted from a step input RTD curve (Teefy 1996). Table 2.2 presents the advantages and disadvantages of step input tracer studies (Teefy 1996).

Table 2.2 Summary of advantages and disadvantages of step input tracer study.

Advantages	Disadvantages
Sometimes can be done with existing plant chemical feed equipment	More tracer chemical is required than in a pulse input test
t_{10} can be determined graphically from curve	Cannot reliably calculate mass recovery or mean residence time to check validity
Results can be verified by monitoring the receding curve	May have to install chemical feed equipment if not already present

In cases where multiple tracer studies cannot be performed, the USEPA *Guidance Manual* (1986) recommends the following equation be used for prediction of contact time based on the same BF .

$$T_{10S} = T_{10T} \times Q_T / Q_D, \quad (2.3)$$

where T_{10S} is t_{10} at the system flow rate, T_{10T} is t_{10} at the tracer study flow rate, Q_T is the tracer study flow rate, and Q_D is the system flow rate.

2.5 Hydraulic Efficiency and Residence Time Distribution (RTD) Curves

RTD curves constructed from tracer study results are one of the main tools used to assess the hydraulic efficiency of disinfection systems. The shape of the curve provides insight to the nature of the flow in the system (Stamou 2002). For example, a steeper gradient represents conditions closer to plug flow dominated by advection and a flatter gradient represents conditions further from plug flow dominated by diffusive processes. While the curve reveals the nature of transport through the system resulting from the flow dynamics, hydraulic indices are used to more easily interpret the RTD curves. These indices are separated into short circuit and mixing indicators but often describe a multitude of physical phenomena (e.g., advection, diffusion, short-circuiting, mixing, recirculation, and dead zones). Short-circuiting describes the degree to which fluid leaves the system earlier than the TDT and mixing describes the "random" spreading of fluid throughout the system via turbulent diffusion and recirculation via flow separation (Teixeira & Siqueira 2008). While turbulence is often viewed as a random and chaotic process, in reality it is a somewhat orderly transference of energy between scales (Pope 2000). Short-circuiting is an important aspect of system operation but is not of significant importance to this research because it describes initial concentration front which is only one portion of the overall hydraulic mixing efficiency. Table 2.3 describes common mixing indices and literature references as described by Teixeira and Siqueira (2008).

Table 2.3. Common hydraulic mixing indices and references.

Index	Definition	References
σ^2	<i>Dispersion index</i> - Ratio between the temporal variance of the RTD function (σ_t^2) and (t_g^2)	Levenspiel (1972), Lyn and Rodi (1990), Marske and Boyle (1973), Stamou and Adams (1988), Stamou and Noutsopoulos (1994), Teixeira (1993), and Thirumurthi (1969)
MI	<i>Morril index</i> - Ratio between the times necessary for 10 and 90 percent of the mass of tracer that was injected at the inlet section to reach the outlet of the unit, $MI = t_{90}/t_{10}$	Hart (1979), Hart <i>et al.</i> (1975), Marske and Boyle (1973), Rebhun and Argaman (1965), Sawyer and King (1969), Stamou and Noutsopoulos (1994), Teixeira (1993), and Thirumurthi (1969)
$t_{90}-t_{10}$	Time elapsed between t_{10} and t_{90}	Stamou and Noutsopoulos (1994)
$t_{75}-t_{25}$	Time elapsed between t_{25} and t_{75} , where t_{25} and t_{75} are the respective times necessary for 25 and 75 percent of the tracer that was injected at the inlet section to reach the outlet of the unit	Lyn and Rodi (1990), Stamou and Noutsopoulos (1994), and Stamou and Rodi (1984)
d	<i>Dispersion number</i> - Indicator of system dispersion with 0 equal to perfect plug flow	Trussell and Chao (1977), Marske and Boyle (1973), Levenspiel (1972), Hart (1979), and Levenspiel and Smith (1957)
BF	<i>Baffle factor</i> - The ratio of t_{10} to TDT	USEPA (1986 and 2003)

The temporal variance of the RTD function is given by

$$\sigma_t^2 = \frac{T^2 \int_0^\infty \theta^2 E(\theta) d\theta}{\int_0^\infty E(\theta) d\theta}, \quad (2.4)$$

where T is the total residence time, θ is the non dimensional time (T/TDT), and $E(\theta)$ is the value of the probability density function for a pulse input tracer study. The center of mass of the RTD curve, t_g , is given by

$$t_g = \frac{T \int_0^\infty \theta E(\theta) d\theta}{\int_0^\infty E(\theta) d\theta}, \quad (2.5)$$

where T is the time, θ is the non dimensional time, and $E(\theta)$ is the value of the probability density function for a slug-dose tracer study. This study addresses hydraulic efficiency

from a quantitative perspective of flow processes rather than on the statistical nature of RTD curve development.

Teixeira and Siqueira (2008) commented that while each of the indices analyzed had advantages, none of the tested mixing indices were adequate measures of hydraulic efficiency. The dispersion index is mostly a statistical parameter relating the temporal variance of the RTD curve but is difficult to replicate. On the other hand, $t_{90}-t_{10}$ and $t_{75}-t_{25}$ were much easier to replicate but only provide a difference in arrival times which is difficult to interpret in terms of efficiency. The Morrill Index (MI) evaluates the amount of diffusion in a system based on the ratio t_{90}/t_{10} which is also difficult to interpret because it has no upper limit to bound values between pure advection and pure diffusion (at least in theory) (USEPA 1986 and Teixeira & Siqueira 2008).

Marske and Boyle concluded that the dispersion number d was the most reproducible of the mixing indices (1973). This quantity can also be interpreted as a non-dimensional diffusivity. As d decreases, the contact system approaches plug flow in a similar manner as MI approaches 1. Using dye curves instead of conservative trace analysis, Levenspiel and Smith (1957) developed between the relationship between the dye curve and the dispersion number seen in equation 2.6

$$E_{\theta} = \frac{1}{\sqrt{4\pi\theta d}} \exp\left[\frac{-(1-\theta)^2}{4\theta d}\right] \quad (2.6)$$

where E_{θ} is the probability density function of the fluid residence time, θ is the non-dimensional time, and d is the dispersion number. However, the dispersion number is not a global representation of hydraulic efficiency since the same dispersion number can be obtained from multiple curves with differing gradients and it is empirically derived.

The need for a design parameter for disinfection systems with the appropriate contact time, or t_{10} , prompted the USEPA's development of the *BF* classification system. *BF* is often assumed to be synonymous with mixing efficiency when in actuality it is only a partial measure of hydraulic efficiency with t_{10} resulting from the flow dynamics and scalar transport properties of the system and *TDT* resulting from the ideal plug flow assumption (Teefy 1996). The *BF* formulation fails to take into account the actual dynamics going on in any given disinfection system beyond t_{10} and therefore, in all cases (at least for the all cases discussed in this research) tends to provide an overestimation of the hydraulic efficiency.

An extensive literature review has shown that all existing indicators of hydraulic efficiency have flaws in a global sense. The dispersion index σ^2 gives a good representation of a system's efficiency but is difficult to replicate. The dispersion number d , while easy to replicate, is not always indicative of the system at hand and can give the same result for hydraulically differing systems. The dispersion number also incorporates the inherent assumption of ideal plug flow through normalizing time to *TDT* which is not an actual parameter of the system. $t_{90}-t_{10}$ and $t_{75}-t_{25}$ are also easy to replicate but do not provide a good assessment of the system's efficiency. *BF*, while technically a system design parameter and not a mixing index, only provides a partial assessment of efficiency. The Morrill Index is the best indicator of those found in literature but is often difficult to interpret leaving the door open to a better indicator of hydraulic efficiency.

2.6 Flow Modeling and Computational Fluid Dynamics

Analytical methods provide a basic overview of complex fluid dynamic problems but they rarely provide a complete understanding of the problem at hand. Experimental methods can be used to gain a better understanding as to the physical processes at work but are often expensive and labor intensive to perform. Through use of mathematical and numerical tools, complex fluid dynamic problems, often in the form of nonlinear partial differential equations, can be broken into algebraic equations and solved computationally. With the advent of personal computers, CFD became popular in the research community because of its adaptability and portability. Because of the accessibility to CFD software, it is tempting to use programs blindly and take the results at face value. Without the theoretical understanding of the problem and experimental data upon which to validate results, CFD model output is essentially worthless. When these three aspects are considered carefully, CFD modeling becomes a powerful tool capable of analyzing problems far beyond the realm of analytical techniques (Anderson 1995). While CFD and numerical modeling have been used extensively to evaluate the hydraulic efficiency of large municipal disinfection facilities (see e.g., Stamou 2008, Falconer & Ismail 1997, Wang & Falconer 1998, Falconer and Liu 1988, Stamou 2002, Wang *et al.* 2003, Stamou and Noutsopoulos 1994, Stamou *et al.* 2009, Stamou 1991, Stamou *et al.* 1989, Templeton *et al.* 2006, Khan *et al.* 2006, and Rauen *et al.* 2007), there is little research on small systems.

The use of CFD inherently involves the development of a model, or simplified description of reality. The complexity of the model is governed by its purpose, available resources, and constraints. Determination must be made if a full scale three-dimensional

model is necessary or if a simplified one- or two-dimensional model is sufficient based on the allowable assumptions in the model development. For example, a rectangular baffled contact tank with inlet and outlet weir configurations can be sufficiently modeled in two-dimensions because the flow varies minimally in the vertical direction. For this study, three-dimensional models were used in order to capture the complex geometry and flow dynamics in the systems.

Within the model development it is important to consider the governing processes. For most fluid dynamic problems, the conservation of mass and conservation of momentum, expressed in terms of the Navier-Stokes equations, are sufficient for describing the process of fluid motion. The conservation of mass (for incompressible flows) is given by

$$\frac{\partial u_i}{\partial x_i} = 0, \quad (2.7)$$

where u_i is the turbulent velocity field. The general form of the Navier-Stokes equations (in tensor notation) with the Boussinesq approximation is

$$\frac{\partial u_i}{\partial t} + \frac{\partial}{\partial x_j} (u_i u_j) = -\frac{1}{\rho_o} \frac{\partial p}{\partial x_j} + \nu \frac{\partial^2 u_i}{\partial x_j \partial x_j} - \frac{g}{\rho_o} \rho \delta_{iz}, \quad (2.8)$$

where u_i is the turbulent velocity field, ρ_o is the reference density to a reference temperature of the fluid T_o , p is the pressure, ρ is the mass density of the fluid, ν is the kinematic viscosity of the fluid, g is gravitational force, and δ_{iz} is the Kronecker delta function. The Boussinesq approximation is used to simplify the continuity equation into the incompressible form and based on the assumption that the density change in the direction of flow is small in comparison to the magnitudes of the velocity gradients.

2.7 Turbulence and Turbulence Models

Turbulence is the time dependent chaotic behavior seen in many environmental fluid flows (e.g., waterfalls, plumes of volcanic smoke, or oceanic transport of oil spills). Virtually all flows of practical engineering interest are turbulent but are far less easily seen. An important characteristic of turbulence, especially in regards to the hydraulic efficiency of disinfection systems, is the ability to better transport and mix fluid as compared to laminar flows. For over a century, turbulence has been studied in hopes to develop a complete analytical theory with no success to this point in time (Pope 2000 and Wilcox 2007).

The difficulty in developing any kind of tractable quantitative theory of turbulent flows lies in its three-dimensional, time-dependent, and apparent random motion of its velocity field. There is also the issue of varying turbulent scales and the transfer of energy between these scales (thought originally to be unidirectional but now believed to be omnidirectional). The numerical solution of the Navier–Stokes equations for turbulent flow is extremely difficult due largely to the nonlinear convective term and the pressure-gradient term (Pope 2000). Thus models are often implemented using linearized numerical systems to solve the Navier-Stokes equations.

To be considered complete, the constituent equations of a model must be free from flow-dependent specifications. Direct Numerical Simulations (DNS) are complete, whereas the mixing-length model is incomplete (the mixing length must be specified). Few models do not require numerical methods (e.g., friction factor f and Mannings n); however, most do. It is important to consider the nature of the problem and if software is

available or has to be developed. The exponential increase in computing power allows for solutions to problems that are more complex and the use of more computational intensive models. Not all models are applicable to all flows. Many models based on two-point correlations are applicable to homogeneous turbulence only. DNS is only applicable to low or moderate Reynolds number and simple geometries due to the steep rise in computational requirements that still exceed state-of-the-art computational power. Accuracy is crucial to any model through comparison with experimental data. It is important to consider both experimental and model/numerical error in this comparison. Ambiguity in the model results can be resolved in performing grid independence and sensitivity analyses. Discrepancies in boundary conditions can also lead to inaccuracies in model data. Typically, there is no “best” turbulence model for any one particular problem, but it is up to the sound judgment of the user in determining a model that best handles the prescribed problem. Of course, in selecting any model, whether it be an overarching computational model or turbulence model as part of a larger model, it is important to consider the following: level of description, completeness, cost and ease of use, range of applicability, and accuracy (Pope 2000).

2.7.1 Direct Numerical Simulations (DNS)

A Direct Numerical Simulation (DNS) solution involves a complete time-dependent solution of the Navier-Stokes and continuity equations (Wilcox 2007). All lengthscales and timescales must be resolved yielding DNS too computationally expensive for most engineering applications. Also, because computational cost increase on the order of Re^3 , DNS is restricted to low-to-moderate Reynolds number flows (Pope

2000). From these restrictions, DNS is not an appropriate choice for analysis of disinfection systems.

2.7.2 Large Eddy Simulations (LES)

A Large Eddy Simulation (LES) solution involves a hybrid of DNS and Reynolds-Average Navier-Stokes (RANS) solutions (Wilcox 2007). Solutions to the largest eddies are computed while solutions to the smallest eddies are modeled using resolved scales. LES requires much smaller cells than RANS models to completely resolve the larger eddies and is time dependent. Solutions for LES still requires more computational power than RANS and orders of magnitude difference in solution time, but are becoming more feasible with increasing computing power and the corresponding decrease in price of computing power.

2.7.3 Reynolds-Averaged Navier-Stokes (RANS) Equations

Reynolds-Averaged Navier-Stokes (RANS) equations are the oldest and most widely used approach to turbulence modeling. The RANS equations involve the time-averaging of the time-dependent fluctuating velocity and pressure fields. The time-dependent decomposition for the turbulent velocity and pressure fields (commonly known as the Reynolds decomposition) is displayed in equations 2.9 and 2.10.

$$u_i(t) = \bar{u}_i + u'_i, \quad (2.9)$$

$$p(t) = \bar{p} + p', \quad (2.10)$$

where $u_i(t)$ is the time-dependent turbulent velocity field, \bar{u}_i is the time-averaged velocity field, u'_i is the time-dependent turbulent velocity field fluctuations, $p(t)$ is the

time-dependent pressure field, \bar{p} is the time-averaged pressure field, and p' is the time-dependent pressure field fluctuations. Similarly, the continuity equation can be time-averaged to yield

$$\frac{\partial \bar{u}_i}{\partial x_i} = 0 , \quad (2.11)$$

where \bar{u}_i is steady-state turbulent velocity field. The RANS equations are a time-averaged representation of the motion of fluid flow as shown in equation 2.12 through the combination of equation 2.8 and equations 2.9 and 2.10 (shown in detail in appendix A). In terms of a qualitative description, the left hand portion of equation 2.12 represents the mean momentum of the flow and is balanced by the mean pressure field, viscous stresses, apparent Reynolds stress, and the mean body force represented by the gravitational force in the z -direction.

$$\frac{\partial \bar{u}_i}{\partial t} + \bar{u}_j \frac{\partial \bar{u}_i}{\partial x_j} = -\frac{1}{\rho_o} \frac{\partial \bar{p}}{\partial x_i} + \frac{\partial}{\partial x_j} \left(\nu \frac{\partial \bar{u}_i}{\partial x_j} - \overline{u'_i u'_j} \right) - \frac{g}{\rho_o} \rho \delta_{iz} , \quad (2.12)$$

where \bar{u}_i is the time-averaged velocity field, ρ_o is the reference density to a reference temperature of the fluid T_o , ρ is the mass density of the fluid, \bar{p} is the average pressure, ν is the kinematic viscosity of the fluid, $\overline{u'_i u'_j}$ is the Reynolds stress, g is the gravitational force, and δ_{iz} is the Kronecker delta function.

The Reynolds stress term adds a second order tensor of unknowns for which various models can provide different levels of closure. In most circumstances, it is easiest to solve this closure problem through the turbulent, or eddy, viscosity ν_t as seen in equation 2.13 which represents the Reynolds stress according to the turbulent-viscosity hypothesis resulting in a similarity to the viscous stress in a Newtonian fluid (Pope 2000).

$$\overline{u'_i u'_j} = \frac{2}{3} k \delta_{ij} - \nu_t \left(\frac{\partial \overline{U}_i}{\partial x_j} + \frac{\partial \overline{U}_j}{\partial x_i} \right), \quad (2.13)$$

where $\overline{u'_i u'_j}$ is the Reynolds stress, k is the turbulent kinetic energy, δ_{ij} is the Kronecker delta function, ν_t is the turbulent viscosity, and $\overline{U}_{i,j}$ is the time-averaged velocity field. The only unknown in equation 2.13 is ν_t . Numerous methods exist to prescribe ν_t from empirical zero-equation models to complex two-equation models described in the following subsection

2.7.4 Two-Equation Turbulence Models

Selecting an appropriate turbulence model is another important aspect of the model. Numerous two-equation turbulence models exist, but each were developed for specific applications such as the Re-Normalisation Group (RNG) k - ε turbulence model and the shear stress transport (SST) k - ω turbulence model. The standard k - ε turbulence model (Launder & Sharma 1974) was used for the research in this study because of its wide use in similar applications to chlorine contact tanks (e.g., Templeton *et al.* 2006, Rauen *et al.* 2007, and Stamou 2008). The turbulent kinetic energy is defined by the following equation.

$$k = \frac{1}{2} (\overline{u_1'^2} + \overline{u_2'^2} + \overline{u_3'^2}), \quad (2.14)$$

where k is the turbulent kinetic energy, $\overline{u_1'^2}$ is the mean of the x-component velocity fluctuation squared, $\overline{u_2'^2}$ is the mean of the y-component velocity fluctuation squared, and $\overline{u_3'^2}$ is the mean of the z-component velocity fluctuation squared in the z-direction. The turbulent viscosity for the standard k - ε turbulence model is given by the following.

$$\nu_t = \frac{C_\mu k^2}{\epsilon}, \quad (2.15)$$

where ν_t is the turbulent viscosity, k is the turbulent kinetic energy, C_μ is a constant, and ϵ is the turbulent kinetic energy dissipation rate.

2.8 Scalar Transport Modeling

Due to the relatively short retention times of the contact tanks in this study, the chemical and biological processes of disinfection were not considered. This study focused on the efficiency with which a passive scalar is mixed throughout the system. A passive scalar is any species that can be transported but is non-reactive and has no influence on the flow field. Traditionally such studies have been performed on Froude scale models; however, Falconer and Liu (1988) showed that physical models often overestimate the advection-diffusion processes and momentum transfer and underestimate the influences of bed friction. The time-averaged advection-diffusion equation for the transport of a passive scalar is given by

$$\frac{DC}{Dt} = \frac{\partial C}{\partial t} + \bar{u}_i \frac{\partial C}{\partial x_i} = \frac{\partial}{\partial x_i} \left(\left(\kappa + \frac{\nu_t}{Sc_t} \right) \frac{\partial C}{\partial x_i} \right), \quad (2.16)$$

where C is the concentration (e.g., conservative tracer or chlorine-containing species), \bar{u}_i is the steady state turbulent velocity field, κ is the molecular diffusivity of the tracer, ν_t is the turbulent eddy viscosity, and Sc_t is the turbulent Schmidt (or Prandtl) number. \bar{u}_i and ν_t are obtained from the steady state solution of the momentum equations (equations 2.12 and 2.13). The turbulent Schmidt number links the momentum and scalar fluxes by

$$Sc_t = \frac{\nu_t}{K_t}, \quad (2.17)$$

where Sc_t is the turbulent Schmidt number and K_t is the turbulent scalar diffusivity. For neutrally stratified flows as in this study, the turbulent Schmidt number Sc_t is taken as 0.7 as shown by Venayagamoorthy and Stretch (2010).

2.9 Modeling Software

ANSYS DesignModeler and Meshing were used for the pre-processing development of the computational models. ANSYS FLUENT v. 12.1 was used as the CFD software for computations and post-processing analysis in this research because of its usage in both the research community and in industry.

2.9.1 Workbench

Workbench is a graphical user interface (GUI) that attempts to incorporate entire process of computational modeling into a singular module and spans a wide spectrum of application from multiphysics to structural analysis. Within workbench, ANSYS DesignModeler was used to create the geometry for each of the models in this study although Workbench is capable of being fully-integrated with any commercially available computer aided design (CAD) software packages. ANSYS Meshing was then used to mesh each of the computational models using the automated meshing feature (non-uniform tetrahedral cells for fluid dynamic preset). While the automated meshing feature may appear to be beneficial, it actually makes it more difficult for the user to control the mesh as compared to GAMBIT (one of the primary software packages used for model creation and meshing prior to Colorado State University's acquisition of Workbench). The streamlined process incorporated in the ANSYS Workbench v. 12.0 seems to encourage the use of CFD for any and every problem when analytic solutions may be

more than adequate. With the increasing ease of use in many CFD platforms, it has become more important for the user to truly understand the process of modeling and discern when models are needed

2.9.2 FLUENT

ANSYS FLUENT v. 12.1 is a finite volume CFD software package that contains a broad spectrum of modeling capabilities for flow and turbulence modeling, heat transfer, and reactions. FLUENT incorporates LES and the most widely used RANS turbulence models. FLUENT also supports parallel processing which is advantageous in analyzing models with a large number of cells in a timely manner. Dynamic load balancing ensures that an equal load is shared among the parallel processors. A unique feature of FLUENT is the ability to create user-defined functions providing the flexibility to create entirely new analysis tools or alter existing functions to match models conditions. This feature was used to model the scalar transport in this study. Appendix B describes many of the numerical schemes used in FLUENT and the user-defined function written in the C programming language.

CHAPTER 3: EVALUATION OF FLOW AND SCALAR TRANSPORT CHARACTERISTICS

3.1 Introduction

As discussed in chapter 2, the flow dynamics, as influenced by a system's parameters and geometry, determine how a scalar is transported through the system. Most contact tanks exhibit uneven flow paths, representative of dead zones, or regions of recirculation or stagnation, flow separation, and turbulent effects (Wang & Falconer 1998). These dead zones rely on much slower and less effective processes (e.g., diffusion) to distribute the scalar (e.g., conservative tracer or chlorine-containing species). These flow phenomena result in some particles residing longer in the system than others that are simply advected. The degree to which particles reside longer in the system (e.g. the more recirculation, turbulence, and stagnation fluid particles encounter) than those advected describes the system's hydraulic efficiency which is discussed more in depth in chapter 4. Traditionally, measurement of disinfection system flow characteristics used existing contact tank systems or relied on scaled similarity models (e.g., see Shiono and Teixeira 2000) using laser or acoustic anemometry. Such methods are often costly and, on the full-scale, can only be performed using pre-existing infrastructure. Difficulty also arises in analyzing the flow through closed, pressurized systems such as pipe loops. As shown in literature, and in this study, CFD is a valid tool for analyzing the flow characteristics and scalar transport through contact tank systems.

This chapter presents the flow and resulting scalar transport analysis of a pipe loop system, series of pressurized tank system, two open surface tank systems, and a baffled tank system and their respective scalar transport characteristics.

A paper containing a portion of this chapter has been accepted for oral presentation to the 13th Annual Water Distribution Systems Analysis (WDSA) Symposium at the 2011 World Environmental and Water Resources (EWRI) Congress of the American Society of Civil Engineers (ASCE). A significant portion of this chapter, in addition to some additional research on the inlet configurations of the open surface tanks, is being incorporated into a paper for submission for possible publication to the ASCE *Journal of Hydraulic Engineering*.

3.2 CFD Modeling

The following subsections describe the flow and scalar transport characteristics of the disinfection systems analyzed in this study, primarily a pipe loop contactor, system of pressurized tanks, two different open surface tanks, and a baffled contact tank.

3.2.1 Pipe Loop System Configuration

The city of Fort Collins Municipal Water Treatment Facility allowed the use of their pilot pipe loop system for this study. The tracer was sampled after 14 major lengths to take advantage of a pre-existing tap in the system. The internal diameter of the piping was 0.15 m with a major length of 6.55 m and a minor length of 0.21 m measured from the outside of the joints. Figure 3.1 shows the pilot pipe-loop facility.



Figure 3.1. Pilot pipe-loop facility at Fort Collins Municipal Water Treatment Facility.

3.2.1.1 Pipe Loop System Computational Model Setup

Using ANSYS DesignModeler a model was created reflecting the sampling point after 14 major lengths as shown in Figure 3.2 (a). The model geometry was then meshed using ANSYS Meshing using the fluid dynamic automated procedure producing an initial unstructured tetrahedral mesh of approximately 895,000 cells shown in Figure 3.2 (b).

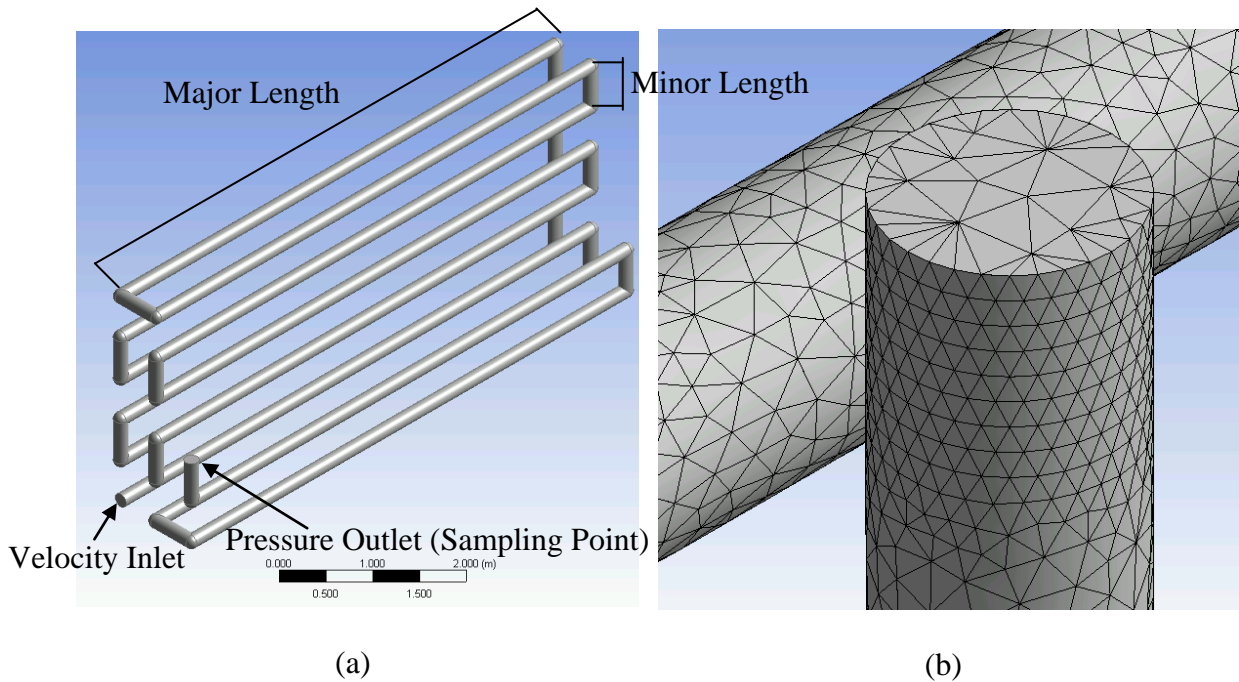


Figure 3.2. (a) Pipe loop geometry and (b) unstructured tetrahedral mesh for CFD analysis.

3.2.1.2 Pipe Loop System FLUENT Setup

This model was then imported into ANSYS FLUENT for setup. The boundary conditions on this system were an inlet velocity (which varied in magnitude depending on the analyzed flow rate), an outlet pressure, and a standard no-slip wall condition for the pipe wall. The turbulent boundary conditions were set to an intensity of 10 percent and hydraulic length of 1 m. As seen in chapter 4, these parameters produced a good correlation with experimental data and were kept constant for all models. The standard $k-\varepsilon$ turbulence model was used with standard empirically derived model constants ($C_{I\varepsilon} = 1.44$, $C_{2\varepsilon} = 1.92$, $C_{\mu} = 0.09$, $\sigma_k = 1.0$, and $\sigma_{\varepsilon} = 1.3$) developed by Jones and Launder (1972). For the solution methods, SIMPLE was used for the velocity-pressure coupling scheme which is described in detail in appendix B using the pressure-based segregated algorithm. The spatial discretization scheme was set to least squares cell based, standard

discretization for the pressure term, and second order upwind for the momentum, turbulent kinetic energy, and turbulent dissipation rate terms. The solution was then initialized and run for a steady-state case until the convergence tolerance of 0.001 was met for continuity, x , y , and z velocities, turbulent kinematic energy k , and turbulent kinetic energy dissipation rate ε . All of the solution methods are described in further detail in appendix B.

This steady-state velocity field provided the basis from which the scalar was transported through the system. In order to analyze the scalar transport, a transient model was used given the converged steady-state velocity field as the initial conditions. Although, the velocity field changes through time, the major flow features are already developed. A user-defined function defining the scalar diffusivity (as discussed in Section 2.8, see e.g., equation 2.16) was introduced and the inlet concentration was set to a constant value of 1 (representing a non-dimensional concentration) to be progressed through time. Because the time step discretization was chosen to be first-order implicit, the solution was unconditionally stable regardless of time step size (discussed further in appendix B). The time step size would affect the accuracy of the solution in regards to scalar transport but was determined to produce the same results for a range of time step sizes from 0.1 to 10 s. For faster computational times, a time step size of 10 s was used throughout this study. To analyze the scalar transport characteristics, a monitor was created to determine the area-weighted average of the passive scalar at the system outlet.

3.2.1.3 Pipe Loop System Results and Conclusions

To further ensure solution convergence of the computational models, grid independence studies were performed, the full details of which are found in appendix C.

Figure 3.3 shows the contours of velocity magnitude displayed on the xz -plane through the pipe loop system operating at $0.001093 \text{ m}^3/\text{s}$ (or 16 gallons per minute (gpm) in English units).

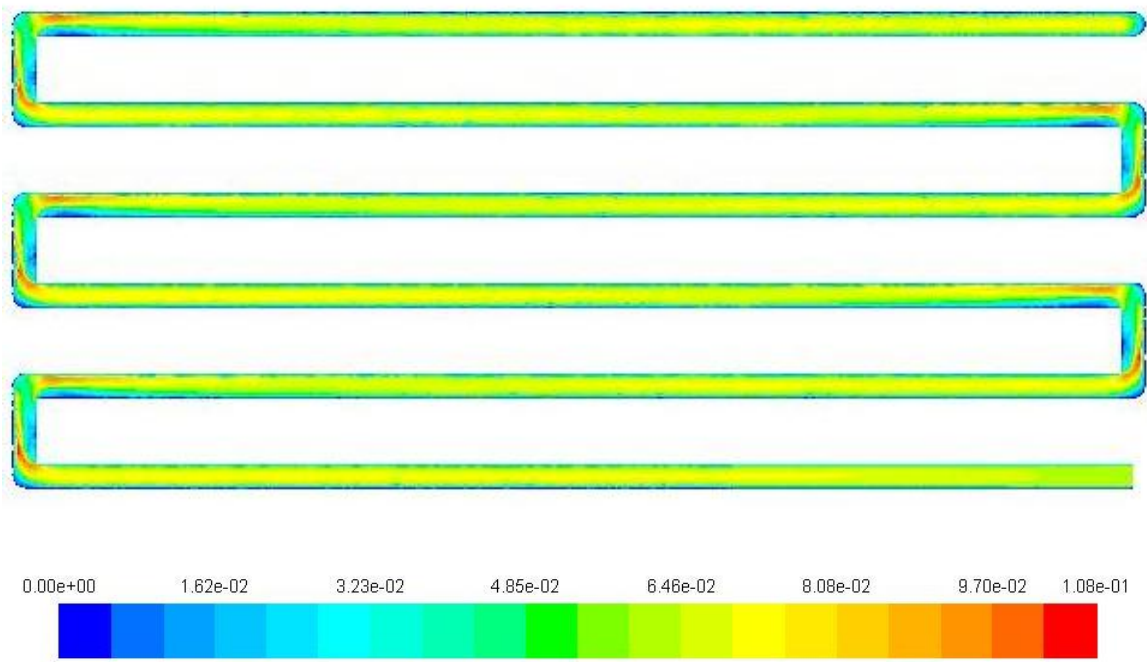


Figure 3.3 Contours of velocity magnitude (m/s) for pipe loop system operating at $0.001093 \text{ m}^3/\text{s}$ (16 gpm).

Figure 3.4 shows an enlarged portion of the pipe loop system that clearly shows flow separation in the corners due to the inertia. As the developed flow field approaches the corner, it attempts to continue in the same direction due to its momentum but encounters a wall causing the flow to accelerate and separate along the inner wall of the corner. Less severe regions of acceleration and separation are seen as the flow re-enters a

major length of the system due to the perturbed flow field. Once in the major length, the flow field returns to a fully developed profile relatively quickly.

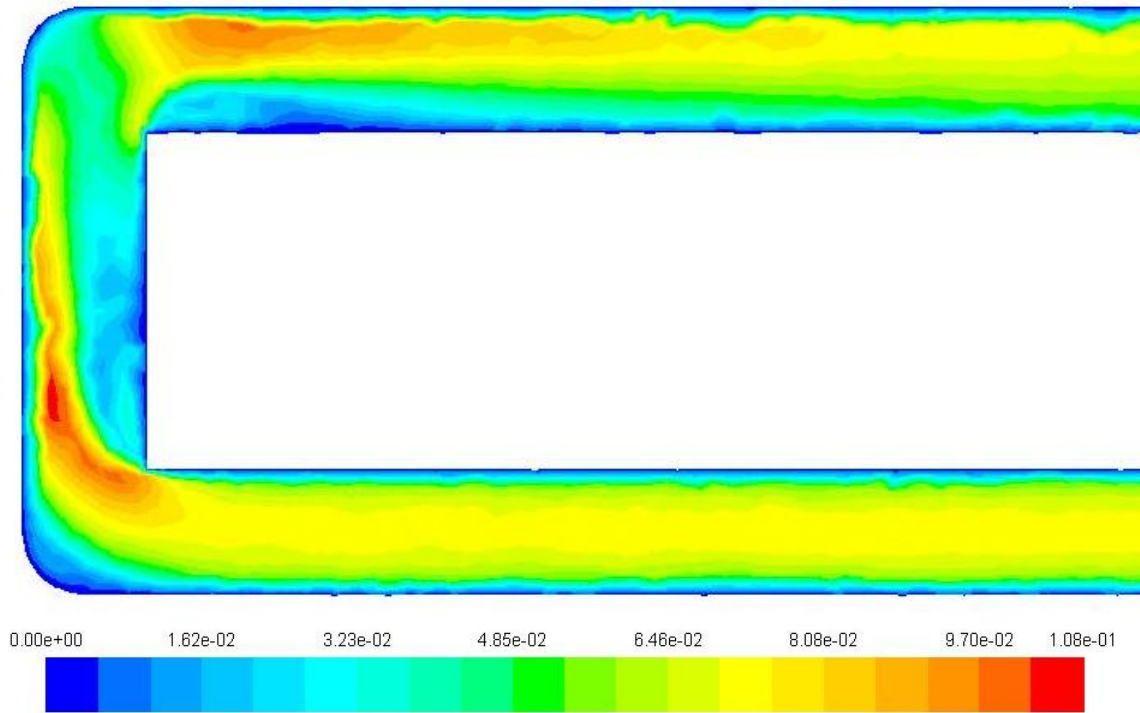


Figure 3.4 Contours of velocity magnitude (m/s) for a corner of the pipe loop system operating at $0.001093 \text{ m}^3/\text{s}$ (16 gpm).

Figure 3.5. shows the velocity vectors for the same portion of the pipe loop observed in Figure 3.4. The velocity vectors more clearly depict the regions of acceleration and recirculation.

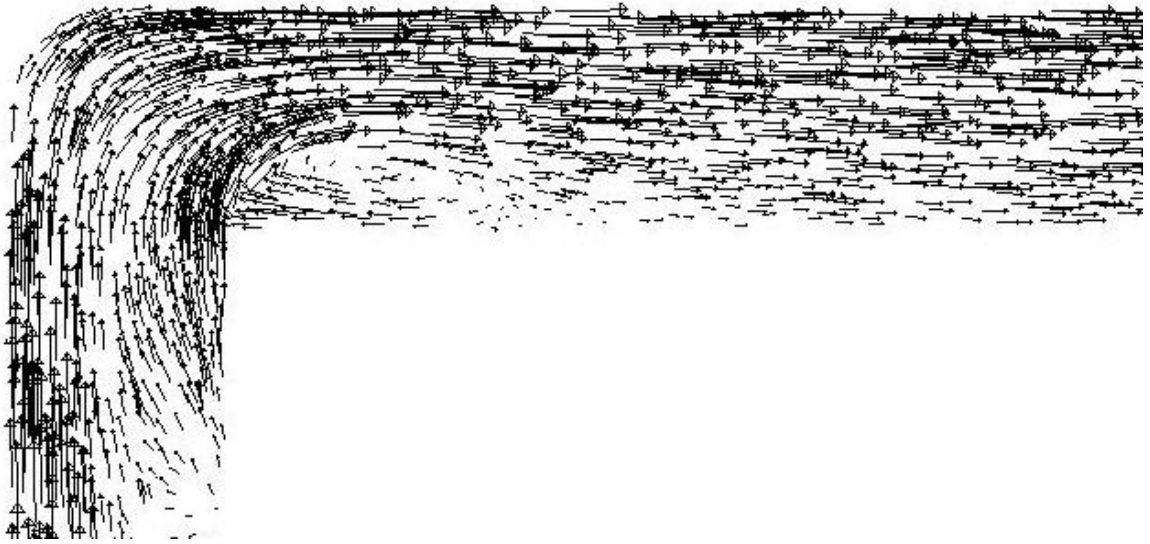


Figure 3.5 Velocity vectors for a corner of the pipe loop system operating at $0.001093 \text{ m}^3/\text{s}$ (16 gpm).

Determining the amount of turbulent mixing in a system can also aid in evaluating the degree to which a system departs from plug flow behavior. The magnitude of the turbulent viscosity is a result of the turbulent mixing the system imparts through inlet/outlet configurations or flow features inducing regions of separation or recirculation. In the case of the pipe loop, the regions of separation and recirculation seen in Figure 3.5 correspond to the areas of higher dynamic turbulent viscosity μ_t as seen in Figure 3.6.

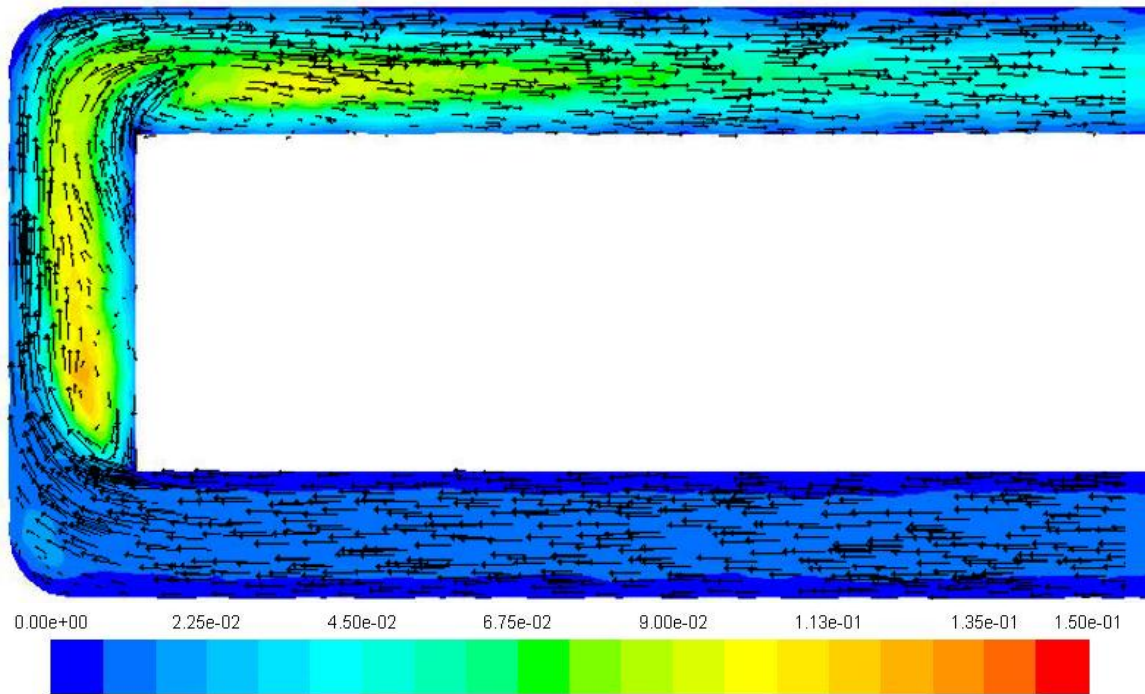


Figure 3.6 Contours of dynamic turbulent viscosity (kg/m-s) and velocity vectors for a corner of the pipe loop system operating at $0.001093 \text{ m}^3/\text{s}$ (16 gpm).

As observed in Figures 3.3, 3.4, 3.5, and 3.6, the dead zones are small in comparison to the regions dominated by advection. These flow dynamics lead to a system that is hydraulically efficient at mixing quantities (e.g., passive scalars, conservative tracers, or chlorine-containing species) through the system which is why pipe loops are considered ideal plug flow reactors. In the scalar transport model, the flow acceleration in the corners is seen to have a direct influence on the passive scalar transport through the system. The scalar field accelerates through the corners but evens out as the flow returns to a developed profile. Figures 3.7(a)-(h) depict the scalar field as it is transported through the pipe loop system for a flow rate of $0.001093 \text{ m}^3/\text{s}$ (16 gpm).

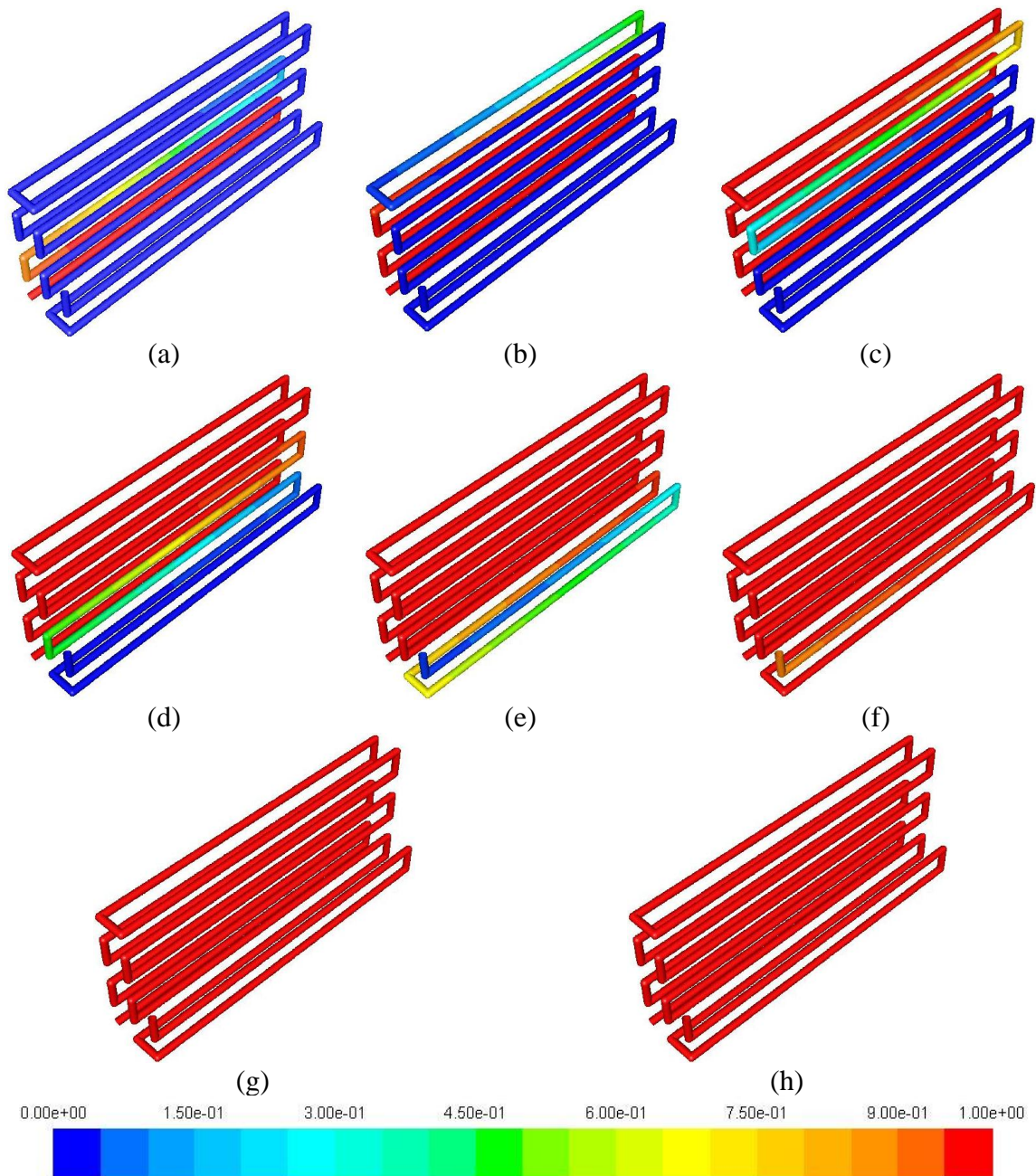


Figure 3.7 Contours of scalar concentration for pipe loop system operating at $0.001093 \text{ m}^3/\text{s}$ (16 gpm) for (a) $t = 300 \text{ s}$, (b) $t = 600 \text{ s}$, (c) $t = 900 \text{ s}$, (d) $t = 1200 \text{ s}$, (e) $t = 1500 \text{ s}$, (f) $t = 1800 \text{ s}$, (g) $t = 2100 \text{ s}$, and (h) $t = 2400 \text{ s}$.

3.2.2 Pressurized Tank System Configuration

This system was constructed at Colorado State University’s hydraulics laboratory at the Engineering Research Center. The pressurized tank system was constructed using

industry standard 0.3 m³ (80 gallon) fiberglass tanks connected using 0.03175 m diameter schedule 80 PVC pipe and plumbed in a manner that allowed multiple flow arrangements to be analyzed without altering the footprint of the system. The system was analyzed for 1, 2, and 3 tanks in series, respectively, as shown in Figure 3.8. The footprint of this system was also altered by placing all 6 tanks in series to facilitate analysis of 4, 5, and 6 tanks in series.



Figure 3.8 Pressurized Series Tank System at CSU’s ERC hydraulic laboratory.

The system was connected to a raw water supply fed from Horsetooth Reservoir in Fort Collins to the Engineering Research Center's hydraulic laboratory. The 3 series tank configuration was analyzed for 0.001262, 0.000946, 0.000631, and 0.000316 m³/s (20, 15, 10, and 5 gpm). The 6 series tank configuration was analyzed for 0.001893, 0.001262, 0.000946, and 0.000631 m³/s (30, 20, 15, and 10 gpm). A wide range of inlet pressures were observed depending on the desired flow rate. The inlet pressure for the maximum analyzed flow rate of 0.001893 m³/s (30 gpm) was approximately 414 kPa (60 psi). The fiberglass tanks have a maximum pressure rating of 552 kPa (80 psi) and thus

the system was limited via a pressure relief valve to 483 kPa (70 psi). Higher pressures were needed to drive flow through the systems as a result of the observed pressure losses discussed further in Subsection 3.2.2.3 and quantified through the hydraulic model presented in appendix D.

3.2.2.1 Pressurized Tank System Computational Model Setup

Using ANSYS DesignModeler the following models were created for the two footprints of 2 sets of 3 tanks in series and 6 tanks in series as seen in Figures 3.9(a) and (b), respectively.

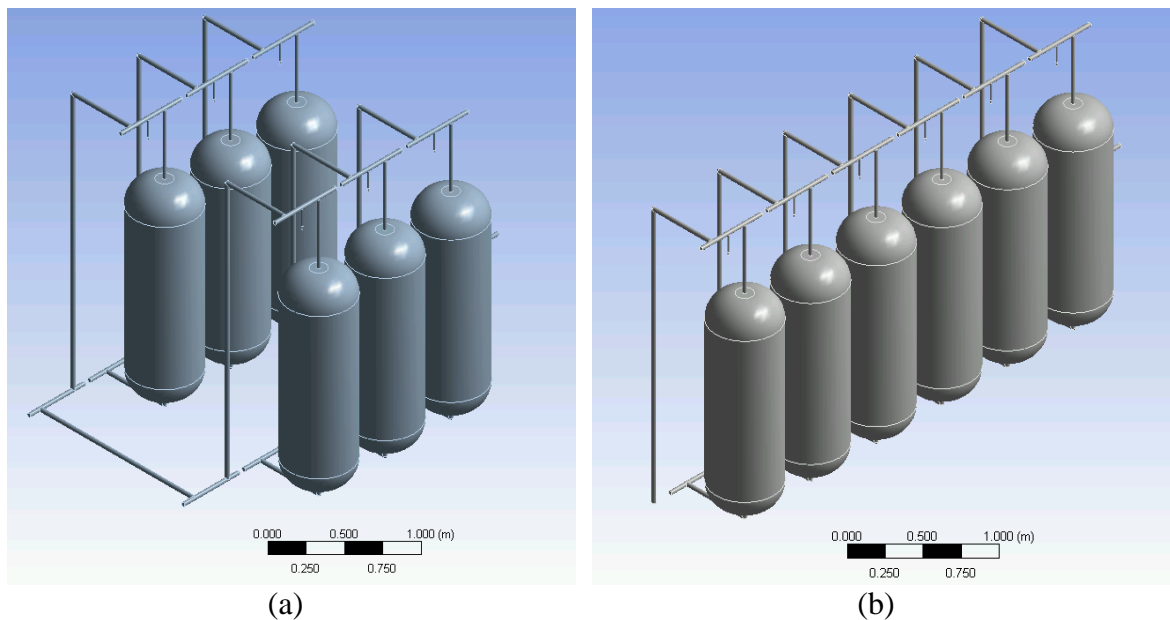


Figure 3.9 Pressurized tank configurations for (a) 3 series and (b) 6 series systems for CFD analysis.

The model with 2 sets of 3 tanks in series was meshed using ANSYS Meshing using the fluid dynamic automated procedure producing an unstructured tetrahedral mesh of 2,104,000 cells. The model of 6 tanks in series was meshed using the same procedure

producing an unstructured tetrahedral mesh of 1,800,000 cells. Figure 3.10 displays a region of the unstructured tetrahedral mesh used for the pressurized tank systems.

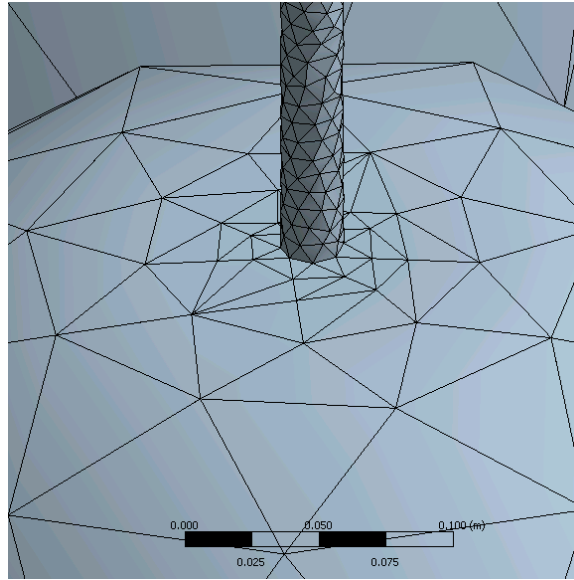


Figure 3.10. Unstructured tetrahedral mesh for pressurized tank systems.

3.2.2.2 Pressurized Tank System FLUENT Setup

The FLUENT setup for the pressurize tank system configuration followed the same procedure as described for the pipe loop system except the monitor for the area-weighted average of the passive scalar was varied depending on the number of tanks in series to be analyzed.

3.2.2.3 Pressurized Tank System Results and Conclusions

The grid independence studies for both of these systems can also be found in appendix C.

Figure 3.11 shows the contours of velocity magnitude for the 3 series tank system operating at $0.001262 \text{ m}^3/\text{s}$ (20 gpm) about a xz -plane cut through the center of the tanks limiting the displayed maximum velocity to 1 m/s.

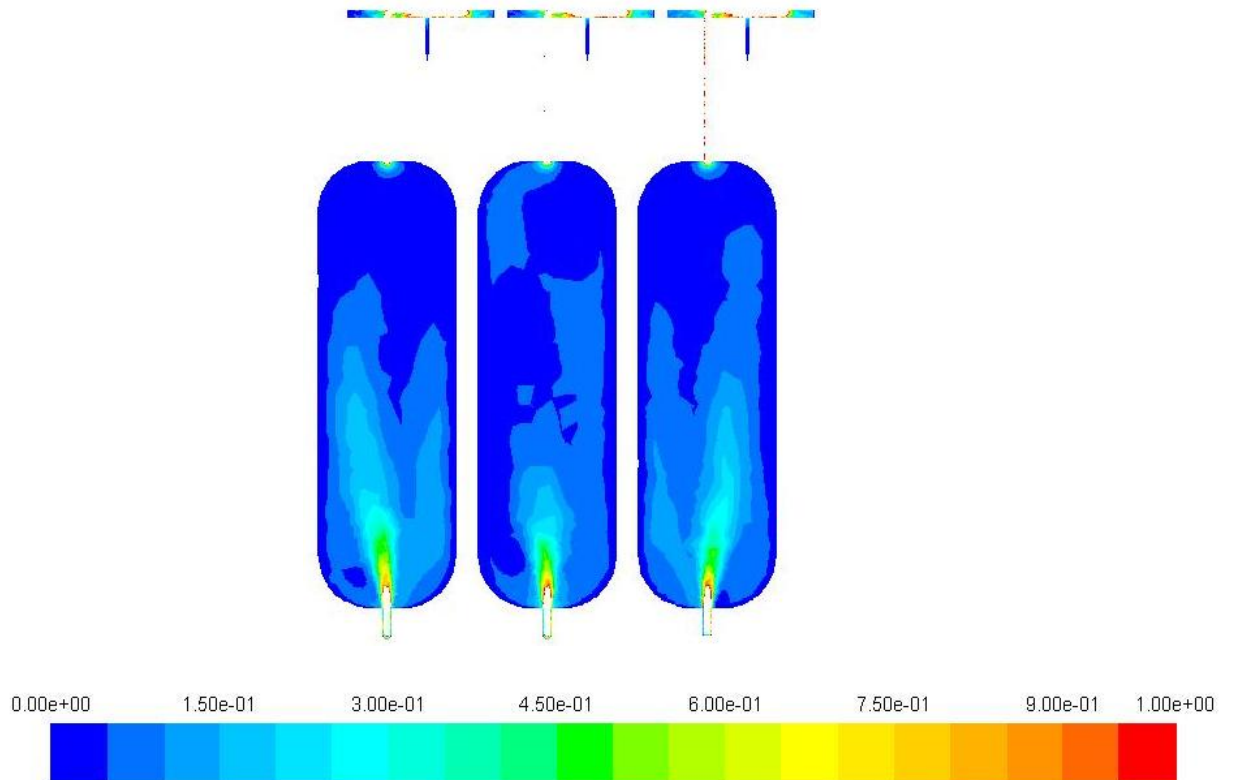


Figure 3.11 Contours of velocity magnitude (m/s) for the 3 series tank system operating at $0.001262 \text{ m}^3/\text{s}$ (20 gpm).

The maximum velocities in the pressure tank systems occur at the entrance to the tanks where flow exits a small pipe into a larger tank carrying much of its momentum with it into the tank in the form of a jet. Figure 3.12 show the velocity vectors for the 3 tank system about the xz -plane through the center of the tanks.

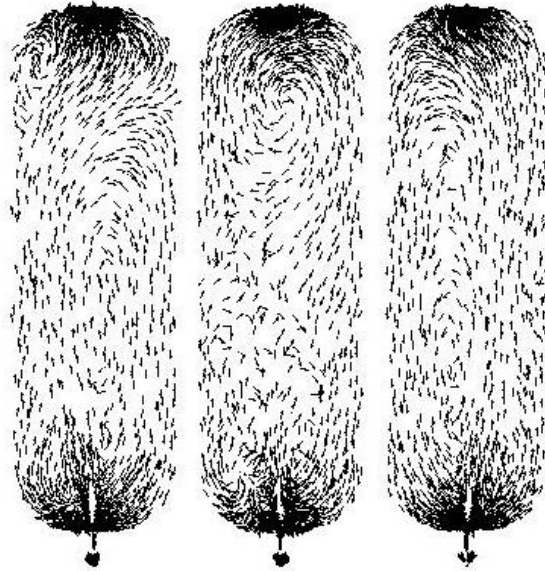


Figure 3.12 Velocity vectors for the 3 series tank system operating at 0.001262 m³/s (20 gpm).

To give a more complete picture of the velocity field, Figure 3.13 shows the velocity vectors about a xy -plane cut through the tanks 1 m from the bottom. These velocity vectors clearly show circulation regions around the perimeter, indicators of a swirling behavior in the tanks.



Figure 3.13 Velocity vectors for the 3 series tank system operating at 0.001262 m³/s (20 gpm).

Figure 3.14 displays the dynamic turbulent viscosity μ_t for the 3 tank system operating at 0.001262 m³/s (20 gpm) and limited to a displayed maximum value of 1.25 kg/m-s.

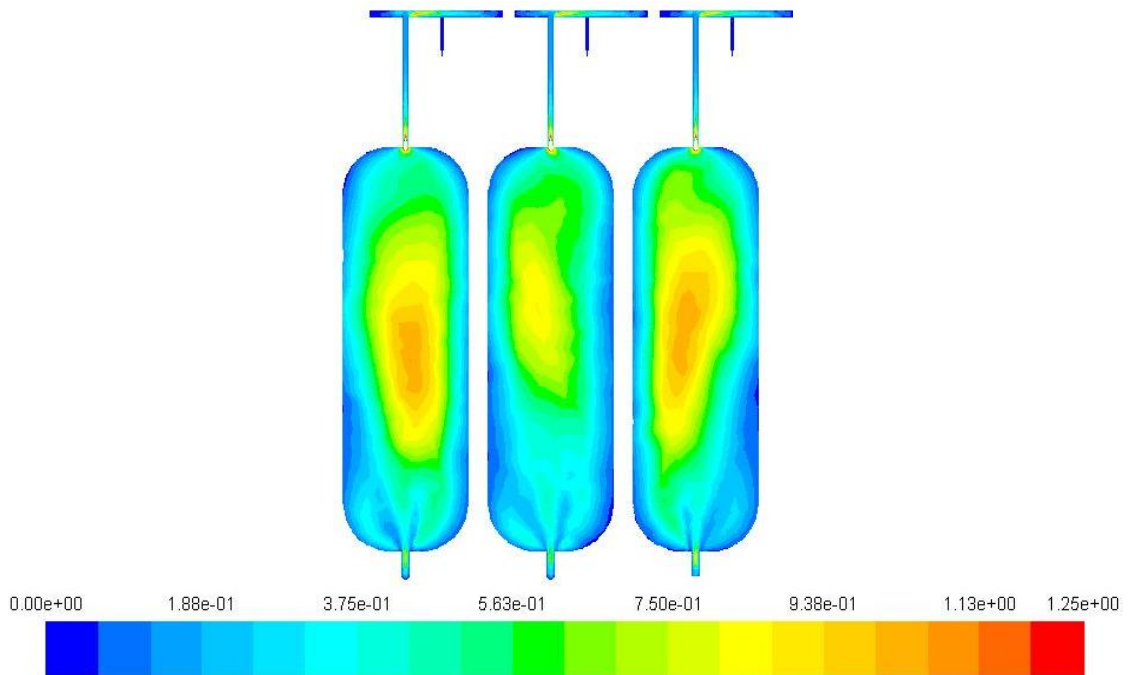


Figure 3.14 Contours of dynamic turbulent viscosity (kg/m-s) for the 3 series tank system operating at $0.001262 \text{ m}^3/\text{s}$ (20 gpm).

For the 3 series pressure tank system, the turbulent viscosity is more than three orders of magnitude large than the molecular viscosity of water in the system. These regions of higher turbulent viscosity correspond to the regions of higher mixing as observed through the velocity vectors in Figures 3.12 and 3.13.

Figures 3.15(a)-(h) display the contours of scalar concentration for the time-stepping transient solution to the RANS model as driven by the velocity field.

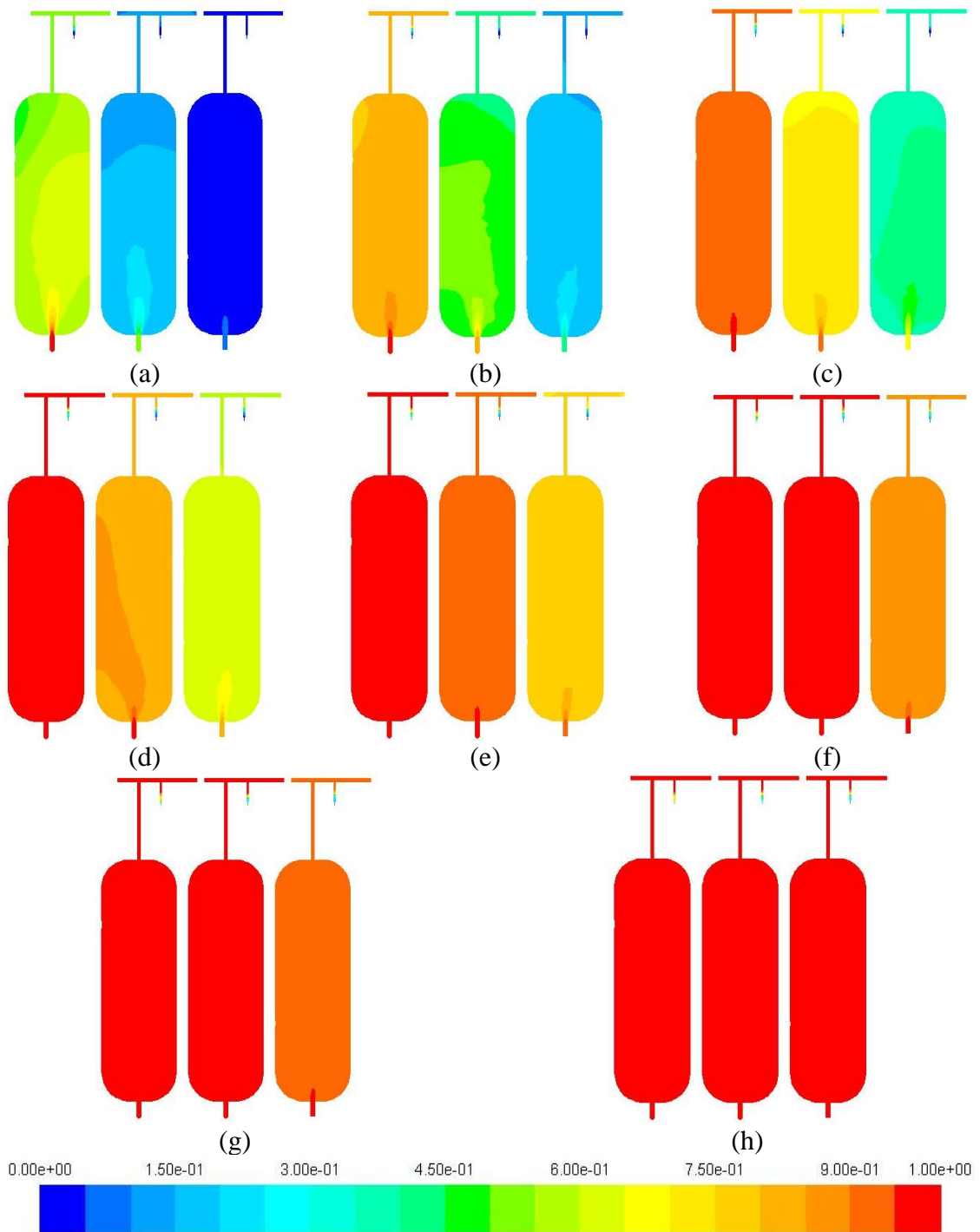


Figure 3.15 Contours of scalar concentration for 3 series tank system operating at $0.001262 \text{ m}^3/\text{s}$ (20 gpm) for (a) $t = 250 \text{ s}$, (b) $t = 500 \text{ s}$, (c) $t = 750 \text{ s}$, (d) $t = 1000 \text{ s}$, (e) $t = 1250 \text{ s}$, (f) $t = 1500 \text{ s}$, (g) $t = 1750 \text{ s}$, and (h) $t = 2000 \text{ s}$.

While it is known that the flow dynamics drive the transport of a passive scalar through a system, Figure 3.16 shows the scalar transport field for a time of 250 s overlain

with the velocity vectors. It can be observed that areas of recirculation in the tank correspond to a lower value of scalar concentration. The scalar follows the flow path in the most direct route from the inlet to the outlet. While there are no true dead zones in these tanks, the spherical geometries at the tops and bottoms of the tanks force mixing within the flow. The regions experiencing circulation increase in scalar concentration slower than the direct flow paths which lead to a system not nearly as efficient as the pipe loop system.

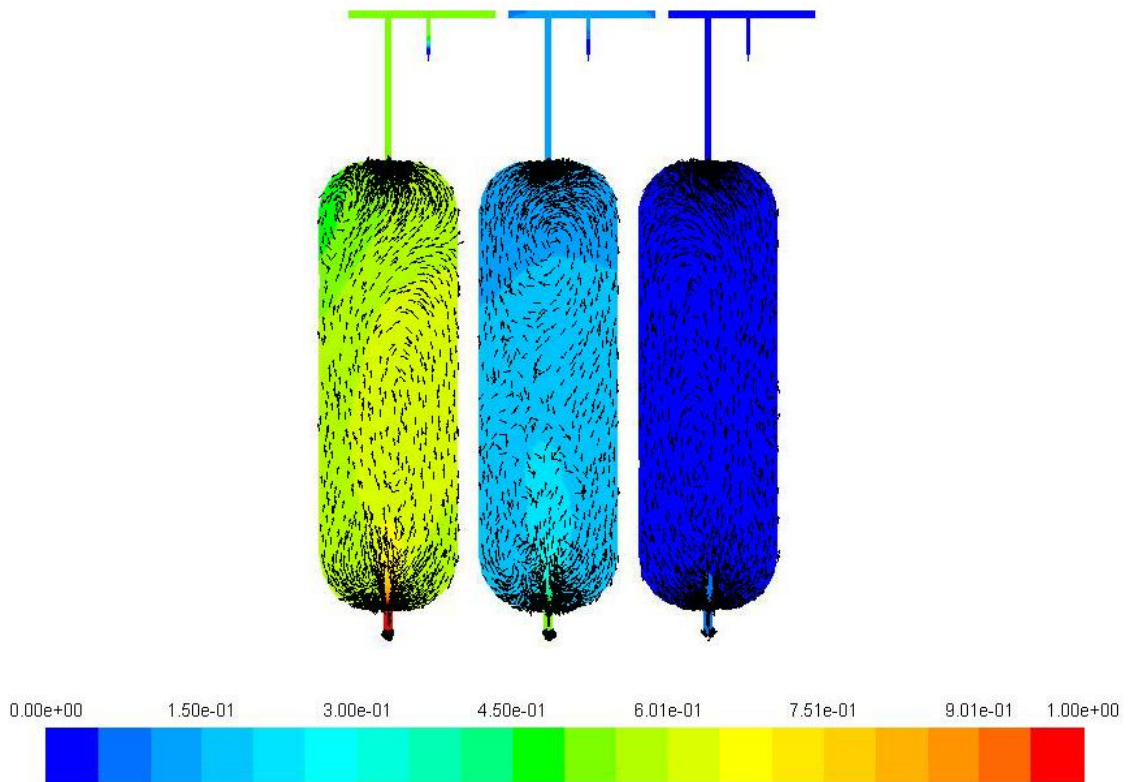


Figure 3.16 Scalar transport field at $t = 250$ s and velocity vectors for the 3 series tank system operating at $0.001262 \text{ m}^3/\text{s}$ (20 gpm).

Figure 3.17 shows the contours of velocity magnitude for the 6 series tank system operating at $0.001893 \text{ m}^3/\text{s}$ (30 gpm) about a xz -plane cut through the center of the tanks limiting the maximum velocity to 1 m/s.

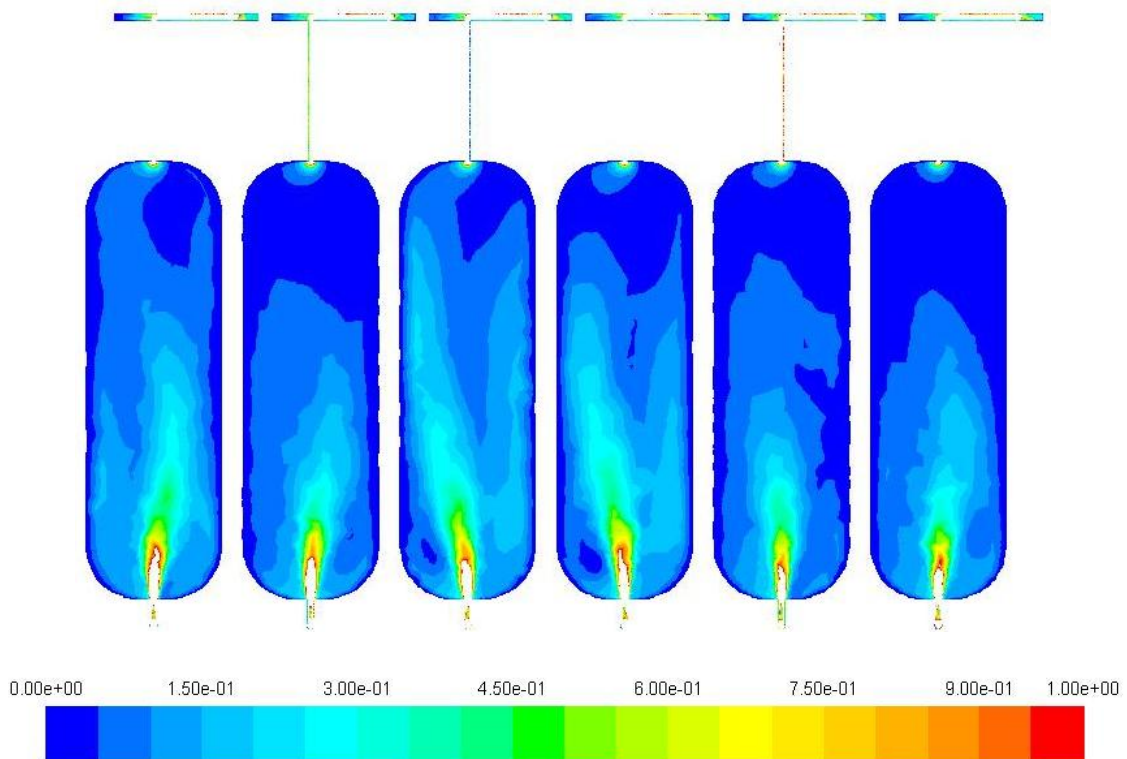


Figure 3.17 Contours of velocity magnitude (m/s) for the 6 series tank system operating at $0.001893 \text{ m}^3/\text{s}$ (30 gpm).

The highest velocity in these pressure tank systems is once again seen at the entrance to the tanks where flow exits a small pipe into a larger tank carrying much of its momentum with it into the tank in the form of a jet. Figure 3.18 shows the velocity vectors for the 6 tank system about the xz -plane through the center of the tanks. As seen with the 3 tank system, the 6 tank system exhibits the same general flow characteristics despite the more significant pressure losses observed by doubling the number of tanks in series.

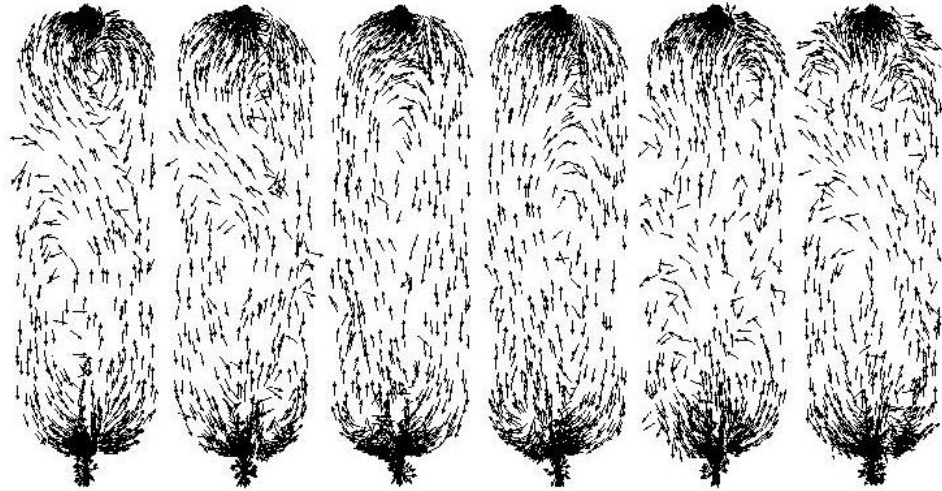


Figure 3.18 Velocity vectors for the 6 series tank system operating at $0.001893 \text{ m}^3/\text{s}$ (30 gpm).

Figure 3.19 displays the contours of turbulent dynamic viscosity for the 6 tank system limited to 2 kg/m-s .

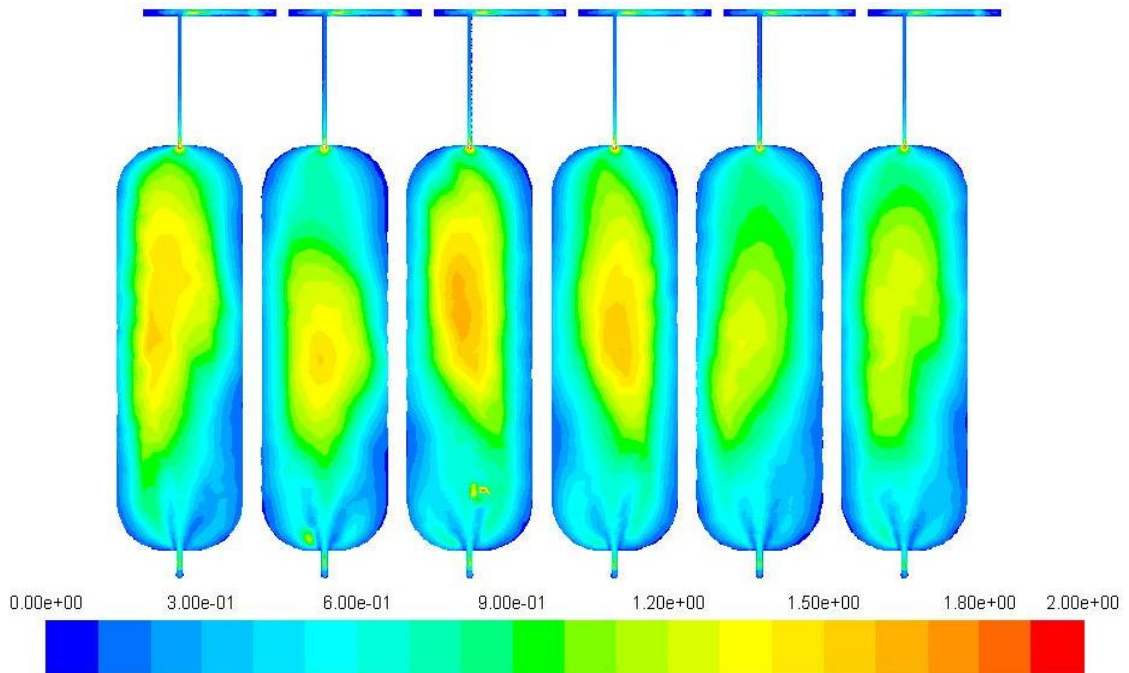


Figure 3.19 Contours of turbulent dynamic viscosity (kg/m-s) for the 6 series tank system operating at $0.001893 \text{ m}^3/\text{s}$ (30 gpm).

As expected, the increase in velocity within the same pressurized tanks resulted in intensified regions of turbulent mixing and associated higher values of turbulent viscosity. Figures 3.20 (a)-(h) display the contours of scalar concentration for the time-stepping transient solution to the RANS model as driven by the velocity field.

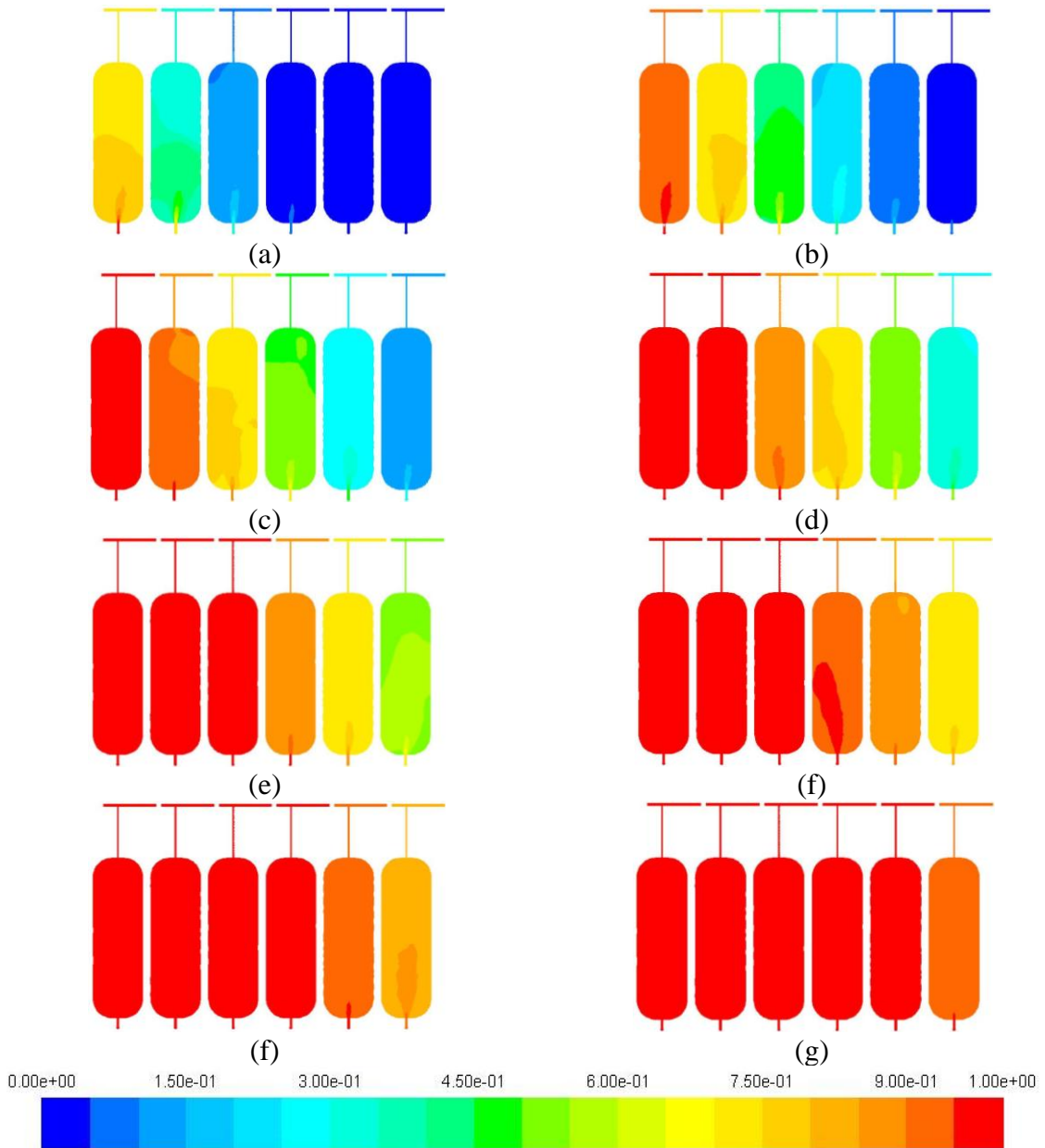


Figure 3.20 Contours of scalar concentration for 6 series tank system operating at $0.001893 \text{ m}^3/\text{s}$ (30 gpm) for (a) $t = 250 \text{ s}$, (b) $t = 500 \text{ s}$, (c) $t = 750 \text{ s}$, (d) $t = 1000 \text{ s}$, (e) $t = 1250 \text{ s}$, (f) $t = 1500 \text{ s}$, (g) $t = 1750 \text{ s}$, and (h) $t = 2000 \text{ s}$.

Figure 3.21 shows the scalar transport field for a time of 750 s and corresponding velocity vectors.

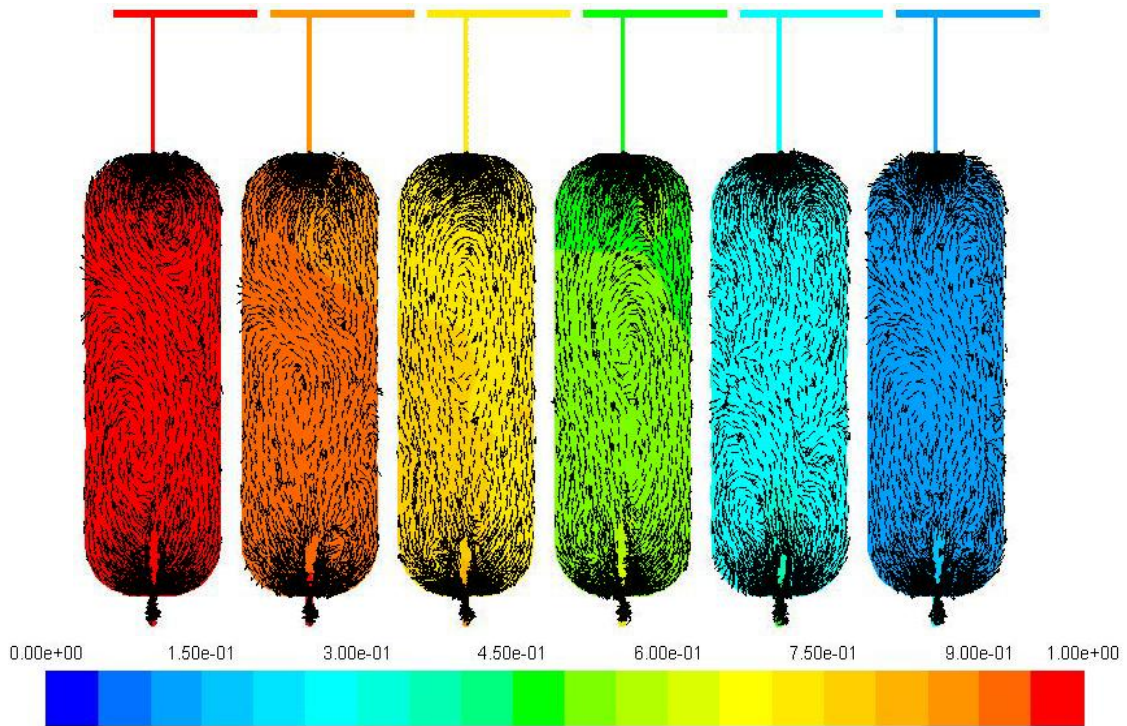


Figure 3.21 Scalar transport field at $t = 750$ s and velocity vectors for the 6 series tank system operating at $0.001893 \text{ m}^3/\text{s}$ (30 gpm).

Once again, the regions of lower scalar concentration in a given tank result from areas of recirculation.

3.2.2.3.1 Series Tank System Pressure Losses

A unique characteristic of the pressurized tank systems is the pressure losses observed through the tanks. Measurement of these pressure losses is important because of the apparent relationship between pressure and Reynolds stress. The greater the turbulent forces are in a system, the greater pressure is needed to drive flow through the system to overcome these Reynolds stress. Simple hydraulic models can be used to estimate the

major and minor losses through the systems. With these major and minor losses known, the losses through the tanks could be extrapolated. The complete details of the hydraulic loss model are contained in appendix D. Table 3.1 contains the measured values of pressure drop over each tank as a function of flow rate and Table 3.2 contains the hydraulic model predicted values of pressure drop over the series tank system based on the developed hydraulic model.

Table 3.1. Measured pressure losses for series pressurized tank systems

Flow Rate (m ³ /s)	Pressure Losses (kPa)					
	Tank 1	Tank 2	Tank 3	Tank 4	Tank 5	Tank 6
0.000063	1.27	2.04	2.41	3.12	3.88	4.26
0.000126	2.86	4.52	5.39	6.89	8.52	9.40
0.000189	4.77	7.44	8.93	11.30	13.94	15.44
0.000252	7.01	10.79	13.04	16.35	20.12	22.37
0.000315	9.57	14.58	17.71	22.04	27.07	30.19
0.000379	12.46	18.81	22.94	28.38	34.80	38.89
0.000442	15.67	23.47	28.74	35.36	43.29	48.50
0.000505	19.20	28.57	35.10	42.98	52.55	58.99
0.000568	23.06	34.11	42.03	51.24	62.58	70.37
0.000631	27.24	40.09	49.52	60.15	73.38	82.64
0.000694	31.75	46.50	57.57	69.70	84.95	95.80
0.000757	36.58	53.35	66.19	79.89	97.29	109.86
0.000820	41.73	60.64	75.37	90.73	110.40	124.80
0.000883	47.21	68.36	85.12	102.20	124.28	140.64
0.000946	53.01	76.52	95.43	114.32	138.93	157.37
0.001009	59.14	85.12	106.30	127.08	154.34	174.98
0.001073	65.59	94.16	117.74	140.49	170.53	193.49
0.001136	72.37	103.63	129.74	154.54	187.49	212.89
0.001199	79.47	113.54	142.31	169.23	205.21	233.18
0.001262	86.89	123.89	155.44	184.56	223.71	254.36

Table 3.2. Predicted pressure losses for series pressurized tank systems

Flow Rate (m ³ /s)	Pressure Losses (kPa)					
	Tank 1	Tank 2	Tank 3	Tank 4	Tank 5	Tank 6
0.000063	1.03	1.61	2.19	2.77	3.35	3.93
0.000126	2.41	3.69	4.97	6.25	7.53	8.82
0.000189	4.13	6.24	8.34	10.44	12.54	14.64
0.000252	6.21	9.25	12.28	15.32	18.35	21.39
0.000315	8.63	12.72	16.80	20.89	24.98	29.06
0.000379	11.40	16.65	21.90	27.15	32.40	37.65
0.000442	14.51	21.04	27.57	34.10	40.63	47.16
0.000505	17.97	25.89	33.81	41.74	49.66	57.58
0.000568	21.78	31.21	40.63	50.06	59.48	68.91
0.000631	25.93	36.97	48.02	59.06	70.10	81.15
0.000694	30.43	43.20	55.97	68.75	81.52	94.30
0.000757	35.27	49.89	64.50	79.12	93.73	108.35
0.000820	40.46	57.03	73.60	90.17	106.74	123.31
0.000883	45.99	64.63	83.26	101.90	120.54	139.17
0.000946	51.87	72.69	93.50	114.31	135.12	155.94
0.001009	58.09	81.20	104.30	127.40	150.51	173.61
0.001073	64.66	90.17	115.67	141.17	166.68	192.18
0.001136	71.57	99.59	127.61	155.62	183.64	211.65
0.001199	78.83	109.47	140.11	170.75	201.39	232.03
0.001262	86.43	119.81	153.18	186.56	219.93	253.30

Figure 3.22 displays a comparison of the predicted and measured values of pressure loss over the system.

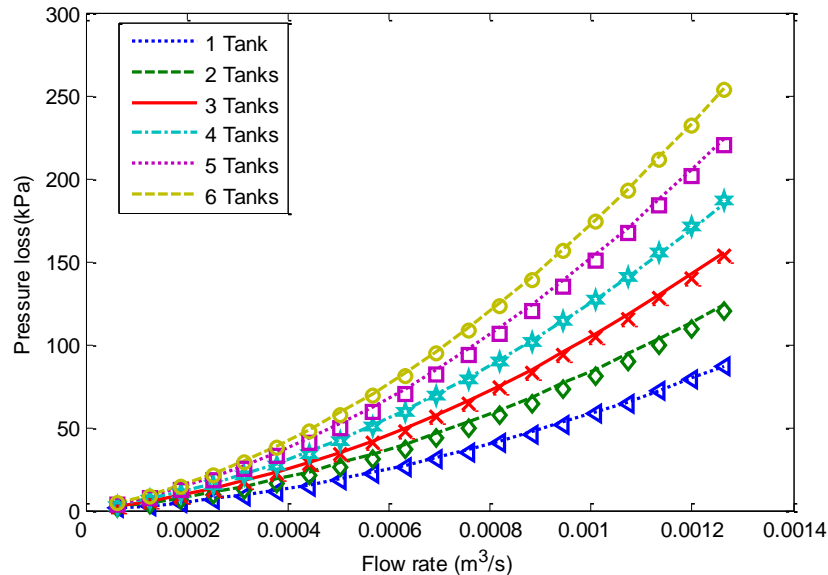


Figure 3.22 Predicted and measured pressure losses over the pressurized series tank systems.

The hydraulic model produced pressure loss values that closely correlated to the measured values. As observed through Tables 3.1 and 3.2 and Figure 3.22, the pressure losses associated with the pressurized series tank system are quite significant. Other major losses were seen as a result of the static mixer, flow meters, improper plumbing, and the tanks themselves. Recommendations are made in chapter 5 for modifying the pressurized series tank systems to reduce the pressure losses and improve the operational capacity.

3.2.3 Open Surface Tank System Configuration

These systems were constructed at Colorado State University's hydraulics laboratory at the Engineering Research Center. One system was comprised of a 1.89 m³ (or 500 gallon) capacity vertical polyethylene tank with an inlet comprised of a 90 degree end tilted 45 degrees from horizontal towards the bottom of the tank and a pressure-break outlet from the top of the tank as pictured in Figure 3.23 (a). The other system was comprised of a 1.99 m³ (or 525 gallon) capacity horizontal polyethylene tank with a similar inlet and outlet as described for the vertical tank and shown in Figure 3.23 (b).



(a)

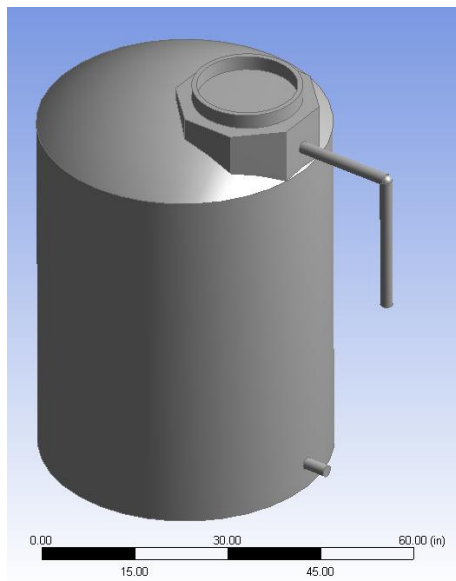


(b)

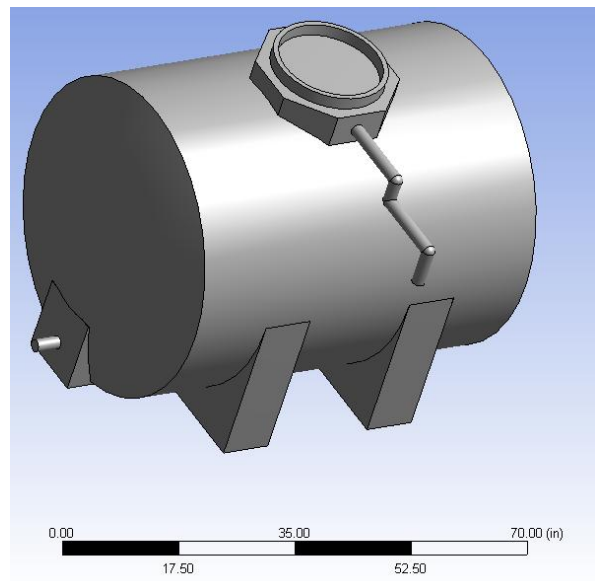
Figure 3.23 (a) Vertical open surface tank system and (b) horizontal open surface tank system at CSU's ERC hydraulic laboratory.

3.2.3.1 Open Surface Tank System Computational Model Setup

Using ANSYS DesignModeler the following models were created for the two polyethylene tanks show in Figures 3.24 (a) and (b).



(a)

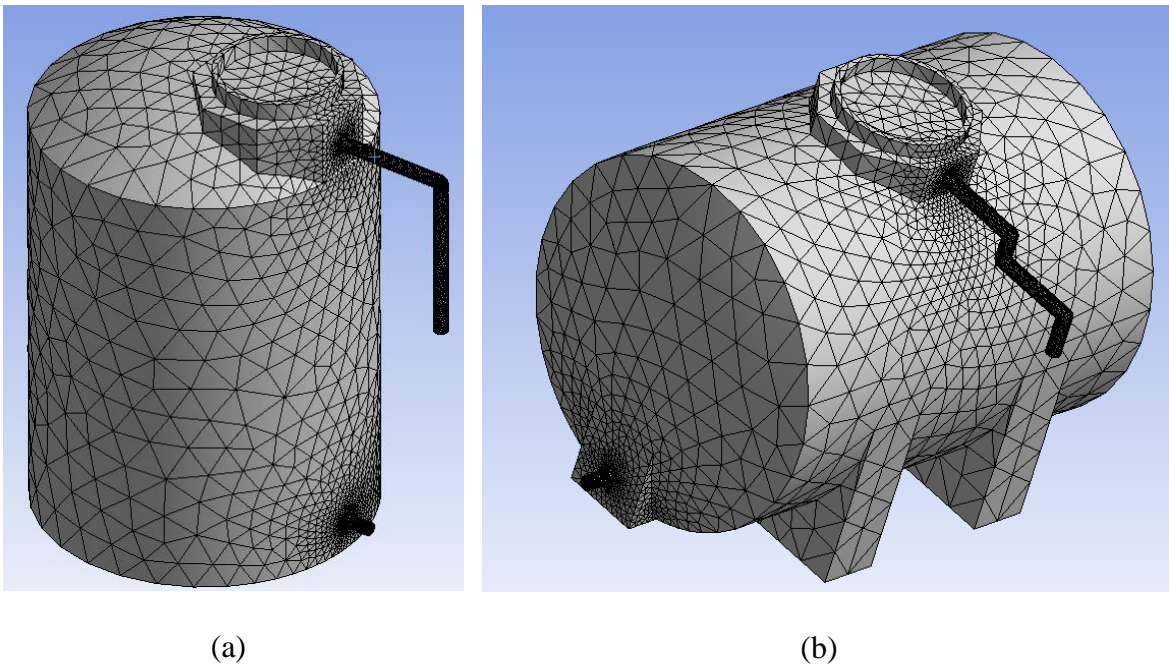


(b)

Figures 3.24 (a) Vertical open surface tank system and (b) horizontal open surface tank system model geometry for CFD analysis.

The differences between the prototype systems in Figures 3.23 (a) and (b) and the model geometry in Figures 3.24 (a) and (b) are evident. The simplifications in the model

geometry are a result of the difficulty in meshing a model with all of the nuances of the physical systems which created steep gradients in cell size ultimately leading to divergence in the computational model. Removing some of the features that were not significant to the flow dynamics provided smoother transition in mesh elements leading to a stable solution to the respective problems. Figures 3.25 (a) and (b) show the unstructured tetrahedral meshes used for CFD analysis of the vertical and horizontal open surface tank systems.



Figures 3.25 Unstructured tetrahedral mesh for (a) vertical and (b) horizontal open surface tank systems.

3.2.3.2 Open Surface Tank System FLUENT Setup

The FLUENT setup for the open surface tank system configurations followed the same procedure as described for the pipe loop system. Another simplification in modeling these open surface tanks was to model them as pressurized tanks which

significantly lowered the complexity yet yielded accurate results as compared to the physical experiments.

3.2.3.3 Open Surface Tank System Results and Conclusions

The complete grid independence studies for each of these respective systems are found in appendix C.

While the major hydrodynamic features remained the same for all of the flow rates, 0.000315, 0.000631, and 0.000946 m³/s (5, 10, and 15 gpm), they did vary in intensity. Figure 3.26 shows the contours of velocity magnitude for the vertical open surface tank system operating at 0.000946 m³/s (15 gpm) on a *xz*-plane through the middle of the tank limited to 0.1 m/s. Limiting the maximum velocity allows for visualization of velocity contours through the entire tank and not just the inlet and outlets (by continuity the velocities in the inlet and outlet sections are considerably greater than in the tank).

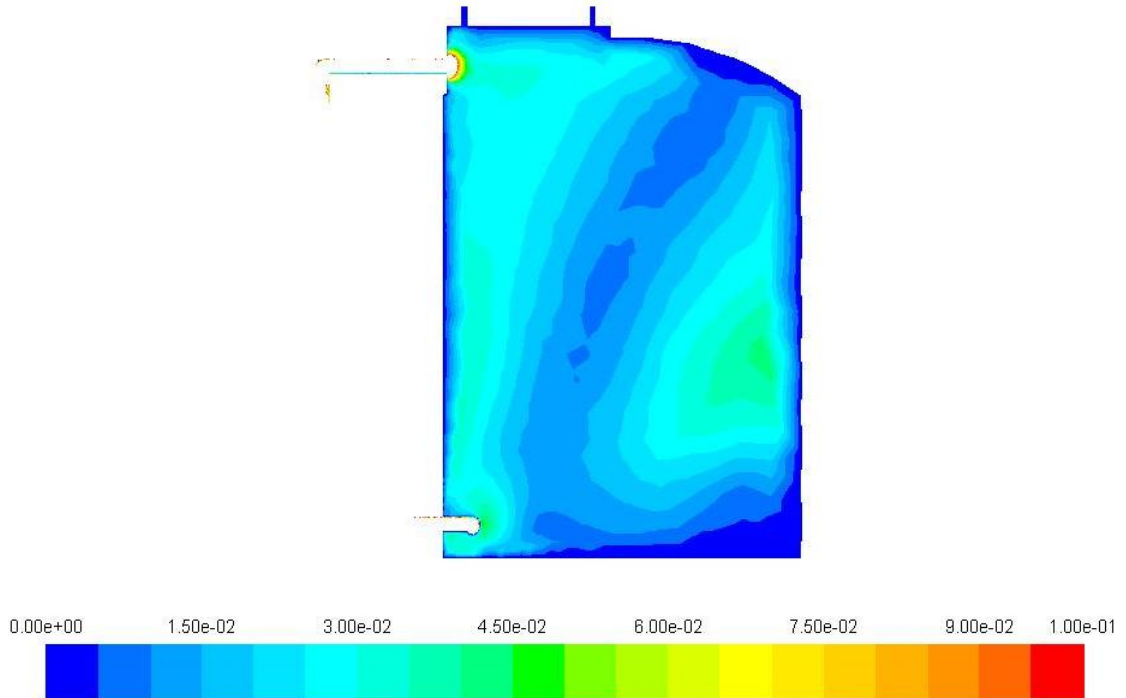


Figure 3.26 Contours of velocity magnitude (m/s) for vertical open surface tank system operating at $0.000946 \text{ m}^3/\text{s}$ (15 gpm).

The exact nature of the highly three dimensional flow field induced by the inlet condition is difficult to perceive in a two-dimensional plane but it is evident that the left and right (as observed in Figure 3.26) encounter greater velocities while the center portion of the tank experiences lower velocities. Figures 3.27, 3.28, and 3.29 depict the velocity vectors on the same plane as pictured above, about a xy -plane cut through the tank 0.1 m from the bottom, and about a xy -plane cut through the tank 1.5 m from the bottom, respectively.

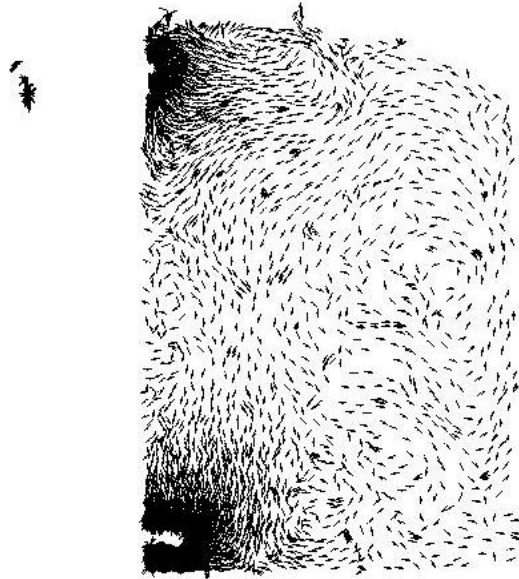


Figure 3.27 Velocity vectors for vertical open surface tank system operating at $0.000946 \text{ m}^3/\text{s}$ (15 gpm).

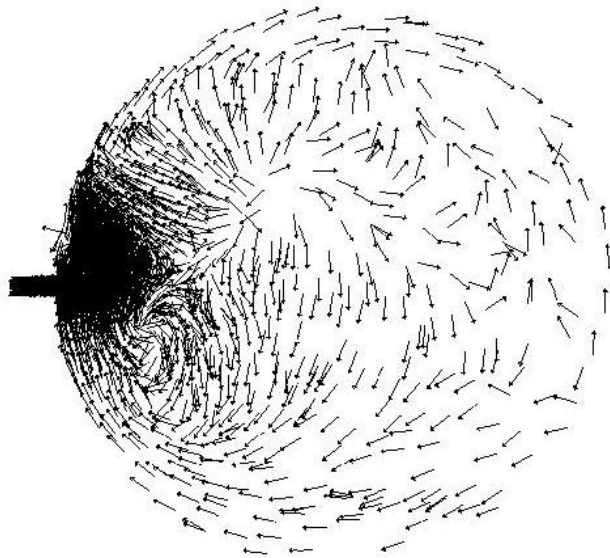


Figure 3.28 Velocity vectors for vertical open surface tank system operating at $0.000946 \text{ m}^3/\text{s}$ (15 gpm) about a xy-plane 0.1 m from the bottom surface.



Figure 3.29 Velocity vectors for vertical open surface tank system operating at $0.000946 \text{ m}^3/\text{s}$ (15 gpm) about a xy -plane 1.5 m from the bottom surface.

Figure 3.27 shows distinct regions of circulation in the tank. Figure 3.28 shows chaotic velocity vectors resulting from the inlet configuration in the tank but the beginnings of a spiraling circulation are seen along the perimeter of the tank 0.1 m from the bottom of the tank. Figure 3.29 shows a clear clockwise circulation pattern has developed 1.5 from the bottom of the tank. There is also a region of recirculation, or dead zone, observed near the right wall of the tank in Figure 3.27 which corresponds closely to the lower region of velocity observed in Figure 3.26. Figure 3.30 shows the three dimensional pathlines in the tank as transported by the velocity field from the inlet to the outlet and colored by residence time in the tank.

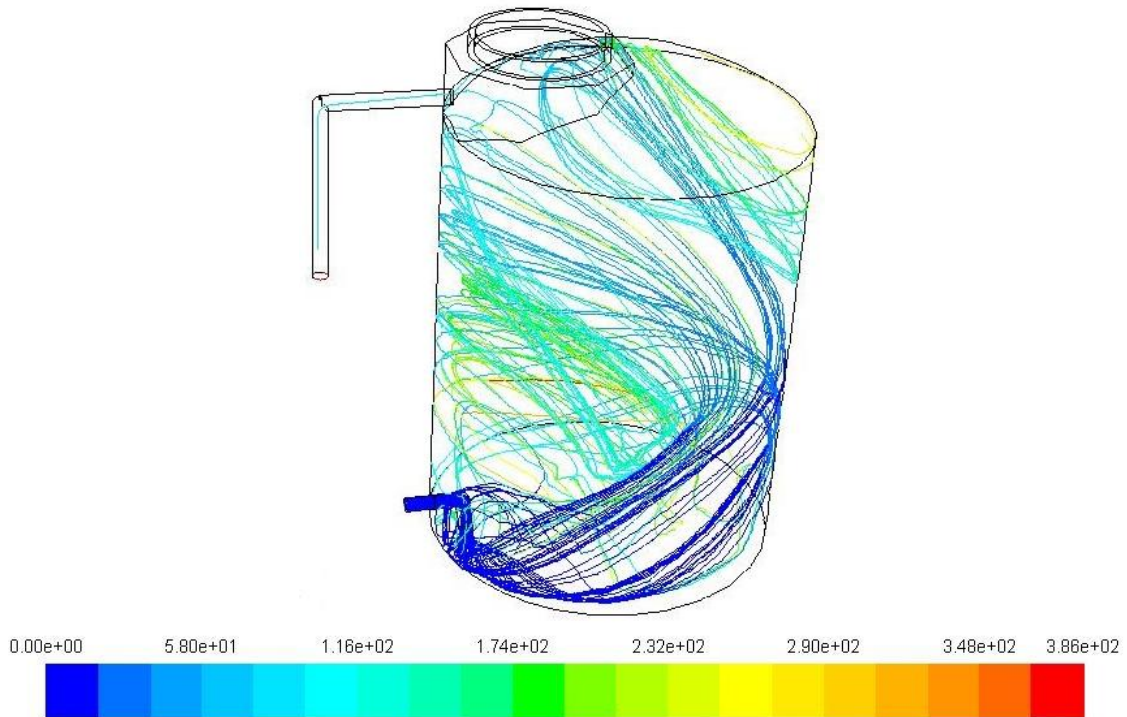


Figure 3.30 Three-dimensional pathlines of particle residence time (s) for vertical open surface system operating at $0.000946 \text{ m}^3/\text{s}$ (15 gpm).

The three-dimensional pathlines gives a better overall visual representation of the flow field seen in Figure 3.26. The nature of the flow circulates around the perimeter of the tank in the z -direction towards the tank outlet. The simplification in analyzing this tank as a pressurized system allows for the flow to be deflected by the tanks upper surface inducing some additional turbulent mixing in the system. Yet the scalar transport characteristics over the analyzed flow rates compared closely to the physical tracer study results. As discussed with the pressurized tank systems, the regions of higher turbulent viscosity in the vertical open surface tank correspond to the areas of higher mixing as observed in the velocity vectors in Figures 3.27.

Figure 3.31 displays the contours of turbulent viscosity on a xz -plane through the center of the vertical open surface tank.

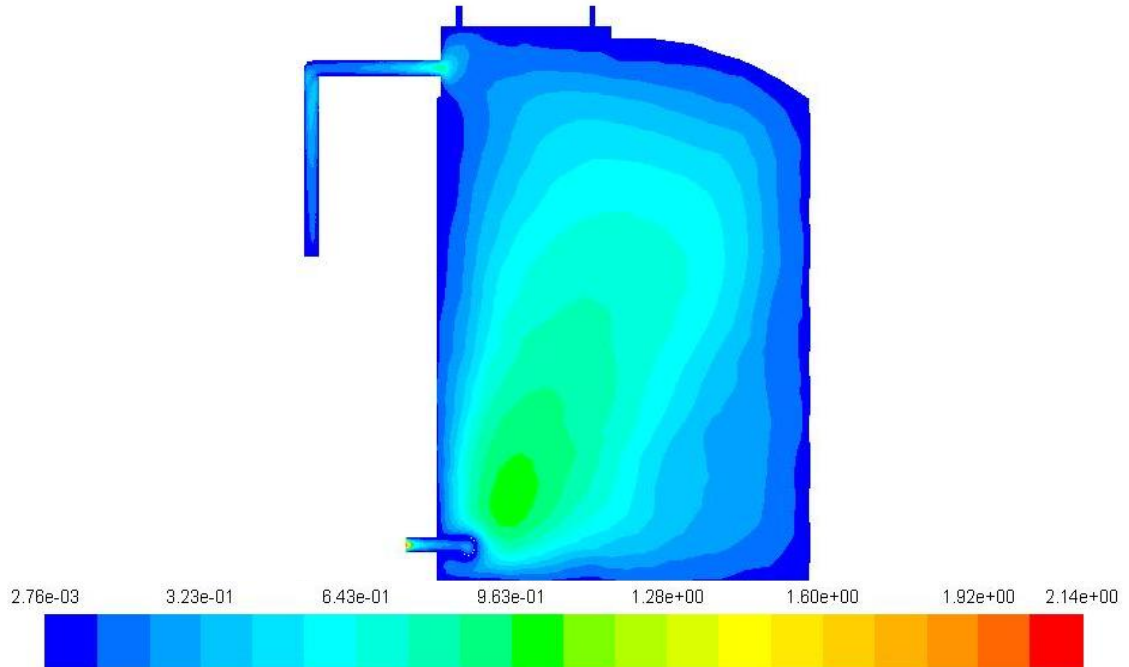


Figure 3.31 Contours of dynamic turbulent viscosity (kg/m-s) for the vertical open surface tank system operating at $0.000946 \text{ m}^3/\text{s}$ (15 gpm).

The values of higher turbulent viscosity correspond to the regions of greater mixing as observed in Figure 3.27.

Figures 3.32 (a)-(i) display the contours of scalar concentration for the time-stepping transient solution to the vertical open surface tank RANS model as driven by the highly three-dimensional velocity field.

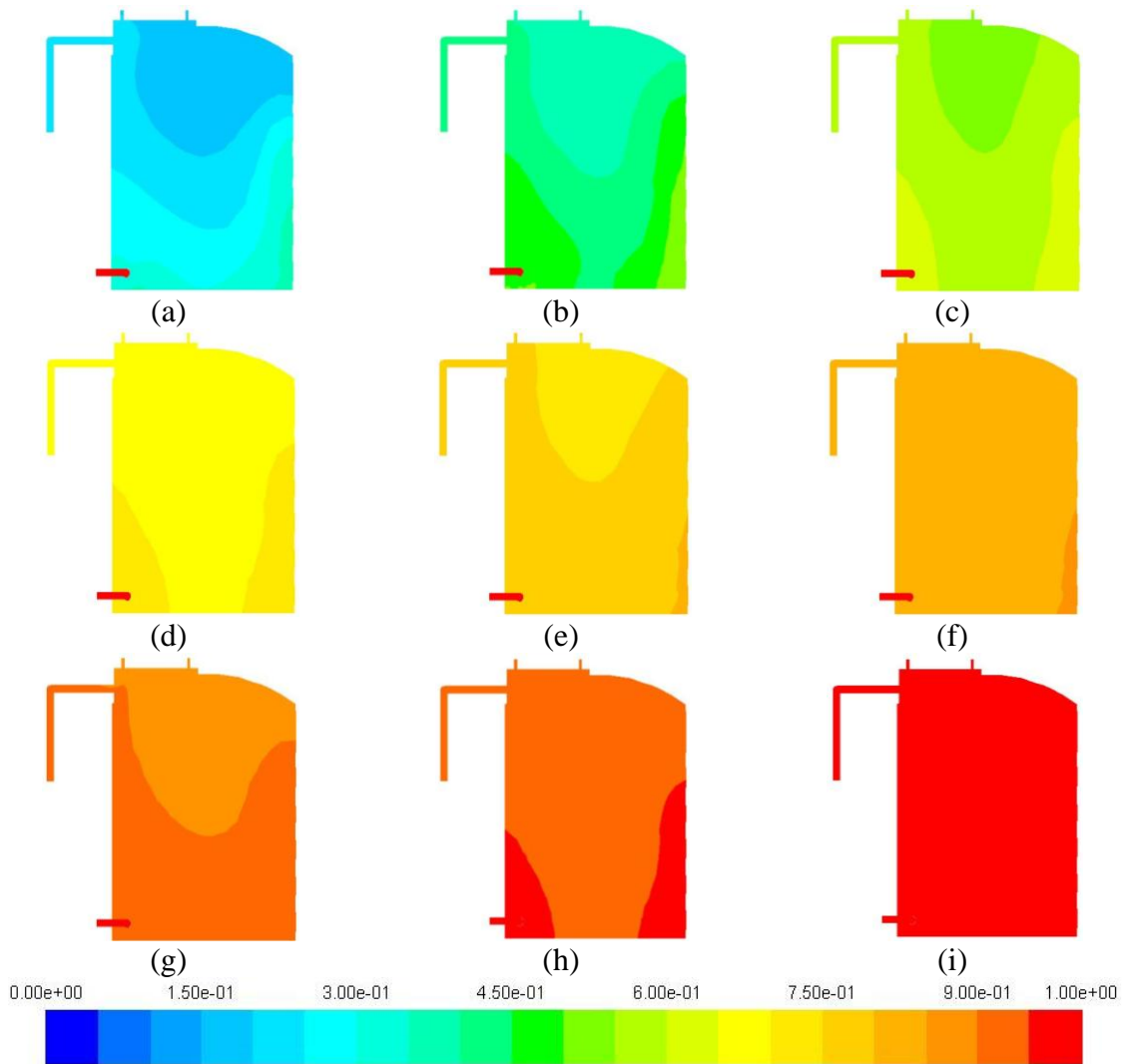


Figure 3.32 Contours of scalar concentration for vertical open surface tank system operating at $0.000946 \text{ m}^3/\text{s}$ (15 gpm) for (a) $t = 600 \text{ s}$, (b) $t = 1200 \text{ s}$, (c) $t = 1800 \text{ s}$, (d) $t = 2400 \text{ s}$, (e) $t = 3000 \text{ s}$, (f) $t = 3600 \text{ s}$, (g) $t = 4800 \text{ s}$, (h) $t = 6000 \text{ s}$, and (i) $t = 7800 \text{ s}$.

The scalar concentration, as seen on the depicted xz -plane, increases around the perimeter of the tank first. It takes much longer for the scalar to increase in the center portion of the tank because of the large region of circulation.

Figure 3.33 shows the scalar concentration in the vertical open surface tank system for a time of 1800 s overlain with the velocity vectors.

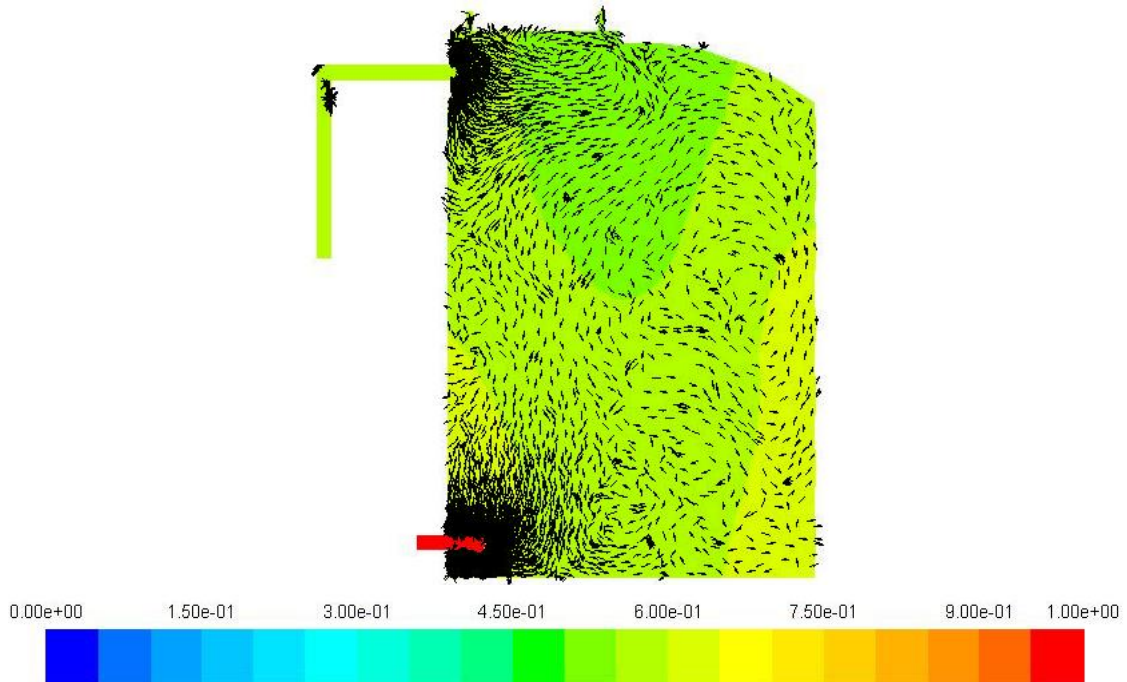


Figure 3.33 Scalar transport field at $t = 1800$ s and velocity vectors for vertical open surface tank system operating at $0.000946 \text{ m}^3/\text{s}$ (15 gpm).

It is more difficult to observe a relationship between the velocity vectors and scalar concentration about a xz -plane through the center of the tank. The scalar field is influenced greater by the flow circulation about the perimeter of the tank as observed in Figures 3.28, 3.29, and 3.30.

As in the vertical open surface tank, the major hydrodynamic features remained the same for all of the flow rates, 0.000315 , 0.000631 , and $0.000946 \text{ m}^3/\text{s}$ (5, 10, and 15 gpm), while varying in intensity. Figure 3.34 shows the contours of velocity magnitude for the horizontal open surface tank system operating at $0.000946 \text{ m}^3/\text{s}$ (15 gpm) on a xz -plane through the middle of the tank limited to 0.1 m/s .

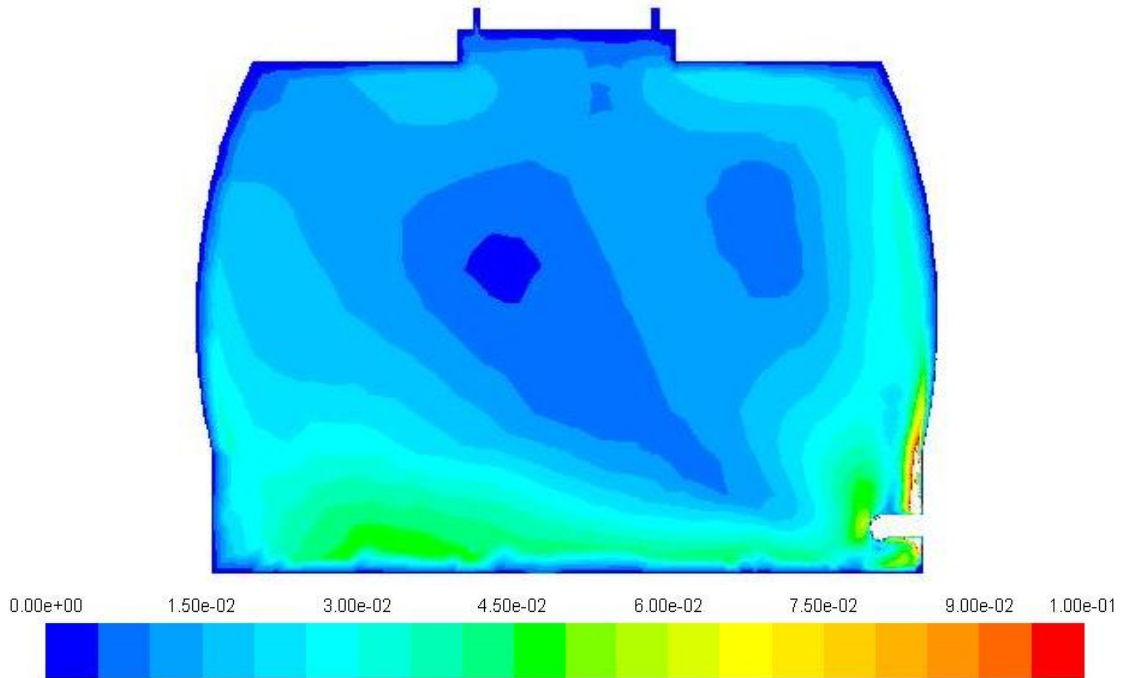


Figure 3.34 Contours of velocity magnitude (m/s) for horizontal open surface tank system operating at $0.000946 \text{ m}^3/\text{s}$ (15 gpm).

Figures 3.35 and 3.36 display the velocity vectors of the horizontal open surface tank operating at $0.000946 \text{ m}^3/\text{s}$ (15 gpm) about a xz -plane through the middle of the tank and a xy -plane 0.1 m from the bottom of the tank.

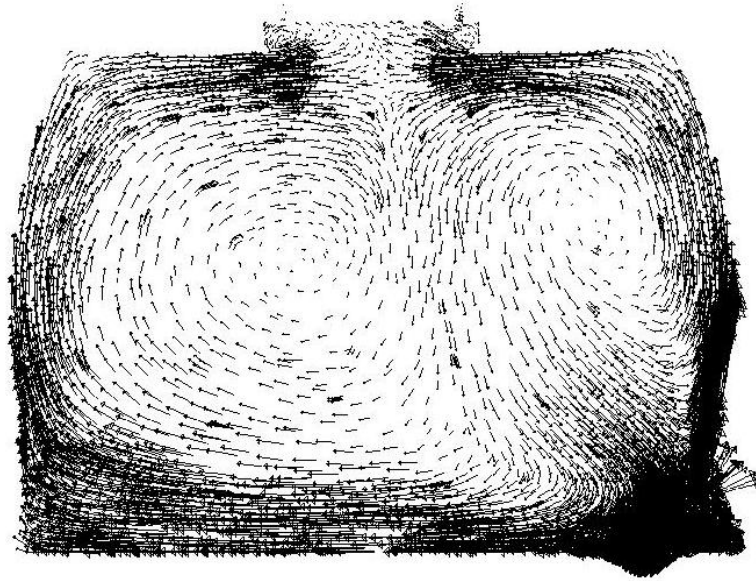


Figure 3.35 Velocity vectors for horizontal open surface tank system operating at $0.000946 \text{ m}^3/\text{s}$ (15 gpm).

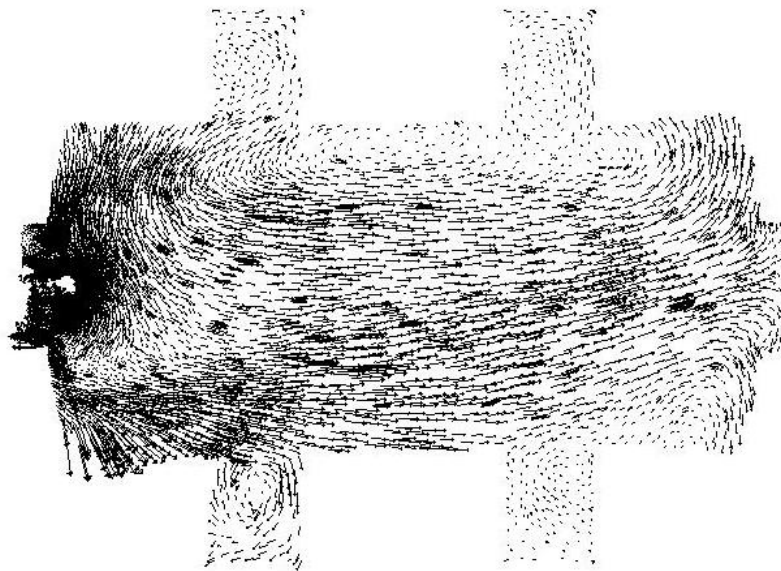


Figure 3.36 Velocity vectors for horizontal open surface tank system operating at $0.000946 \text{ m}^3/\text{s}$ (15 gpm) about a xy -plane 0.1 m from the bottom surface.

Figure 3.35 shows two distinct regions of circulation in middle of the tank about the xz -plane. Figure 3.36 shows chaotic velocity vectors resulting from the inlet configuration in the tank but the beginnings of a spiraling circulation are seen along the perimeter of the tank 0.1 m from the bottom of the tank and a clear flow path towards the far end of the

tank where the flow begins to spiral upward around the perimeter of the tank. Figure 3.37 shows the three dimensional pathlines in the tank as transported by the velocity field from the inlet to the outlet and colored by residence time in the tank.

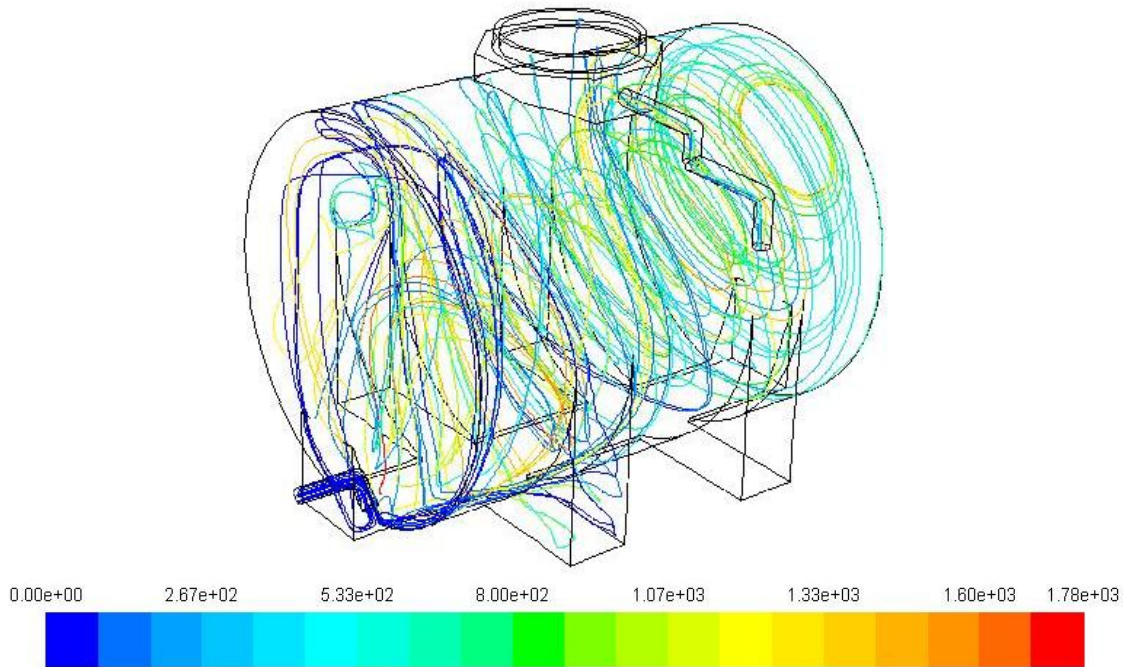


Figure 3.37 Three-dimensional pathlines of particle residence time (s) for horizontal open surface system operating at $0.000946 \text{ m}^3/\text{s}$ (15 gpm).

The three-dimensional pathlines give a better overall visual representation of the flow field seen in Figure 3.34 and the velocity vectors seen in Figures 3.35 and 3.36. The nature of the flow circulates around the perimeter of the tank in the z -direction towards the tank outlet.

Figure 3.38 displays the contours of turbulent dynamic viscosity on a xz -plane through the center of the tank.

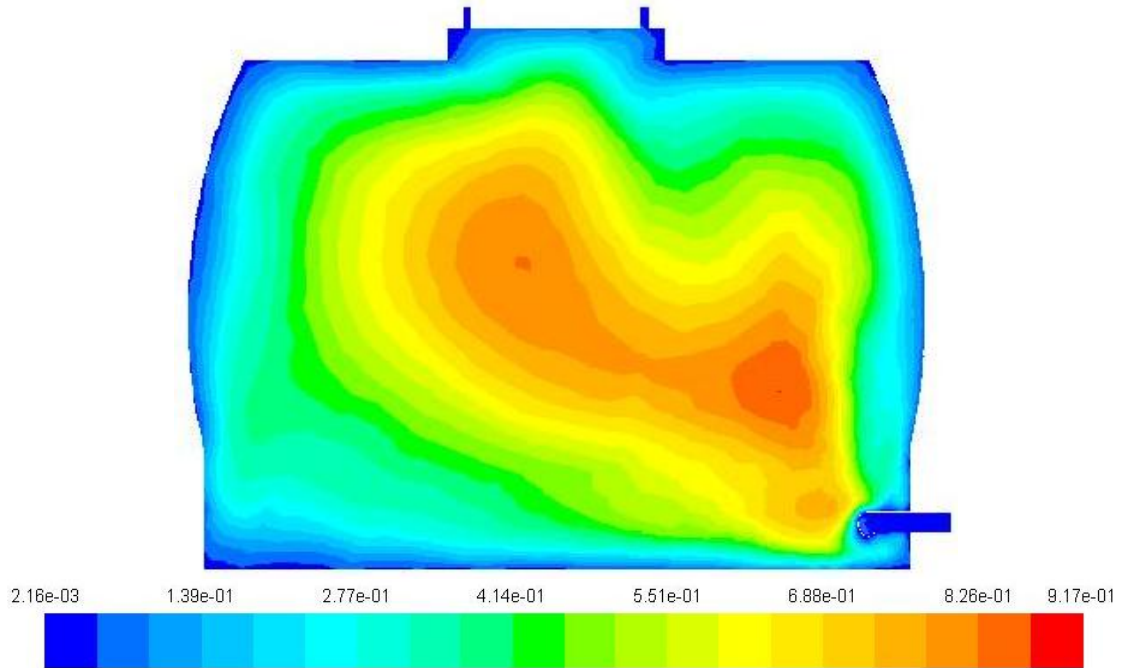


Figure 3.38 Contours of turbulent dynamic viscosity (kg/m-s) for the horizontal open surface tank system operating at $0.000946 \text{ m}^3/\text{s}$ (15 gpm).

The simplification in analyzing this tank in a pressurized system allows for the flow to be deflected by the tanks upper surface inducing some additional turbulent mixing in the system. Yet the scalar transport characteristics over the analyzed flow rates compared closely to the physical tracer study results discussed further in chapter 4.

Figures 3.39 (a)-(i) displays the scalar concentration field as a function of time for the horizontal open surface tank system.

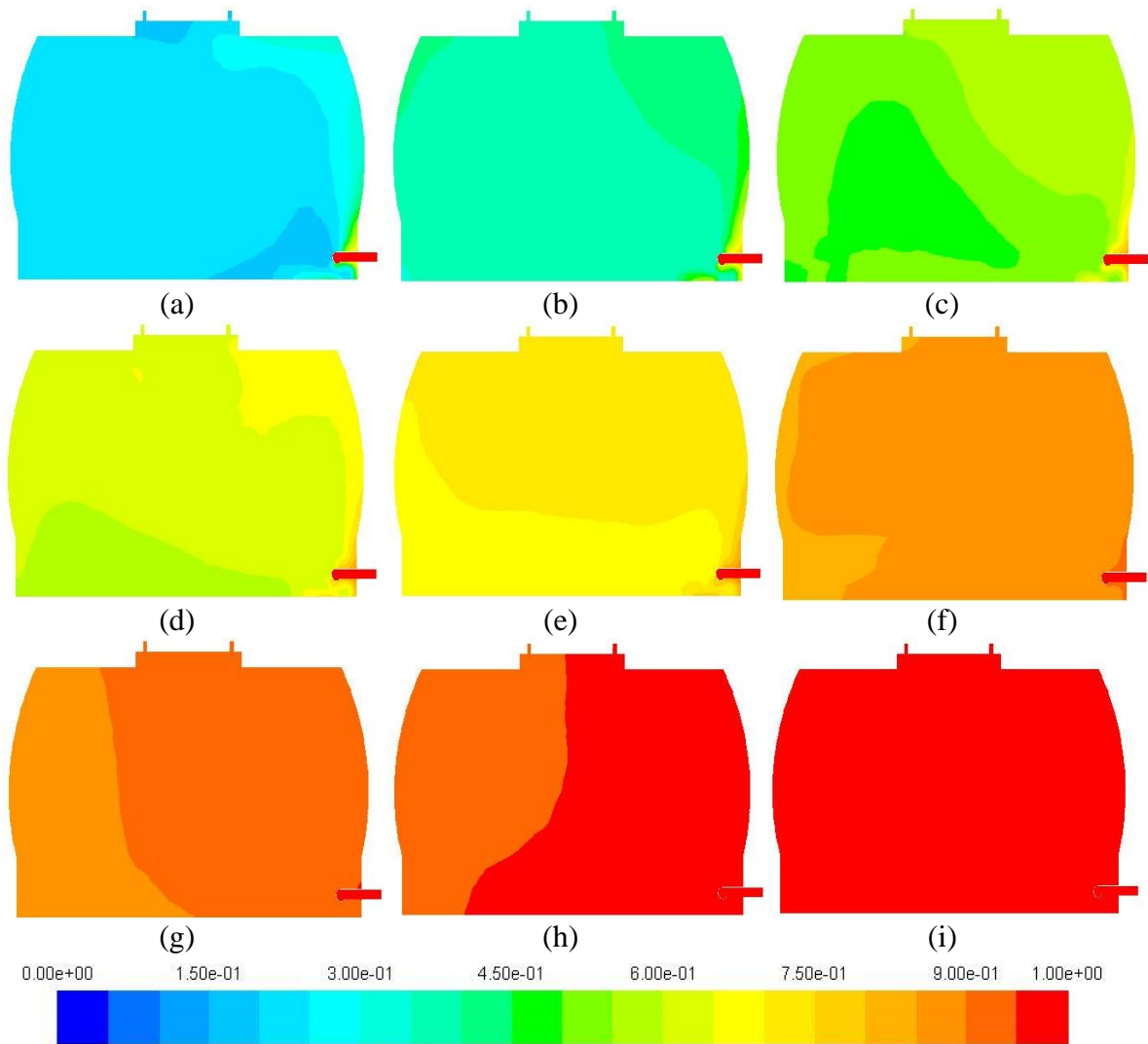


Figure 3.39 Contours of scalar concentration for horizontal open surface tank system operating at $0.000946 \text{ m}^3/\text{s}$ (15 gpm) for (a) $t = 600 \text{ s}$, (b) $t = 1200 \text{ s}$, (c) $t = 1800 \text{ s}$, (d) $t = 2400 \text{ s}$, (e) $t = 3000 \text{ s}$, (f) $t = 4800 \text{ s}$, (g) $t = 6000 \text{ s}$, (h) $t = 8400 \text{ s}$, and (i) $t = 9600 \text{ s}$.

Figures 3.39(a)-(i) fail to show a clear pattern of scalar transport as with the series of pressurized tanks and vertical open surface tank systems. It is clear that the scalar concentration field takes a greater amount of time to interact with the left-hand-side portion of the tank (as pictured above). This effect is largely due to the location of the system outlet in the center portion of the tank (e.g., see Figure 3.24 (b)) and the more chaotic flow field as observed in Figure 3.37.

Figure 3.40 shows the scalar transport field for a time of 1800 s overlain with the velocity vectors.

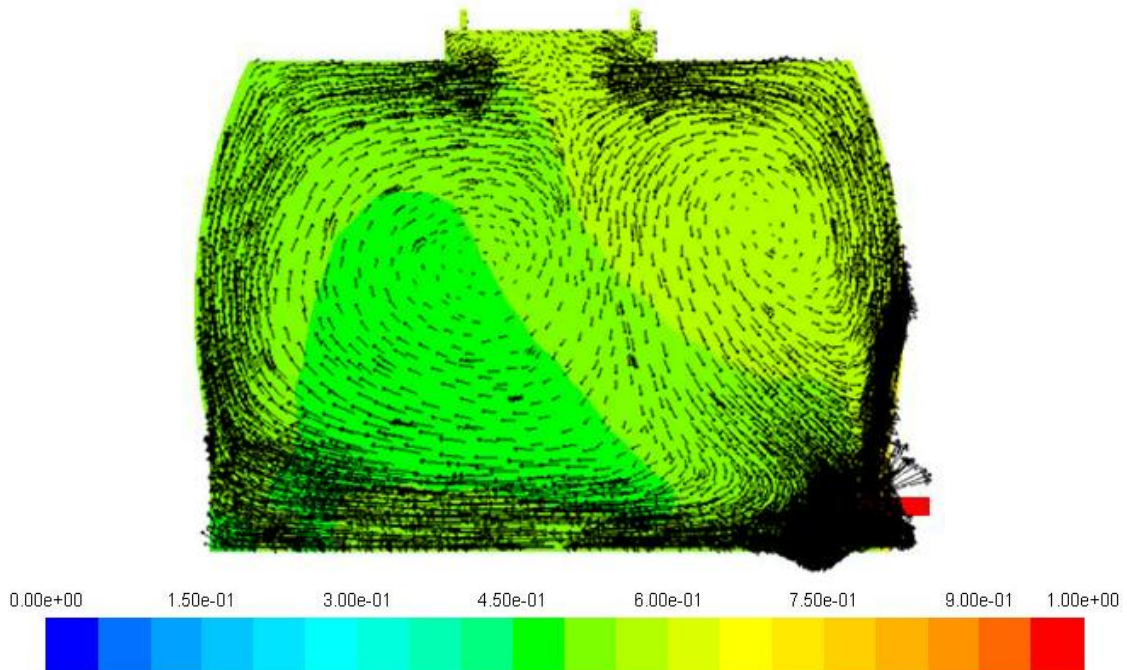


Figure 3.40 Scalar transport field at $t = 1800$ s and velocity vectors for horizontal open surface tank system operating at $0.000946 \text{ m}^3/\text{s}$ (15 gpm).

The regions of lower scalar concentration in the horizontal tank are a result of the flow recirculation in that region and not a direct path. Again, as in the case of the vertical open surface tank, the highly three-dimensional flow field drives the scalar field and cannot be easily observed on any one given plane through the system.

3.2.4 Baffled Tank System

A case study was performed on pilot scale experimental study of a contact tank by Shiono *et al.* (1991) and the further investigation performed by Xu and Venayagamoorthy (2010) and Xu (2010).

3.2.4.1 Baffled Tank System Configuration.

The analyzed system was based on the pilot scale experimental study of a contact tank by Shiono *et al.* (1991) with a length of 1.995 m, a width of 0.94 m, and seven internal baffles each measuring 0.75 m in length. To further investigate the hydraulic efficiency characteristics of the system, Xu and Venayagamoorthy (2010) altered the number of baffles, from zero to ten, on the same footprint as the pilot tank used by Shiono *et al.* (1991) (see Figure 3.41).

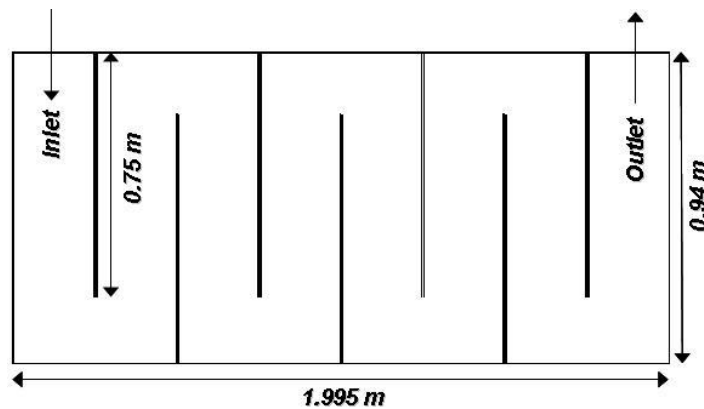


Figure 3.41 Model geometry for pilot scale contact tank study (Shiono *et al.* 1991).

3.2.4.2 Baffled Tank System FLUENT Setup

The computational model for the baffle contact tank had boundary conditions of velocity inlet, pressure outlet, and no-slip wall condition. This model utilized a two-dimensional flow model using RANS model with the standard $k-\varepsilon$ turbulence model. An area-weighted average of the passive scalar concentration was monitored at the system outlet.

3.2.4.3 Baffled Tank System Results and Conclusions

Figures 3.42 (a)-(k) show the contours of velocity magnitude for the internal baffle configurations. As the number of baffles increased in the system, the area of the dead zones decreased.

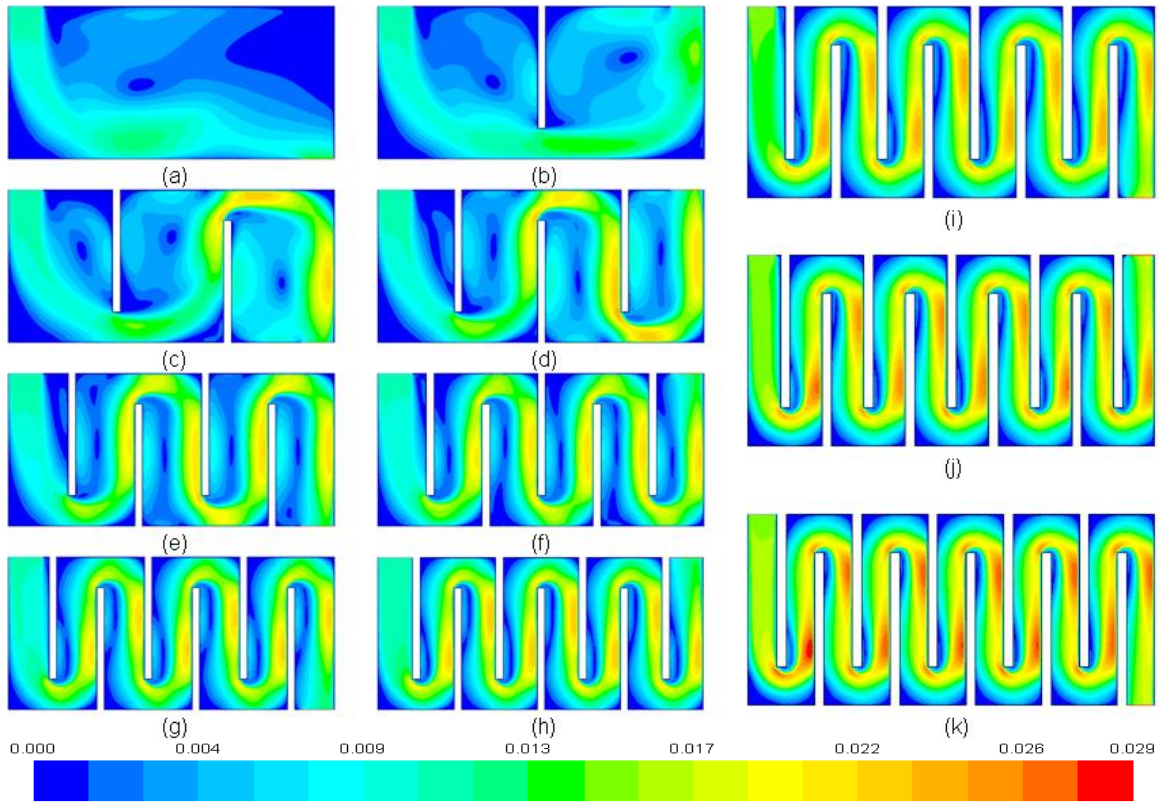


Figure 3.42 Contours of velocity magnitude (m/s) for pilot scale chlorine contact tank with (a) 0, (b) 1, (c) 2, (d) 3, (e) 4, (f) 5, (g) 6, (h) 7, (i) 8, (j) 9, and (k) 10 internal baffles (Xu and Venayagamoorthy 2010).

Figures 3.42 (a)-(k) show the influence of inertia on the time-averaged velocity field. As the flow field approaches the end of each baffle, it cannot make such an abrupt change in direction causing a region of separation and recirculation on the opposing sides of the baffles. There are also obvious dead zones in the rectangular corners of each baffle section as the flow field takes a preferential path through the system.

Figures 3.43 (a)-(l) present the contours of scalar concentration for the seven baffled tank over time (Xu 2010).

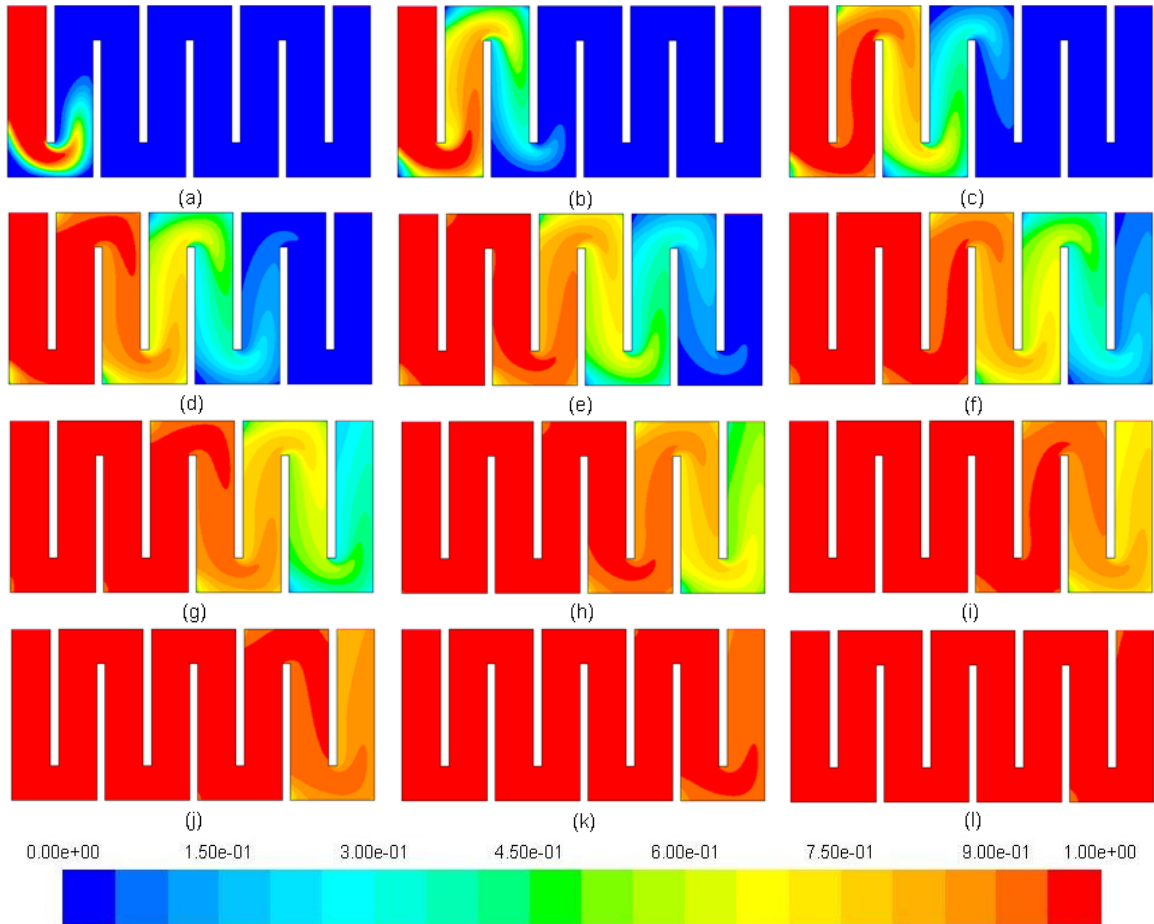


Figure 3.43 Contours of scalar concentration for a seven baffled tank system operating at $0.00012 \text{ m}^3/\text{s}$ (1.9 gpm) at (a) $t = 100$ s, (b) $t = 200$ s, (c) $t = 300$ s, (d) $t = 400$ s, (e) $t = 500$ s, (f) $t = 600$ s, (g) $t = 700$ s, (h) $t = 800$ s, (i) $t = 900$ s, (j) $t = 1000$ s, (k) $t = 1100$ s, and (l) $t = 1200$ s.

In comparing the velocity fields of Figure 3.42 (h) with the scalar distribution in Figures 3.43 (a)-(l), the scalar concentration field is transported faster by advective forces. The dead zones and regions of separation rely on the much slower processes such as diffusion for scalar transport.

3.3 Conclusions

Pipe loop systems have traditionally been considered ideal plug flow reactors because of their large length to width ratio. The pipe loop system in this study is clearly dominated by advective forces as shown in the system velocity fields and scalar transport properties. The regions of separation and recirculation are relatively small in comparison to the entire system. The maximum magnitude of turbulent viscosity (approximately 0.15 kg/m-s) was relatively small in comparison to the maximum turbulent viscosities observed in the other systems in this study again showing the dominance of advective forces over mixing and diffusive forces. The system was analyzed only for turbulent flows (Reynolds numbers of approximately 5800 and 2900) and would likely have a different behavior for purely laminar flow conditions, although such low flows would be well below the requirements for any public water system.

The Water Quality Control Division of CDPHE designated the analyzed pressure tank systems as viable small public water disinfection systems. Chapter 4 will focus on the hydraulic efficiency of these systems but the hydrodynamics already show a significant departure from the plug flow behavior seen in the pipe loop system. While there are no clear dead zones in the tanks as observed in baffled tanks, there are significant areas of recirculation as indicated by the velocity vector and contours of turbulent viscosity. The observed scalar transport through the system does indicate some short circuiting as the concentration front reaches the tank outlet before the concentration reaches a steady-state. The difficulty in visualizing the entirety of the scalar transport about a two-dimensional plane is the three-dimensional nature of the flow through these systems as observed in the velocity vectors in Figures 3.12 and 3.13. A single pressurized

tank would likely not be an adequate disinfection system, but a series of these tanks would yield a sufficient system mimicking the behavior of baffles in a large tank as will be seen in chapter 4.

The open surface tank systems displayed the most highly three-dimensional flow fields amongst all of the systems in this research. This condition was a result of the inlet configurations in the tanks. There were apparent regions of recirculation in the center of each of the tanks designated by lower velocities and higher turbulent viscosities. The three-dimensional pathlines showed a clearer picture of the flow field for each of the respective systems which governed the flow of the passive scalar field through the systems. As these open surface tanks are an ongoing field of study not included in the scope of this research, they will be analyzed using a free surface model to more fully analyze the flow characteristics as influenced by the inlet configuration. The goal of this further research will be to increase the hydraulic efficiency of these large open surface tanks by altering the inlet configuration to more evenly distribute the flow at the inlet resulting in a lower region of the tank to promote uniform mixing and drive to flow towards plug flow conditions.

The case study performed on the work by Xu and Venayagamoorthy (2010) shows the influence that baffles have on the velocity field. As the number of baffles increase in the tank, the area of dead zones present dramatically decreases. Yet there does not appear to be a significant decrease in the dead zone area for systems containing more than 6 baffles. Adding more baffles would allow the flow behavior to asymptotically approach plug flow but not without an associated increase in pressure losses in the system. There seems to be an effective point of diminishing returns as related to

hydraulic efficiency discussed in further detail in chapter 4. The two-dimensional model provided an adequate representation of the baffled contact tank system in terms of both the velocity field and scalar transport.

CHAPTER 4: EVALUATION OF HYDRAULIC EFFICIENCY OF DISINFECTION SYSTEMS BASES ON RESIDENCE TIME DISTRIBUTION CURVES¹

4.1 Introduction

Hydraulic efficiency is an important component in the design and operation of disinfection systems, particularly chlorine contact tanks, considering the potential carcinogenic products formed in the chlorination process. Improving the hydraulic efficiency of a system allows for a smaller dose of disinfectant to be used thus reducing the formation of potential carcinogens (Singer 1994 and Wang *et al.* 2003). Most contact tanks have an uneven flow path, inducing regions of recirculation or stagnation, commonly known as dead zones (Wang & Falconer 1998) shown throughout the CFD model results in chapter 3.

In order to evaluate the efficiency of contact tanks for disinfection purposes, the United States Environmental Protection Agency (USEPA) has established the practice of assigning tanks a baffle factor (*BF*) (USEPA 2003). The contact time of the disinfectant with the water in the tank is taken to be t_{10} , which is the time for 10 percent of the inlet concentration to be observed at the outlet. These quantities are typically obtained through tracer studies of an established system using conductivity measurements or tracer analysis using fluoride or lithium. *BF* is the ratio of t_{10} to *TDT* and ranges from a value of

¹ This chapter has been published in substantial part as "Evaluation of hydraulic efficiency of disinfection systems based on residence time distribution curves" by J.M. Wilson and S.K. Venayagamoorthy, in *Environmental Science and Technology* **2010**, 44 (24): 9377-9382.

0.1 representing an un baffled tank with significant short-circuiting to an upper bound value of 1.0 representing ideal plug flow conditions as described by the Interim Enhanced Surface Water Treatment Rule (USEPA 2003).

In addition, the Morrill Index (*MI*), used as a measure of hydraulic efficiency in Europe, evaluates the amount of diffusion in a system based on the ratio t_{90}/t_{10} (USEPA 1986 and Teixeira & Siqueira 2008). The USEPA's practice of assigning *BFs* assumes that a system can achieve plug flow through the use of *TDTs*. The research presented in this chapter shows that a better measure of hydraulic efficiency must include the complete flow dynamics of the system since it is the flow dynamics that governs the transport of a tracer from the inlet to outlet through time (Stamou & Noutsopoulos 1994). This is usually depicted by a residence time distribution (RTD) or flow through curve (FTC), obtained by plotting the system's effluent concentration over time, as shown for example in Figure 4.1.

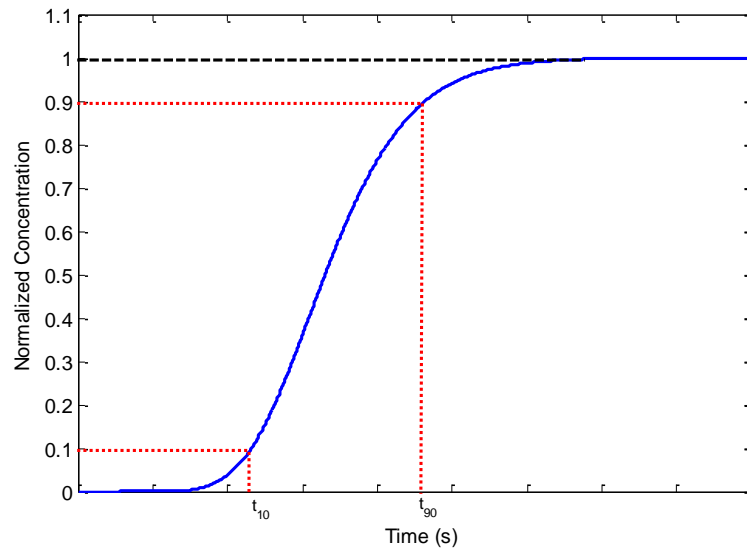


Figure 4.1 Residence time distribution (RTD) curve for an arbitrary disinfection system.

As previously discussed in chapter 2, the shape of the RTD curve provides insight to the nature of the flow in the system (Stamou 2002). However, current practice only uses the rising limb, or rather the t_{10} value, from the RTD curve and compares it to a *TDT* value unrelated to the actual flow in the system. This methodology often leads to a *BF* that overestimates the system's actual hydraulic efficiency, as shown throughout the results in this study. The results evaluating the four disinfection systems are discussed in detail, providing the basis for a better evaluation methodology of hydraulic efficiency based on the ratio of t_{10} to t_{90} obtained from the RTD curves.

4.2 Experimental Methods

To validate the usage of CFD for analysis of these small public water disinfection systems, conservative tracer analysis was performed on each of these systems at a minimum of two flow rates. A detailed standard operating procedure (SOP) was developed for the conservative tracer analysis of these systems and can be found in its entirety in appendix E. Lithium (lithium chloride) was selected as the primary conservative tracer in this study due to the low background levels found in raw water. Fluoride (sodium fluoride) was used as a secondary conservative tracer due to its wide use in industry and the ability for on-site analysis whereas lithium sample must be analyzed using mass spectrometry or inductively coupled plasma-atomic emission spectroscopy (used by Colorado State University's Soils and Water Laboratory for analysis). A stock solution was mixed so that the maximum concentration of lithium and fluoride in the system effluent was 0.04 and 1 mg/L, respectively, as to not exceed the maximum contaminant levels. Lithium is not currently regulated under USEPA

regulations and while fluoride is regulated, the 1 mg/L concentration falls well below the 4 mg/L maximum level. The main concern with fluoride was to keep the concentration under the typical range for potable water in the city of Fort Collins.

For the systems constructed at the hydraulics laboratory at Colorado State University's Engineering Research Center, conductivity tracer studies were also performed using sodium chloride to provide a clear estimate for the sampling protocol for lithium and fluoride tracers. These conductivity studies were not used for validating the CFD models due to the fluctuations in source conductivity beyond the control of the experiment. On occasion, the quantity of sodium chloride added to the stock solution under high flow rates often yielded an over-saturated solution which often precipitated out and caused an uneven inlet concentration. While this situation was not ideal, the results were clear enough to accurately develop a sampling protocol. Appendix F contains a SOP for performing conductivity studies using sodium chloride (or similar salt) and an online conductivity meter.

After mixing the appropriate quantity of stock solution for the tested flow rate, the solution was connected to a dual-control electronic chemical injection pump (LMI P151-392BI) to be fed into the system upstream of a static mixer to aid in the even mixing of the tracer (or chlorine-containing species in an actual system). Samples were taken from the appropriate points in the system at the specified times to be sent to the Soil and Water Laboratory for analysis. For some of the tracer studies, sufficient sample quantities were collected to perform on-site analysis using atomic absorption of a colorimeter (HACH Fluoride Pocket Colorimeter) with SPADNS 2 (Arsenic-free) Fluoride Reagent AccuVac Ampules commonly used in field analysis of water treatment facilities.

4.3 Comparison of scalar transport results for CFD models and physical tracer studies

The following subsections present the results of the physical tracer studies using conservative tracer analysis as compared to the computational model results of the passive scalar transport.

4.3.1 Pipe Loop System

The tracer study analyzed flow rates of 0.000505 and 0.001093 m³/s (8 and 16 gpm), respectively. Table 4.1 presents the results of the pipe loop analysis which show that the *BF* values are consistently higher than the t_{10}/t_{90} values by approximately 10 percent.

Table 4.1 Results of CFD model and tracer study analysis of pilot pipe-loop facility.

Analysis	Q (m³/s)	t_{10} (s)	t_{90} (s)	<i>TDT</i> (s)	<i>BF</i>	t_{10}/t_{90}
CFD Model	0.000505	3234	3774	3360	0.96	0.86
	0.001093	1584	1890	1680	0.94	0.84
Tracer Study	0.000505	3120	3786	3360	0.93	0.82
	0.001093	1536	1950	1680	0.91	0.79

Figures 4.2(a) and (b) show a comparison of RTD curves for the tracer study and CFD model results for two different flow rates. The CFD model and lithium tracer RTD curves correlated closely, as observed in Figures 4.2(a) and (b), thus validating the CFD analysis for three-dimensional scalar transport on the specified pipe-loop configuration.

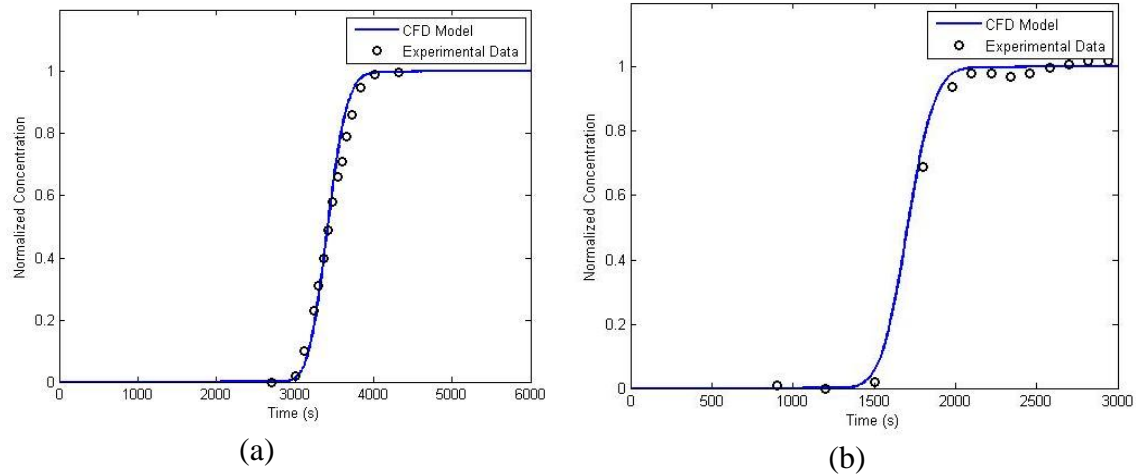


Figure 4.2 Comparison of CFD model and tracer study RTD curves for pipe loop facility for (a) 0.000505 m³/s (8 gpm) and (b) 0.001093 m³/s (16 gpm).

4.3.2 Pressurized Tank System

The tracer study analyzed flow rates of 0.000631, 0.000946, and 0.001262 m³/s (or 10, 15, and 20 gpm) for 1, 2, and 3 tanks in series, respectively. Figures 4.3 (a), (b) and (c) show the comparison of RTD curves for the tracer study and the CFD model results for 1, 2, and 3 tanks in series at a flow rate of 0.000946 m³/s, respectively. The CFD model and lithium tracer RTD curves again correlated closely, as observed in Figures 4.3 (a), (b), and (c), thus validating the CFD analysis for three-dimensional scalar transport on the specified pressurized tank configuration.

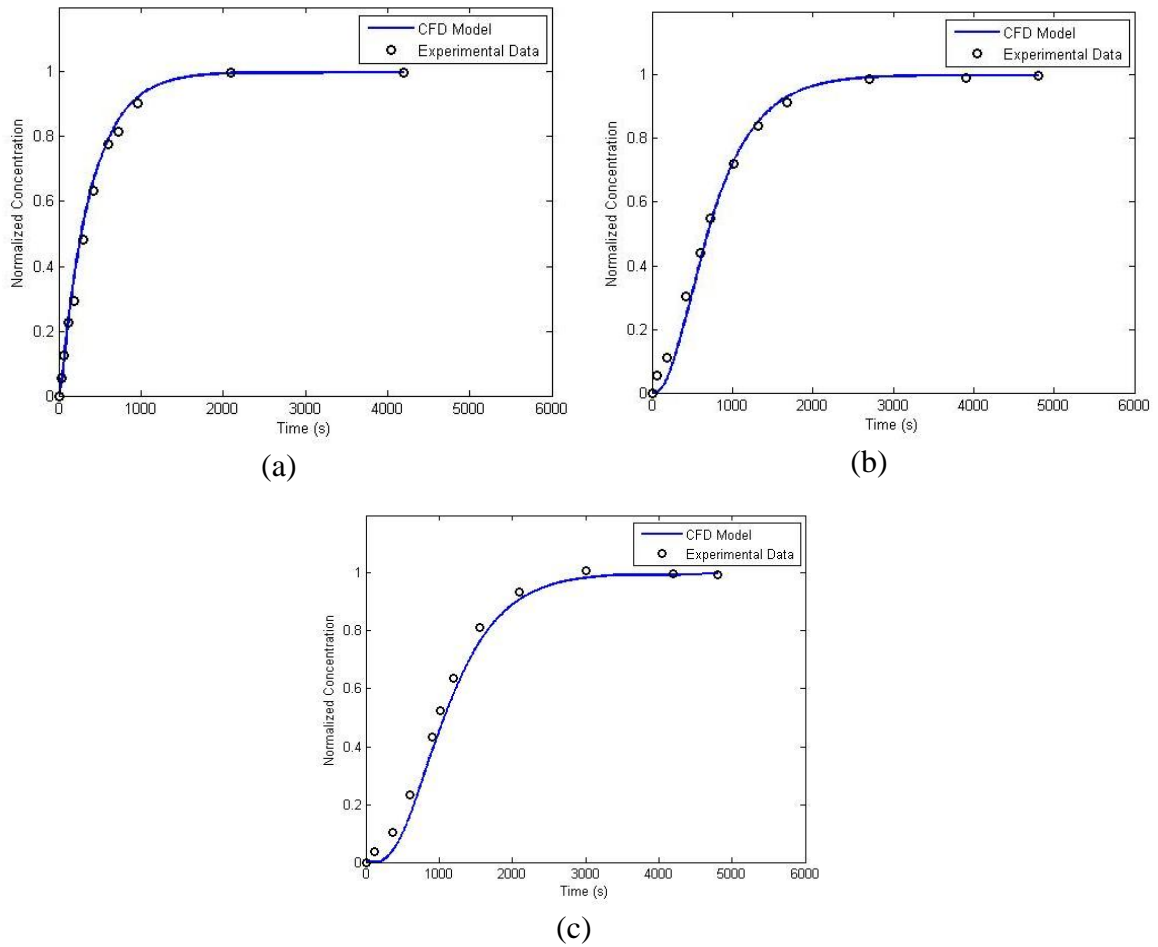
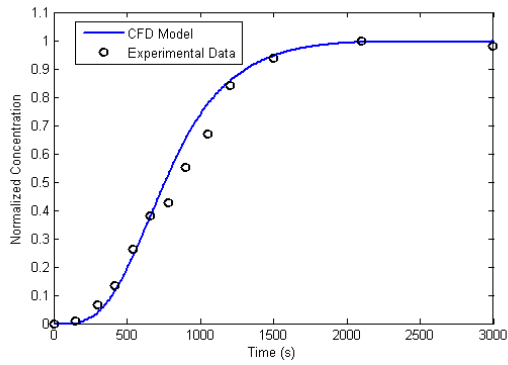
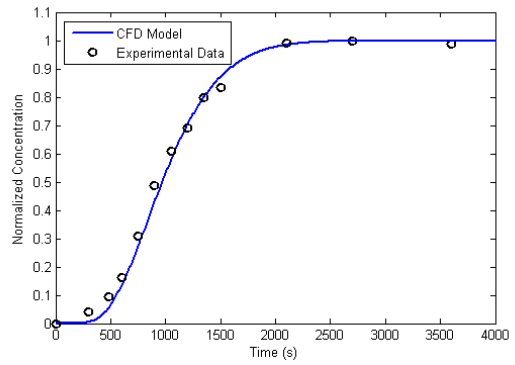


Figure 4.3 Comparison of CFD model and tracer study RTD curves for 0.000946 m³/s (15 gpm) through (a) 1 tank, (b) 2 tanks and (c) 3 tanks in series.

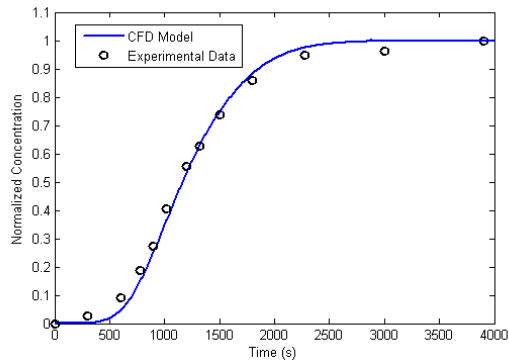
For the 4, 5, and 6 series tank system, flow rates of 0.001893, 0.001262, 0.000946, and 0.000631 m³/s (30, 20, 15, and 10 gpm) were analyzed. Figures 4.4 (a), (b), and (c) present a comparison of the tracer study and CFD model study results for a flow rate of 0.001893 m³/s (30 gpm) for 4, 5, and 6 series tank systems, respectively.



(a)



(b)



(c)

Figure 4.4 Comparison of CFD model and tracer study RTD curves for $0.001893 \text{ m}^3/\text{s}$ (30 gpm) through (a) 4 tanks, (b) 5 tanks and (c) 6 tanks in series.

Table 4.2 contains the data resulting from physical tracer studies and CFD models for all of the series pressure tank systems.

Table 4.2 Results of CFD model and tracer study analysis of series tank system.

Analysis	No. of Tanks in Series, N_T	Q (m^3/s)	t_{10} (s)	t_{90} (s)	TDI (s)	BF	t_{10}/t_{90}
CFD Model	1	0.000316	155	2354	1000	0.16	0.07
	1	0.000631	108	1212	498	0.21	0.09
	1	0.000946	60	870	336	0.19	0.07
	1	0.001262	54	624	252	0.22	0.09
	2	0.000316	730	4271	2000	0.36	0.17
	2	0.000631	354	2106	1002	0.36	0.17
	2	0.000946	252	1506	666	0.38	0.17
	2	0.001262	210	1062	498	0.42	0.20
	3	0.000316	1670	6185	3000	0.56	0.27
	3	0.000631	744	3078	1500	0.50	0.24
	3	0.000946	498	2046	1002	0.50	0.24
	3	0.001262	378	1548	750	0.50	0.24
	4	0.000631	1207	3931	2000	0.60	0.31
	4	0.000946	80	2594	1333	0.60	0.31
	4	0.001262	601	1988	1000	0.60	0.30
	4	0.001893	401	1328	667	0.60	0.30
	5	0.000631	1634	4659	2500	0.65	0.35
	5	0.000946	1101	3106	1667	0.66	0.35
	5	0.001262	846	2378	1250	0.68	0.36
	5	0.001893	566	1582	833	0.68	0.36
6	0.000631	2105	5505	3000	0.70	0.38	
6	0.000946	1396	3665	2000	0.70	0.38	
6	0.001262	1042	2738	1500	0.69	0.38	
6	0.001893	713	1869	1000	0.71	0.38	
Tracer Study	1	0.000316	90	2963	1000	0.09	0.03
	1	0.000631	48	1266	498	0.10	0.04
	1	0.000946	48	948	336	0.14	0.05
	1	0.001262	30	684	252	0.12	0.04
	2	0.000316	446	3487	2000	0.22	0.13
	2	0.000631	300	2496	1002	0.30	0.12
	2	0.000946	162	1608	666	0.24	0.10
	2	0.001262	168	1110	498	0.34	0.15
	3	0.000316	989	6027	3000	0.33	0.16
	3	0.000631	510	3048	1500	0.34	0.17
	3	0.000946	354	1944	1002	0.35	0.18
	3	0.001262	258	1530	750	0.34	0.17
	4	0.000946	546	2430	1333	0.41	0.22
	4*	0.001262	246	1920	1000	0.25	0.13
	4	0.001893	360	1380	667	0.54	0.26
	5	0.000946	774	2808	1667	0.46	0.28
	5*	0.001262	384	2400	1250	0.31	0.16
	5	0.001893	486	1752	833	0.58	0.28
	6	0.000946	1044	3576	2000	0.52	0.29
	6*	0.001262	336	2346	1500	0.22	0.14
6	0.001893	618	2016	1000	0.62	0.30	

*Lithium results were skewed because of a significant residual left in the system from a prior tracer study and are thus unreliable.

Additional figures presenting the comparison of CFD and tracer study results for the pressurized tank systems can be found in appendix G.

Figures 4.5 (a) and (b) show the hydraulic efficiency versus the number of tanks in series over the system for the CFD models and tracer studies, respectively.

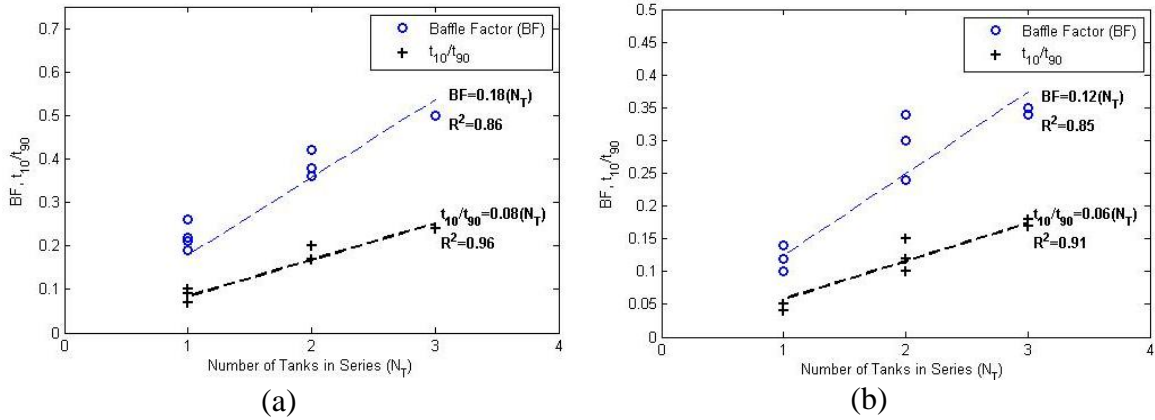


Figure 4.5 Comparison of BF and t_{10}/t_{90} values for (a) CFD model and (b) tracer study for 3 pressurized series tank system.

Figures 4.5 (a) and (b) also show a linear regression curve fit to each series of data points and their corresponding equations and coefficients of determination, R^2 , with a y-intercept of zero. Despite the differences in the BF and t_{10}/t_{90} values of the computational model and tracer study results, the curve fits in Figures 4.5 (a) and (b) show a linear scale-up in the hydraulic efficiency with an increase of the number of tanks in series. Furthermore, Figures 4.5 (a) and (b) show that the BF values overestimate the hydraulic efficiency described by t_{10}/t_{90} by approximately 100 percent for both cases.

Figures 4.6 (a) and (b) display the average values of BF and t_{10}/t_{90} for the CFD model and tracer studies as compared to the linear regression curve fit developed for the 3 series tank system.

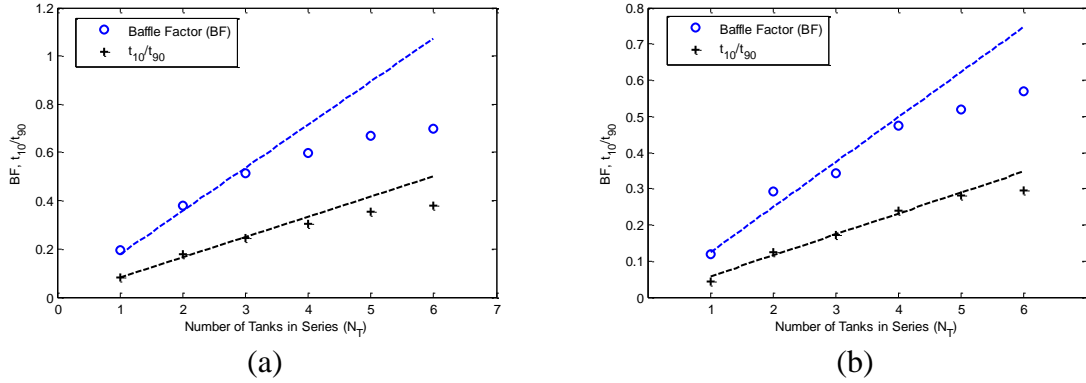
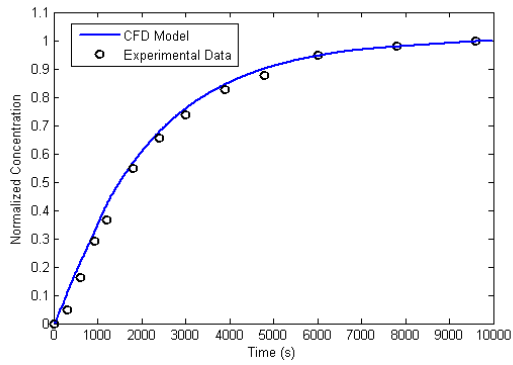


Figure 4.6 Comparison of BF and t_{10}/t_{90} values for (a) CFD model and (b) tracer study for 6 pressurized series tank system.

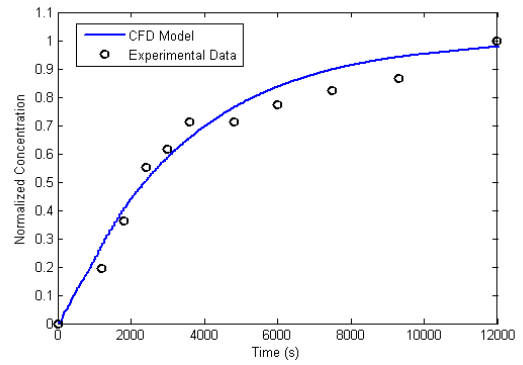
These figures show that a linear increase in hydraulic efficiency breaks down after approximately 4 tanks in series. Additionally, adding another tank into the system after 4 tanks only provides a minimal gain in efficiency but still adds a significant amount of pressure loss to the system as observed in chapter 3. If the pressure head of a source is questionable it is important to maximize system efficiency while reducing pressure losses allowing for adequate flow through the system.

4.3.3 Open Surface Tank Systems

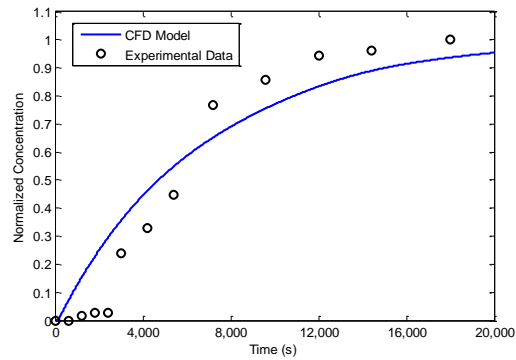
The tracer study analyzed flow rates of 0.000316, 0.000631, and 0.000946 m^3/s (or 5, 10, and 15 gpm) for both the vertical and horizontal open surface tank systems. Figures 4.7 (a), (b) and (c) show the comparison of RTD curves for the tracer study and the CFD model results for the vertical open surface tank over the range of analyzed flow rates. Figures 4.8 (a), (b) and (c) show the comparison of RTD curves for the tracer study and the CFD model results for the horizontal open surface tank over the range of analyzed flow rates.



(a)



(b)



(c)

Figure 4.7 Comparison of CFD model and tracer study RTD curves for vertical open surface tank system operating at (a) 0.000946 (15 gpm), (b) 0.000631 (10 gpm), and (c) 0.000316 m³/s (5 gpm).

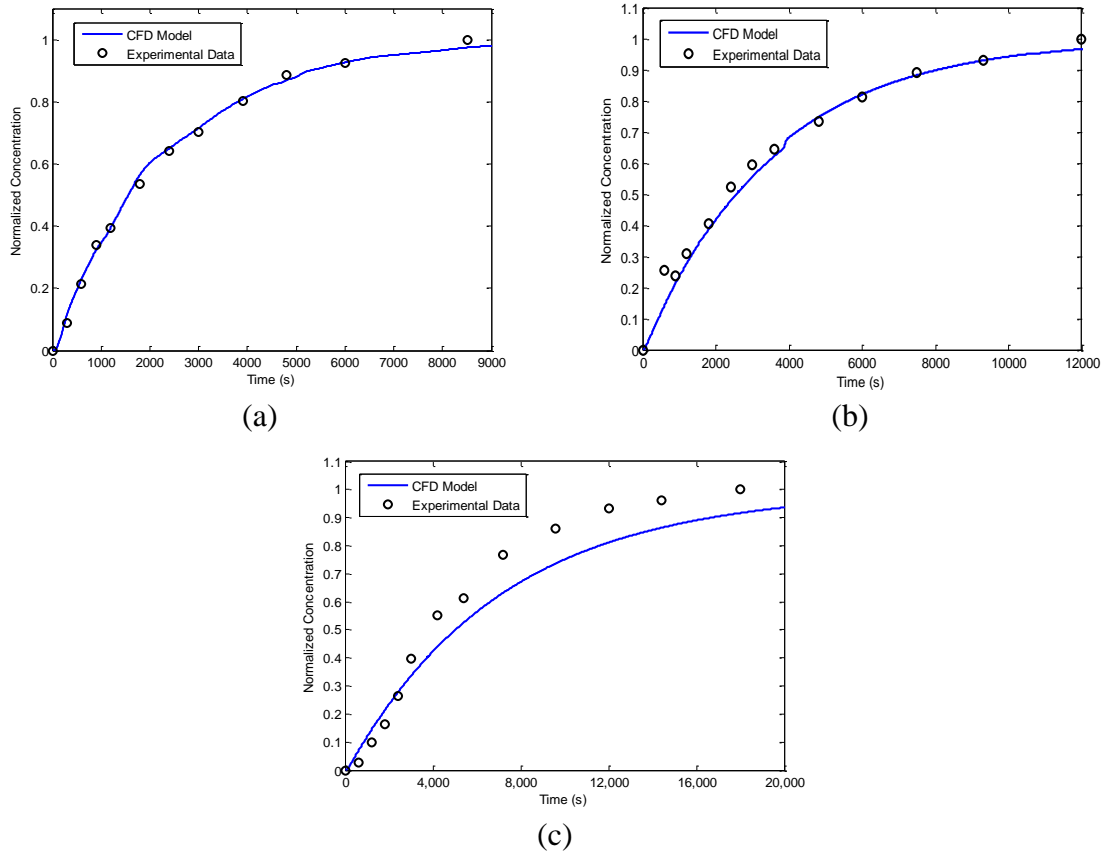


Figure 4.8 Comparison of CFD model and tracer study RTD curves for horizontal open surface tank system operating at (a) 0.000946 (15 gpm), (b) 0.000631 (10 gpm), and (c) 0.000316 m³/s (5 gpm).

The CFD model and lithium tracer RTD curves again correlated well with the 0.000946 and 0.000631 m³/s (15 and 10 gpm) for both the vertical and horizontal open surface tank systems, as observed in Figures 4.7 (a) and (b) and Figures 4.8 (a) and (b). For all 0.000316 m³/s (5 gpm) cases, the CFD model followed the trend of the experimental data but did not match their magnitude. These results show that the pressurized treatment of these open surface tank systems begins to break down around 0.000631 m³/s. In a pressurized model of these systems, the flow is allowed to interact with the top portions of each tank which induces greater recirculation and causes that passive scalar to reside longer in the computational models than in the physical models.

Tables 4.3 and 4.4 show the data analysis of the vertical and horizontal open surface tanks. These results also show that the BF values are consistently higher than the t_{10}/t_{90} values

Table 4.3 Results of CFD model and tracer study analysis of vertical open surface tank system.

Analysis	Q (m^3/s)	t_{10} (s)	t_{90} (s)	TDT (s)	BF	t_{10}/t_{90}
Tracer Study	0.000946	436.8	5168.0	2000	0.22	0.08
	0.000631	616.7	10002.0	3000	0.21	0.06
	0.000316	1260.6	10793.1	6000	0.21	0.12
CFD Model	0.000946	293.9	4793.2	2000	0.15	0.06
	0.000631	446.6	7588.3	3000	0.15	0.06
	0.000316	815.2	15040.0	6000	0.14	0.05

Table 4.4 Results of CFD model and tracer study analysis of horizontal open surface tank system.

Analysis	Q (m^3/s)	t_{10} (s)	t_{90} (s)	TDT (s)	BF	t_{10}/t_{90}
Tracer Study	0.000946	327.9	5253.3	2100	0.16	0.06
	0.000631	380.6	7882.5	3150	0.12	0.05
	0.000316	1193.7	10910.8	6300	0.19	0.11
CFD Model	0.000946	271.3	5267.9	2100	0.13	0.05
	0.000631	428.5	8073.0	3150	0.14	0.05
	0.000316	852.6	16689.2	6300	0.14	0.05

4.3.4 Baffled Tank System

The efficiency of the baffled tank system increases in a manner that appears to never reach plug flow conditions regardless of the number of baffles. The values of BF and t_{10}/t_{90} reflect this observation as shown in Table 4.5. Further details on the hydraulic efficiency of baffled tanks are discussed by Xu and Venayagamoorthy (2010) and Xu (2010).

Figure 4.9 shows the RTD curves of the internal baffle configurations (from zero to ten) of the pilot scale chlorine contact tank shown in part in Figures 3.42 (a)-(l). The

gradient of the RTD curve increases with the number of baffles, indicating that advective transport begins to dominate diffusive transport as the number of baffles increases in the tank.

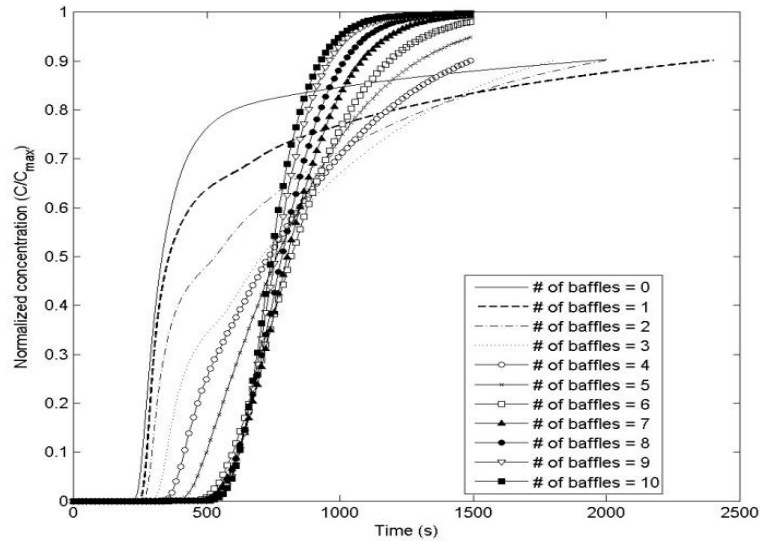


Figure 4.9 Comparison of RTD curves for internal baffle configurations of pilot scale chlorine contact tank.

Table 4.5 presents the results of the two-dimensional CFD analysis of the varying internal baffle configurations of the chlorine contact tank. The results clearly show that the BF is consistently greater than the quantity t_{10}/t_{90} even for the two-dimensional simulation used in this specific configuration.

Table 4.5 Results of CFD analysis for pilot scale contact tank of varying internal baffle configurations.

No. of Baffles	V (m^3)	Q (m^3/s)	TDT (s)	t_{10} (s)	t_{90} (s)	BF	t_{10}/t_{90}
0	1.0052	0.0012	859.11	258	1923	0.30	0.13
1	0.9871	0.0012	843.65	275	2373	0.33	0.12
2	0.9690	0.0012	828.19	294	1980	0.36	0.15
3	0.9509	0.0012	812.73	349	1793	0.43	0.19
4	0.9328	0.0012	797.27	415	1484	0.52	0.28
5	0.9147	0.0012	781.80	498	1295	0.64	0.38
6	0.8966	0.0012	766.34	597	1182	0.78	0.51
7	0.8785	0.0012	750.88	617	1080	0.82	0.57
8	0.8604	0.0012	735.42	617	1015	0.84	0.61
9	0.8424	0.0012	719.96	623	958	0.86	0.65
10	0.8243	0.0012	704.50	623	926	0.88	0.67

4.4 Discussion

While estimates can be made about a systems efficiency based on the BF guidelines (USEPA 1986), a tracer study and resulting RTD curve or combination of a CFD model and validation tracer study are the only ways to evaluate the respective hydraulic efficiencies of the systems. As seen in this study, even the detention time in a pipe loop, listed as a perfect plug flow contactor by the USEPA, departs from a perfect step function. A full RTD curve is a clear indicator of the internal flow dynamics of a system; whether it be a short-circuited flow, plug flow, or somewhere in between (Stamou 2002 and Lyn & Rodi 1990). There are many contributing factors for this departure of the flow such as boundary layer turbulence, flow separation, entry and exit conditions, and buoyancy forces due to stratification. As a result, the t_{10}/t_{90} values for all three systems discussed in this study are consistently lower than the values for the BF . Because the BF formulation assumes that a perfect plug flow can be achieved in every system, it, therefore, inherently overestimates the hydraulic efficiency. For example, systems of the same volume can have differing geometries yet have the same TDT for a

given flow rate. Clearly, large unbaffled rectangular tanks and long pipe contactors have differing flow dynamics and should not have their efficiencies evaluated based on the same idealized *TDT*, which assumes plug flow conditions. This simple illustration presents a major flaw in the USEPA's methodology through failing to make a clear distinction between the hydraulic efficiency and *BF* of a contact tank in the *LTIESWTR Disinfection Profiling and Benchmarking Manual*.

Because a disinfection system with a sufficiently large length-to-width ratio asymptotically approaches ideal plug flow behavior, the *BF* values did not differ as significantly from the t_{10}/t_{90} values in the pipe loop contactor as they did in the pressurized and baffled tank systems. As the length-to-width ratio decreases, the difference in *BF* and t_{10}/t_{90} values increases due to diffusion and other flow phenomena (e.g., flow separation and recirculation). This also results in a further departure from the ideal plug flow assumption inherent in the *BF* formulation of a purely advective system. Furthermore, the results of the CFD models and tracer studies suggest that the ratio of t_{10} to t_{90} is a more appropriate measure of hydraulic efficiency. The values of t_{10} and t_{90} are obtained from the RTD curve which as previously mentioned is a direct indicator of the flow dynamics in the system, thus eliminating any ambiguity associated with the *TDT*. The *MI* evaluates the amount of diffusion in a system based on the ratio t_{90}/t_{10} with a lower bound value of 1.0 representing pure advection (ideal plug flow) but is convoluted in that there is no upper limit to describe the amount of diffusion in the system (Kothandaraman *et al.* 1973). In contrast, the quantity t_{10}/t_{90} gives the ratio of advective to diffusive actions with an upper bound value of 1.0 representing pure advection and a lower bound value of zero representing (at least in theory) pure diffusion. In this manner,

t_{10}/t_{90} presents a straightforward ratio from which one can easily deduce the influence of advective and diffusive forces on the system similar to the Peclet number which is a measure of the advection to diffusion effects in a fluid transport system and is given by

$$Pe = \frac{UL}{\kappa} \quad (4.2)$$

where U is a characteristic velocity scale of the flow, L is a characteristic length scale, and κ is molecular diffusivity. A high Peclet number would imply a system which is dominated by advection and vice versa for a system dominated by diffusion. Hence, the ratio of t_{10}/t_{90} can in fact be considered as a form of the Peclet number expressed here as a time scale ratio.

As with any disinfection system, a more efficient system requires less contact time for a given amount of chlorine-containing species to achieve a certain level of log-inactivation. While the USEPA guidelines have proven adequate for use in contact tank systems, this study has shown that *BFs* only provide a partial assessment of the hydraulic efficiency, making use of only the rising limb of the RTD curve, and thus tend to overestimate the hydraulic efficiency of the disinfection system. On the other hand, the t_{10}/t_{90} ratio provides a better measure of the hydraulic efficiency of any disinfection system since it takes into account the actual flow and scalar transport dynamics in a given system by utilizing a substantial portion of the RTD curve of a given system.

CHAPTER 5: SUMMARY AND CONCLUSIONS

5.1 Summary of Research

The research performed in this study validated the use of CFD analysis, specifically the use of a finite volume code invoking a time-stepping RANS formulation with a standard $k-\varepsilon$ turbulence model, for analysis of passive scalar transport through small public water disinfection systems. Systems included a pipe loop system, series of pressurized tanks, and vertical and horizontal open surface tank systems. A case study was also performed on a baffled contact tank first analyzed by Shiono *et al.* (1991) and further studied by Xu and Venayagamoorthy (2010) to evaluate the indices of hydraulic efficiency.

Chapter 3 provided the hydrodynamic analysis of the prescribed systems as well as detailed descriptions of the unique flow characteristics influencing the nature of scalar transport for each of the systems. Chapter 4 follows up on chapter 3 by interpreting the data obtained from the scalar transport through use of RTD curves. Chapter 4 also challenges the common misconception that the USEPA's *BF* classification system is synonymous with hydraulic efficiency and suggested that the ratio t_{10}/t_{90} might be a better measure of hydraulic efficiency as compared to those found in literature.

5.2 Major Conclusions

The pipe loop system was dominated by advective force yet did not exhibit the predicted ideal plug flow behavior. This result leads to the conclusion that plug flow is an idealized flow characteristic which can only be asymptotically approached. The pipe loop system is an ideal disinfection system that will require a significant footprint area to obtain an adequate capacity.

The series of pressurized tank systems exhibited significant turbulent mixing in the interior region of each tank but were similar to baffles in a rectangular tank in that the more tanks added in series, the greater degree of efficiency the system obtained. A system of 4 tanks in series yielded the maximum return in hydraulic efficiency whereas 6 baffles yielded the maximum return in hydraulic efficiency for the baffled tank system.

The open surface tanks were the least efficient systems with significant short-circuiting and regions of recirculation. The inlet configuration in each of these two tanks greatly influenced the flow dynamics and subsequent scalar transport. By more evenly distributing the inflow, the hydraulic efficiency is likely to increase, which is the subject of future research.

In evaluating hydraulic efficiency, it was concluded that the ratio t_{10}/t_{90} was the best indicator of advective and diffusive forces. While it is clear that this measure of hydraulic efficiency will not replace the baffle factor classification system used by the USEPA for contact tank design based on the billions of dollars of infrastructure built under this assumption, it should be used in combination to provide a better evaluation of these small systems. Small public water systems often lack the resources to provide

adequate monitoring of the free chlorine residual in the system. In such systems, t_{10}/t_{90} is more appropriate in the design calculations.

5.3 Recommendations

The following recommendations are made for the continuing research on the small public water disinfection systems

- Plumb the series tank systems such that the inlet and outlets of each tank vary based on the shortest distance from the outlet of the previous tank to the inlet of the next tank. It is hypothesized that this alteration will reduce the pressure losses in the system to some degree thus allowing the system to operate at a higher capacity.
- Analyze the open surface tank system using an open surface CFD model. While the pressurized model assumption gave an adequate representation of the systems operating at higher flow rates, it failed to capture the true flow dynamics and scalar transport properties at the lowest flow rate.
- Alter the inlet configurations of the open surface tank system and analyze the effect on the systems hydraulic efficiency. It is hypothesized that distributing the influent in a more even fashion will increase the system efficiency. After validating an open surface CFD model, concepts will be modeled to evaluate their performance before constructing and analyzing its behavior in the physical system. This research has the potential to produce further pre-engineered systems to improve the hydraulic efficiency of these commonly used open surface tank systems.

REFERENCES

- Anderson, J.D. *Computational Fluid Dynamics*; McGraw Hill; New York, **1995**.
- Borchardt, J. A.; Walton, G. "Water Quality." In *Water Quality and Treatment*, 3rd ed., American Water Works Association, McGraw-Hill: New York, **1971**.
- Falconer, R.A.; Tebbutt, T.H.Y. A theoretical and hydraulic model study of a chlorine contact tank, *ICE Proceedings*, 1986. 81 (2): 255-276.
- Falconer, R.A.; Liu, S. Modeling solute transport using QUICK scheme, *J. Environ. Eng.* **1988**, 114 (1): 3-20.
- Falconer, R.A.; Ismail, A.I.B.M. Numerical modeling of tracer transport in a contact tank, *Environmental International*. **1997**, 23 (6): 763-773.
- Fluent Inc. *FLUENT 6.3 User's Guide*. **2006**. Ann Arbor, MI.
- Gordon, G.; Adam, L. C.; Bubnis, B. P.; Hoyt, B.; Gillette, S. J.; Wilczak, A. Controlling the formation of chlorate ion in liquid hypochlorite feedstocks, *J. AWWA*. **1993**, 85 (9): 89-97.
- Gordon, G.; Adam, L.C.; Bubnis, B. P. Minimizing chlorate ion formation, *J. AWWA*. **1995**, 87 (6): 97-106.
- Hansen, R. D. Water and wastewater systems in imperial Rome, <<http://www.waterhistory.org>>
- Hart, F. L.; Allen, R.; Dialesio, J.; Dzialo, J. Modifications improve chlorine contact chamber performance. Part II, *Water & Sewage Works*. **1975**, 122 (10): 88-90.
- Hart, F. L. Improved hydraulic performance of chlorine contact chamber, *J. Water Pollut. Control Fed.* **1979**, 51 (12): 2868-2875.
- HDR Engineering, Inc. Safe Drinking Water Act Update: Looking Back - A Century of Change, March **1999**.
- Jones, W.P.; Launder, B.E. The prediction of laminarization with a two-equation model of turbulence, *Int. J. Heat Mass Transfer*, **1972**, 15: 301-314.
- Khan, A.R.; Wicklein, E.A.; Teixeira, E.C. Validation of a three-dimensional computational fluid dynamics model of a contact tank, *J. Hydraul. Eng.* **2006**. **132** (7): 741-746
- Kothandaraman, V.; Southerlan, H.L.; Evans, R.L. Performance characteristics of chlorine contact tanks, *Journal (Water Pollution Control Federation)*. **1973**, 45 (4): 611-619.
- Letterman, R. D, ed. *Water Quality and Treatment*, 5th ed., American Water Works Association, McGraw-Hill: New York, **1999**.
- Levenspiel, O; Smith, W. K. Notes on the diffusion-type model for the longitudinal mixing of fluids in flow, *Chem. Eng. Sci.* **1957**, 6: 227-233.
- Levenspiel, O. *Chemical reaction engineering*, 2nd Ed., Wiley: New York, **1972**.
- Lyn, D.A.; Rodi, W. Turbulent measurements in model settling tank, *J. Hydraulic Eng.* **1990**, 116 (1): 3-21.

- Marske, D. M.; Boyle, J. D. Chlorine contact tank design—A field evaluation, *Water & Sewage Works*, **1973**, 120 (1): 71–77.
- McDermott, J. H. Federal drinking water standards—past, present, and future, *J. Envir. Eng. Div.*, EE4(99), August **1973**: 469.
- Ortloff, C. R. The water supply and distribution system of the Nabataean city of Petra (Jordan), 300 BC - AD 300, *Cambridge Archaeological J.* **2005**, 15(1): 93-109.
- Pope, S.B. *Turbulent Flows*; Cambridge University Press: Cambridge, U.K., **2000**.
- Rauen, W.B.; Lin, B.; Falconer, R.A. CFD and experimental model studies for water disinfection tanks with low Reynolds number flows, *Chem. Eng. J.*, **2007**. 137: 550-560.
- Rebhun, M., and Argaman, Y. Evaluation of hydraulic efficiency of sedimentation basins, *J. Sanit. Eng. Div.* **1965**, 91 (5): 37–45.
- Sawyer, C. M., and King, P. H. The hydraulic performance of chlorine contact tanks, *Proc., 24th Industrial Waste Conf.* **1969**, Purdue Univ., West Lafayette, 1151–1168.
- Shiono, K.; Teixeira, E.C. Turbulent characteristics in a baffled contact tank, *J. Hydraulic Res.* **2000**, 38 (4): 271-271.
- Singer, P.C. Control of disinfection by-products in drinking water, *J. Environ. Eng.* **1994**, 120 (4): 727-744.
- Stamou A. I.; Adams, E. A.; Rodi, W. Numerical modelling of flow and settling in primary rectangular clarifiers, *J. Hydr. Res., IAHR*, **1989**. 27(5): 665-682.
- Stamou A. I. On the prediction of flow and mixing in settling tanks using a curvature modified k- ϵ model, *Applied Mathematical Modelling*, **1991**. 15: 351-358.
- Shiono, K.E.; Teixeira, E.C.; Falconer, R.A. *Turbulent measurements in chlorine contact tank*, The 1st international conference on water pollution: Modeling, measuring, and predicting, Southampton, UK: **1991**, 519-531.
- Stamou, A.I.; Noutsopoulos, G. Evaluating the Effect of Inlet Arrangement in Settling Tanks Using the Hydraulic Efficiency Diagram, *Water SA*. **1994**, 20 (1), 77-83.
- Stamou, A.I. Verification and application of a mathematical model for the assessment of the effect of guiding walls on hydraulic efficiency of chlorination tanks, *J. Hydroinformatics*. **2002**, 4: 245-254.
- Stamou, A.I. Improving the hydraulic efficiency of water process tanks using CFD models, *Chem. Eng. Process.* **2008**, 47: 1179-1189.
- Stamou, A.I.; Theodoridis, G.; Xanthopoulos, K. Design of secondary settling tanks using a CFD model, *J. Environ. Eng.*, **2009**, 135 (7): 551-561.
- Teefy, S.M., ed. *Tracer Studies in Water Treatment Facilities: A Protocol and Case Studies*, American Water Works Association Research Foundation: Denver, **1996**.
- Teixeira, E. C. Hydrodynamic processes and hydraulic efficiency of chlorine contact units, Ph.D. thesis, Dept. of Civil Engineering, Univ. of Bradford, Bradford, U.K., **1993**.
- Teixeira, E.; Siqueira, R. Performance Assessment of Hydraulic Efficiency Indexes, *J. Environ. Eng.* **2008**, 134 (10), 851-859.
- Templeton, M.R.; Hofmann, R.; Andrews, R.C. Case study comparisons of computational fluid dynamics (CFD) modeling versus tracer testing for

- determining clearwell residence times in drinking water treatment, *J. Environ. Eng.*, **2006**, 5 (6): 529-536.
- Thirumurthi, D. A break-through in the tracer studies of sedimentation tanks, *J. Water Pollut. Control Fed.* **1969**, 41 (11): R405–R418.
- Trussell, R. R.; Chao, J.L. Rational design of chlorine contact facilities, *J. Water Pol. Control Fed.* **1977**, 49 (7): 659–667.
- United States Environmental Protection Agency, USEPA. Design manual: municipal wastewater disinfection. **1986**. EPA:625:1-86:021. USEPA Office of Res. and Dev., Cincinnati, OH.
- United States Environmental Protect Agency, USEPA. Report of the National Drinking Water Advisory Council Small Systems Implementation Working Group. **2000**, EPA 816-R-00-012, Office of Water, Washington, D.C.
- United States Environmental Protect Agency, USEPA. Disinfection profiling and benchmarking guidance manual. **2003**, EPA 815-R-99-013, Office of Water, Washington, D.C.
- United States Environmental Protect Agency, USEPA. The Ground Water Rule (GWR) Implementation Guidance. **2009**, EPA 816-R-09-004, Office of Water, Washington, D.C.
- United States Environmental Protection Agency, USEPA. Small Systems and Capacity Development;
<http://water.epa.gov/type/drink/pws/smallsystems/basicinformation.cfm#challenges>, **2010**.
- Venayagamoorthy, S.K.; Stretch, D.D. On the turbulent Prandtl number in homogeneous stably stratified turbulence, *J. Fluid Mech.* **2010**, 644: 359-369.
- Wang, H.; Falconer, R.A. Simulating disinfection processes in chlorine contact tanks using various turbulence models and high-order accurate difference schemes, *Water Res.* **1998**, 32 (5): 1529-1543
- Wang, H.; Shao, X.; Falconer, R.A. Flow and transport simulation models for prediction of chlorine contact flow-through curves, *Water Res.* **2003**, 75 (5): 455-471.
- Wilcox, D.C. *Basic Fluid Mechanics*, 3rd ed.; DCW Industries, Inc: San Diego, **2007**.
- Wilson, J.M.; Venayagamoorthy, S.K. Evaluation of hydraulic efficiency of disinfection systems based on residence time distribution curves, *Environ. Sci. Technol.*, **2010**, 44 (24): 9377-9382.
- Wolfe, R.; Ward, N.; Olson, B. Inorganic chloramines as drinking water disinfectants: a review, *J. AWWA.* **1984**, 76 (5): 74.
- Xu, Q.; Venayagamoorthy, S.K. *Hydraulic efficiency of baffled disinfection contact tanks*, 6th International Symposium on Environmental Hydraulics, 23-25 June 2010, Athens: **2010**, 1041-1046.
- Xu, Q. Internal hydraulics of baffled disinfection contact tanks using computational fluid dynamics, Masters thesis, Dept. of Civil and Environmental Engineering, Colorado State University, U.S. **2010**.

APPENDIX A

Derivation of Reynolds-Averaged Navier-Stokes equations

This procedure begins with the time dependent solution to the Navier-Stokes equations with the Boussinesq approximation.

$$\frac{\partial u_i}{\partial t} + \frac{\partial}{\partial x_j} (u_i u_j) = -\frac{1}{\rho_o} \frac{\partial p}{\partial x_j} + \nu \frac{\partial^2 u_i}{\partial x_j x_j} - \frac{g}{\rho_o} \rho \delta_{iz}, \quad (\text{A.1})$$

where u_i is the turbulent velocity field, ρ_o is the reference density to a reference temperature of the fluid T_o , P is the pressure, ρ is the mass density of the fluid, ν is the kinematic viscosity of the fluid, g is gravitational force, and δ_{iz} is the Kronecker delta function. The time-averaging process assumes that the time-dependent quantities, primarily velocity and pressure, can be decomposed into a time-independent average term and a time-dependent fluctuating term.

$$u_i(t) = \bar{u}_i + u'_i, \quad (\text{A.2})$$

$$p(t) = \bar{p} + p', \quad (\text{A.3})$$

where $u_i(t)$ is the time-dependent turbulent velocity field, \bar{u}_i is the time-averaged velocity field, u'_i is the time-dependent turbulent velocity field fluctuations, $p(t)$ is the time-dependent pressure field, \bar{p} is the time-averaged pressure field, and p' is the time-dependent pressure field fluctuations.

Rearranging equations A.2 and A.3 and substituting into equation A.1 yields

$$\begin{aligned} \frac{\partial(\bar{u}_i + u'_i)}{\partial t} + (\bar{u}_j + u'_j) \frac{\partial(\bar{u}_i + u'_i)}{\partial x_j} \\ = -\frac{1}{\rho_o} \frac{\partial(\bar{p} + p')}{\partial x_j} + \nu \frac{\partial^2(\bar{u}_i + u'_i)}{\partial x_j x_j} - \frac{g}{\rho_o} \rho \delta_{iz}, \end{aligned} \quad (\text{A.4})$$

where \bar{u}_i is the time-averaged velocity field, u'_i is the time-dependent turbulent velocity field fluctuations, ρ_o is the reference density to a reference temperature of the fluid T_o , ρ

is the mass density of the fluid, \bar{p} is the average pressure, ν is the kinematic viscosity of the fluid, p' is the time-dependent pressure field fluctuations and δ_{iz} is the Kronecker delta function.

Time-averaging equation A.4 gives

$$\begin{aligned} \frac{\partial(\overline{u_i + u'_i})}{\partial t} + (\overline{u_j} + u'_j) \frac{\partial(\overline{u_i + u'_i})}{\partial x_j} \\ = -\frac{1}{\rho_o} \frac{\partial(\overline{p} + p')}{\partial x_j} + \nu \frac{\partial^2(\overline{u_i + u'_i})}{\partial x_j \partial x_j} - \frac{g}{\rho_o} \rho \delta_{iz}, \end{aligned} \quad (\text{A.5})$$

where $\overline{u_i}$ is the time-averaged velocity field, u'_i is the time-dependent turbulent velocity field fluctuations, ρ_o is the reference density to a reference temperature of the fluid T_o , ρ is the mass density of the fluid, \bar{p} is the average pressure, ν is the kinematic viscosity of the fluid, p' is the time-dependent pressure field fluctuations and δ_{iz} is the Kronecker delta function.

Equation A.6 presents the results of the time-averaging procedure from A.5

$$\frac{\partial \overline{u_i}}{\partial t} + \overline{u_j} \frac{\partial \overline{u_i}}{\partial x_j} + \frac{\partial \overline{u'_i u'_j}}{\partial x_j} = -\frac{1}{\rho_o} \frac{\partial \bar{p}}{\partial x_j} + \nu \frac{\partial^2 \overline{u_i}}{\partial x_j \partial x_j} - \frac{g}{\rho_o} \rho \delta_{iz} \quad (\text{A.6})$$

Rearranging equation A.6 gives a common form of the Reynolds-Averaged Navier-Stokes equations.

$$\frac{\partial \overline{u_i}}{\partial t} + \overline{u_j} \frac{\partial \overline{u_i}}{\partial x_j} = -\frac{1}{\rho_o} \frac{\partial \bar{p}}{\partial x_i} + \frac{\partial}{\partial x_j} \left(\nu \frac{\partial \overline{u_i}}{\partial x_j} - \overline{u'_i u'_j} \right) - \frac{g}{\rho_o} \rho \delta_{iz}, \quad (\text{A.7})$$

where $\overline{u_{i,j}}$ is the time-averaged velocity field, ρ_o is the reference density to a reference temperature of the fluid T_o , ρ is the mass density of the fluid, \bar{p} is the average pressure, ν

is the kinematic viscosity of the fluid, $\overline{u'_i u'_j}$ is the Reynolds stresses, and δ_{iz} is the Kronecker delta function

APPENDIX B

Numerical schemes utilized in ANSYS FLUENT

Pressure-Based Segregated Solver

The pressure-based segregated solver was used in the FLUENT solutions and is described by the following flow chart.

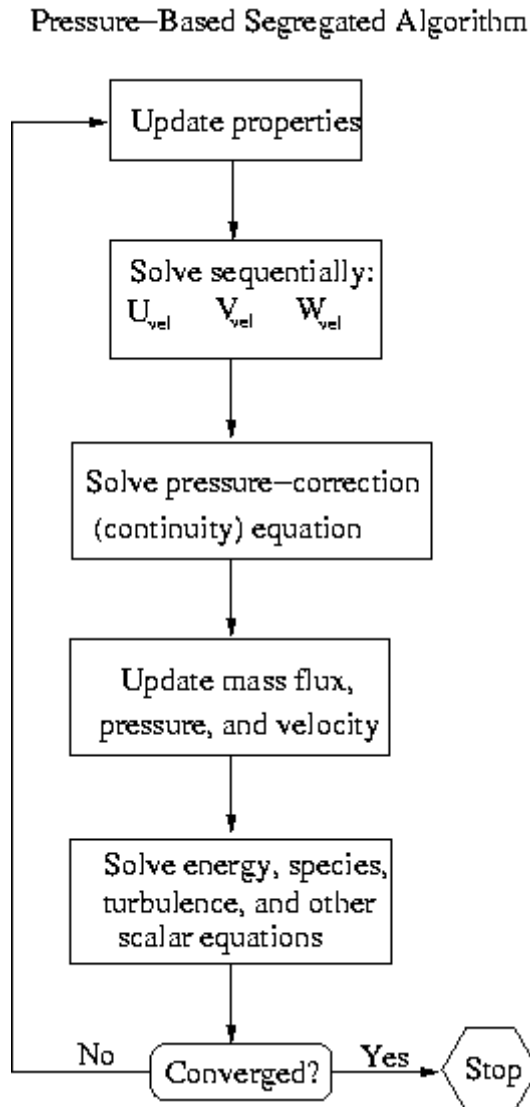


Figure B.1 Flow chart for pressure-based segregated algorithm (Fluent 2006).

In this algorithm, the governing equations are solved sequentially. The non-linear and coupled nature of the governing equations requires that the solution be iterated to reach a converged numerical solution. This solution method requires a greater solution time as

compared to the pressure-based coupled algorithm, but uses 1.5-2 times less memory for solutions (Fluent 2006).

SIMPLE Pressure-Velocity Coupling Solution Algorithm

SIMPLE is one of the methods employed by FLUENT to resolve the pressure-velocity coupling with the Navier-Stokes equations. The simplified steps in this algorithm are:

1. An approximate solution to the velocity field is obtained solving the momentum equation.
2. The pressure gradient is calculate from the pressure distribution at the previous itereation
3. The pressure equation is formulated and solved to obtain the new pressure distribution
4. Velocities are corrected leading to the determination of a new set of conservative fluxes

Second-Order Upwind Spatial Discretization

In order to obtain second-order accuracy of the spatially discretized terms (momentum, turbulent kinetic energy, and turbulent kinetic energy dissipation rate), a second-order upwind scheme is used.

$$\phi_{f,sou} = \phi + \nabla\phi \cdot \vec{r}, \quad (\text{B.1})$$

where ϕ is the cell-centered value, $\nabla\phi$ is the gradient in the upstream cell, and \vec{r} is the displacement vector from the upstream cell centriod and face centriod. For purposes of this demonstration, ϕ is a scalar quantity representative of any pertinent quantity such as

velocity or concentration. This equation requires the determination of the gradient $\nabla\phi$ in each cell as determined by the least squares cell-based gradient evaluation. This gradient evaluation assumes that the solution varies linearly. Figure B.2 displays the cell centroid evaluation expressed in equation B.2 for a change in cell values between cell c_0 and c_i along the vector Δr_i .

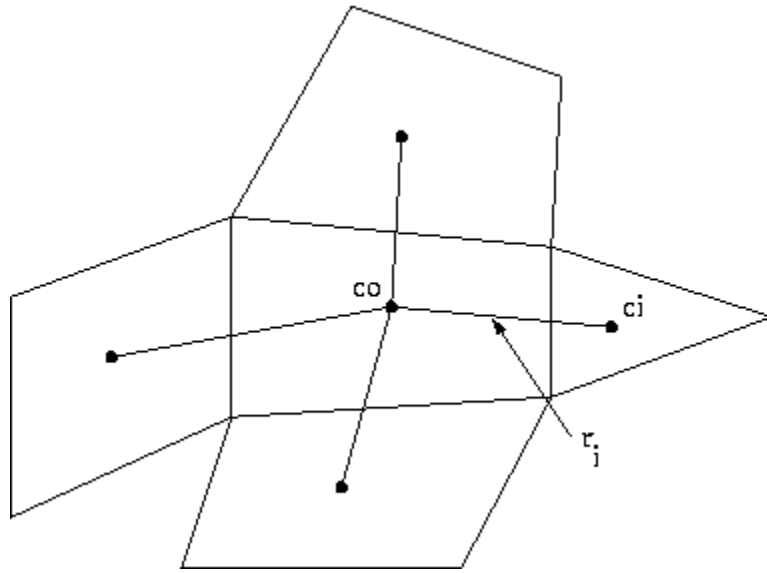


Figure B.2 Cell Centroid Evaluation (Fluent 2006).

$$(\nabla\phi)_{c_0} \cdot r_i = (\phi_{c_i} - \phi_{c_0}), \quad (\text{B.2})$$

where $(\nabla\phi)_{c_0}$ is the cell gradient of current cell, r_i is the displacement vector from the upstream cell centroid and face centroid, ϕ_{c_i} is the cell-centered value of the adjacent cell, and ϕ_{c_0} is the cell-centered value of the current cell. The total expression for all of the cells surround c_0 can be expressed in compact notation by

$$[J](\nabla\phi)_{c_0} = \Delta\phi, \quad (\text{B.3})$$

where $[J]$ is the coefficient matrix as a function of geometry, $(\nabla\phi)_{c_0}$ is the cell gradient of current cell, and $\Delta\phi$ is the difference vector. The method of least squares is an

approach used to determine an approximate solution to an over-determined system. FLUENT uses a weighted least squares approach to determine the solution of the cell gradient

$$\nabla\phi_0 = \phi_x\vec{i} + \phi_y\vec{j} + \phi_z\vec{k} \quad (\text{B.4})$$

The decomposition of the over-determined coefficient matrix using the Gram-Schmidt process yields a matrix of weights for each cell. For the example cell-centered scheme there are three component weights (W^x_{i0} , W^y_{i0} , W^z_{i0}) for each of the faces of cell c_0 . The gradient at the cell center is then computed by multiplying the weighting factors by the difference vector $\Delta\phi$.

$$(\phi_x)_{c_0} = \sum_{i=1}^n W^x_{i0} \cdot (\phi_{ci} - \phi_{c_0}), \quad (\text{B.5})$$

$$(\phi_y)_{c_0} = \sum_{i=1}^n W^y_{i0} \cdot (\phi_{ci} - \phi_{c_0}), \quad (\text{B.6})$$

$$(\phi_z)_{c_0} = \sum_{i=1}^n W^z_{i0} \cdot (\phi_{ci} - \phi_{c_0}), \quad (\text{B.7})$$

where $(\phi_x)_{c_0}$ is the x component of the cell-centered value, W^x_{i0} is the x component weight, ϕ_{ci} is the cell-centered value of the adjacent cell, ϕ_{c_0} is the cell-centered value of the current cell, $(\phi_y)_{c_0}$ is the y component of the cell-centered value, W^y_{i0} is the y component weight, $(\phi_z)_{c_0}$ is the z component of the cell-centered value, and W^z_{i0} is the z component weight (Fluent 2006).

Temporal Discretization

A first order implicit differentiation scheme was used for the temporal discretization for the numerical solution. This scheme involves evaluation of the functional terms at the next time level as described by the following

$$\frac{\phi^{n+1} - \phi^n}{\Delta t} = F(\phi^{n+1}), \quad (\text{B.8})$$

where ϕ^{n+1} is the value at the future time step, ϕ^n is the value at the current time step, Δt is the time step size, and $F(\phi^{n+1})$ is the function evaluated at the future time step. The advantage of this method is that it produces an unconditionally stable solution regardless of time step size but requires a greater memory requirement to invert the large coefficient matrices. Despite the unconditional stability, care must be taken to ensure an accurate solution to the problem at hand. If the time step is too large, the physics of the problem are missed yielding a solution unrepresentative of the problem (Fluent 2006).

User-Defined Function for Scalar Transport

In order to model the transport of a passive scalar through a prescribed system, a user-defined function was developed for the scalar diffusivity coefficient given by the following

$$\Gamma_{eff} = \kappa + \frac{\nu_t}{Sc_t}, \quad (\text{B.9})$$

where Γ_{eff} is the effective diffusivity coefficient as defined in the scalar transport equation, κ is the molecular diffusivity, ν_t is the turbulent viscosity, and Sc_t is the turbulent Schmidt (or Prandtl) number. Equation B.9 was coded in the C programming language using the following script for use in the computational models.

```

/*****
UDF that computes diffusivity for mean age using a user-defined scalar.
*****/
#include "udf.h"
DEFINE_DIFFUSIVITY(diff,c,t,i)
{
return C_MU_T(c,t) / 0.7+0.001;
}

```

APPENDIX C

Grid Independence Studies of Computational models

This document contains the results of the grid independence studies to ensure solution convergence of the respective computation models. The initial meshes created in ANSYS Meshing were refined using FLUENT by adapting the volume of each cell. Because of the non-uniform tetrahedral mesh, the progression of refinement may appear random despite their being a sense of order in refining the cell volume by 10 percent of the maximum for each level.

Pipe Loop System

The original mesh using the automated procedure in ANSYS Meshing contained 895,950 unstructured tetrahedral cells. This mesh produced results which compared closely with the experimental data for all design flow rates. To ensure solution convergence, the mesh was refined once to 1,569,116 unstructured tetrahedral cells. Table C.1 and Figure C.1 contain the results of these two grids for an operational flow rate of 0.001093 m³/s.

Table C.1 Grid refinement parameters for pipe loop system operating at 0.001093 m³/s (16 gpm).

No. of Cells	t₁₀ (s)	t₉₀ (s)	BF	t₁₀/t₉₀	Flow Rate (m³/s)
895,950	1584	1890	0.94	0.84	0.001093
1,569,116	1541	1877	0.92	0.82	0.001093

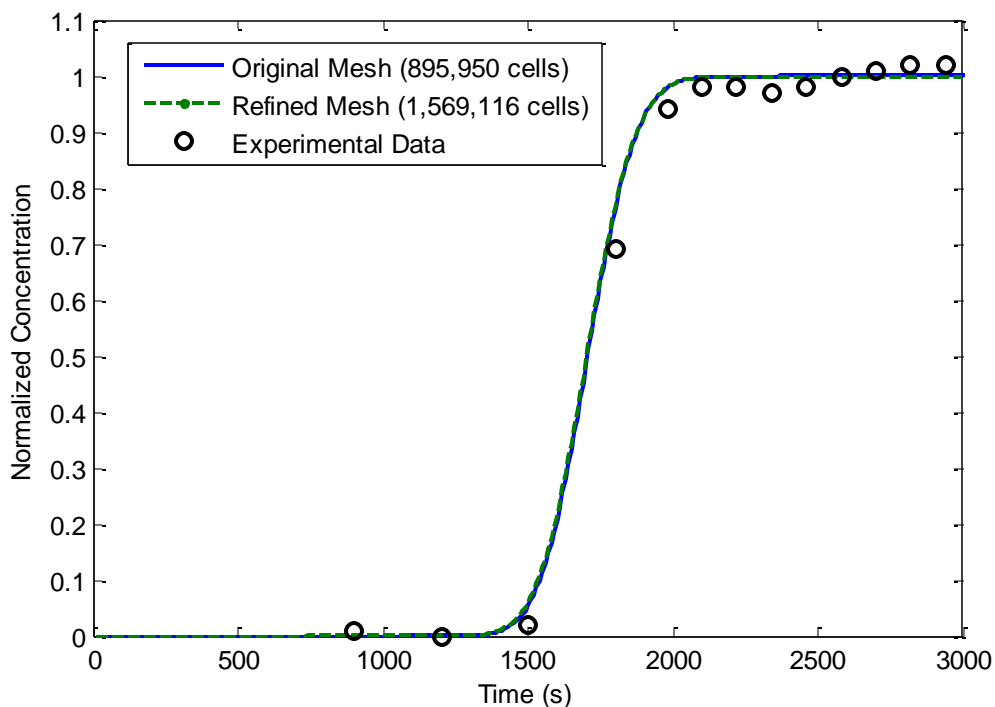


Figure C.1 Comparison of RTD curves for differing levels of grid refinement for pipe loop system operating at 0.001093 m³/s (16 gpm).

The refined grid did not significantly alter the computational model behavior thus the grid of 895,950 cells was used to expedite model results without sacrificing accuracy.

Pressurized Tank Systems

The original mesh of the 3 series tank system was 2,103,527 unstructured tetrahedral cells as produced in the automated procedure in ANSYS Meshing. The grid was refined once to 3,824,967 unstructured tetrahedral cells. Table C.2 presents the tabulated data for the original and refined meshes. Figure C.2 presents a graphical comparison of the RTD curves produced from these different meshes at an operational flow rate of 0.001262 m³/s.

Table C.2 Grid refinement parameters for 3 series tank configuration operating at 0.001262 m³/s (20 gpm).

No. of Cells	t ₁₀ (s)	t ₉₀ (s)	BF	t ₁₀ /t ₉₀	Flow Rate (m ³ /s)
2103527	54	624	0.22	0.09	0.001262
3824967	43	607	0.17	0.07	0.001262

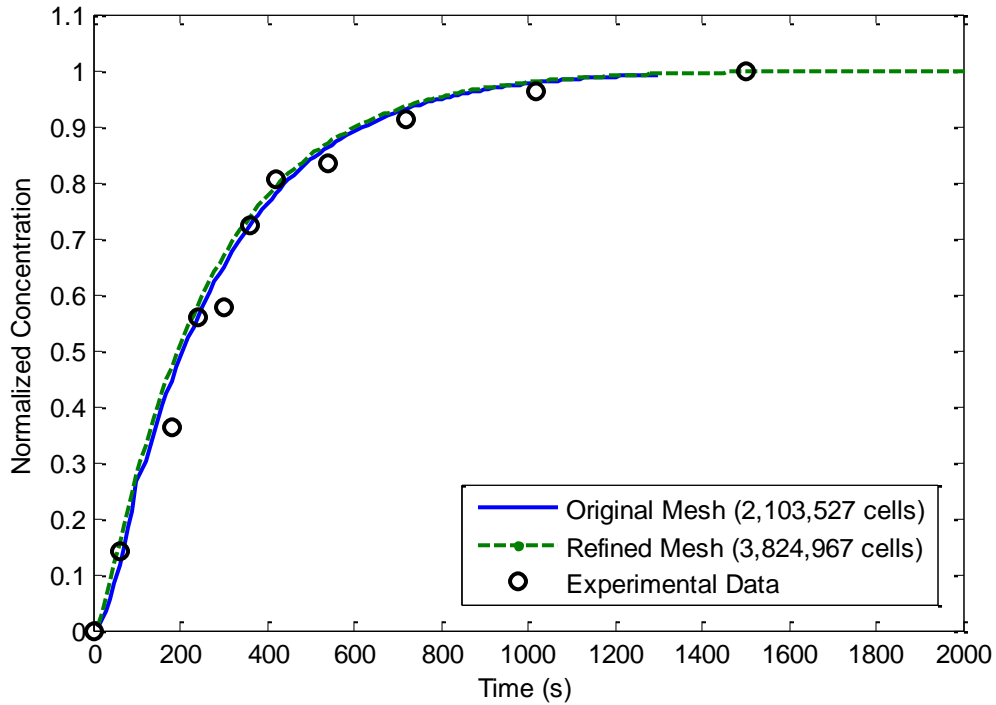


Figure C.2 Comparison of RTD curves for differing levels of grid refinement for 3 series tank configuration operating at 0.001262 m³/s (20 gpm).

The original mesh of the 6 series tank system was 1,810,567 unstructured tetrahedral cells as produced in the automated procedure in ANSYS Meshing. The grid was refined once to 3,961,820 unstructured tetrahedral cells. Table C.3 presents the tabulated data for the original and refined meshes. Figure C.3 presents a graphical comparison of the RTD curves produced from these different meshes at an operational flow rate of 0.001893 m³/s.

Table C.3 Grid refinement parameters for 6 series tank configuration operating at 0.001893 m³/s (30 gpm).

No. of Cells	t ₁₀ (s)	t ₉₀ (s)	BF	t ₁₀ /t ₉₀	Flow Rate (m ³ /s)
1810567	400.5	1328	0.60	0.30	0.001893
3961820	398.2	1321	0.60	0.30	0.001893

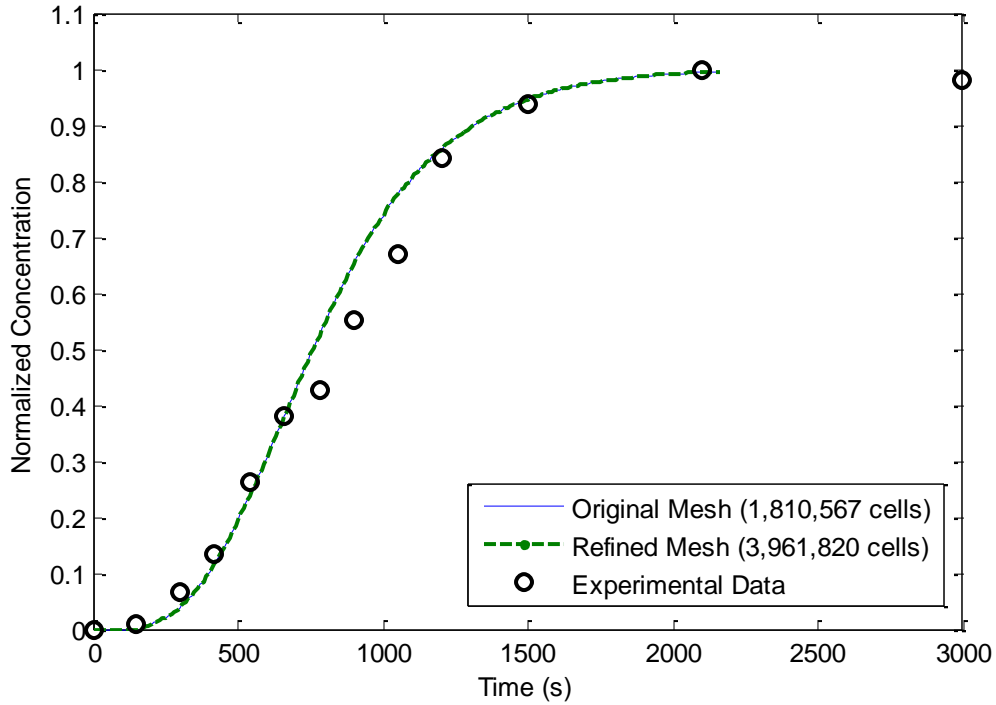


Figure C.3 Comparison of RTD curves for differing levels of grid refinement for 6 series tank configuration operating at 0.001893 m³/s (30 gpm).

Open Surface Tank Systems

The original mesh for the vertical open surface tank contained 152,439 unstructured tetrahedral cells again using the automated feature within ANSYS Meshing. The grid was refined once to 620,956 unstructured tetrahedral cells. Table C.4 presents the tabulated data for the original and refined meshes. Figure C.4 presents a graphical comparison of the RTD curves produced from these different meshes at an operational flow rate of 0.000316 m³/s.

Table C.4 Grid refinement parameters for vertical open surface tank system operating at 0.000316 m³/s (5 gpm).

No. of Cells	t ₁₀ (s)	t ₉₀ (s)	BF	t ₁₀ /t ₉₀	Flow Rate (m ³ /s)
152,439	771.3	15492.8	0.13	0.05	0.000316
620,956	815.2	15040.0	0.14	0.05	0.000316

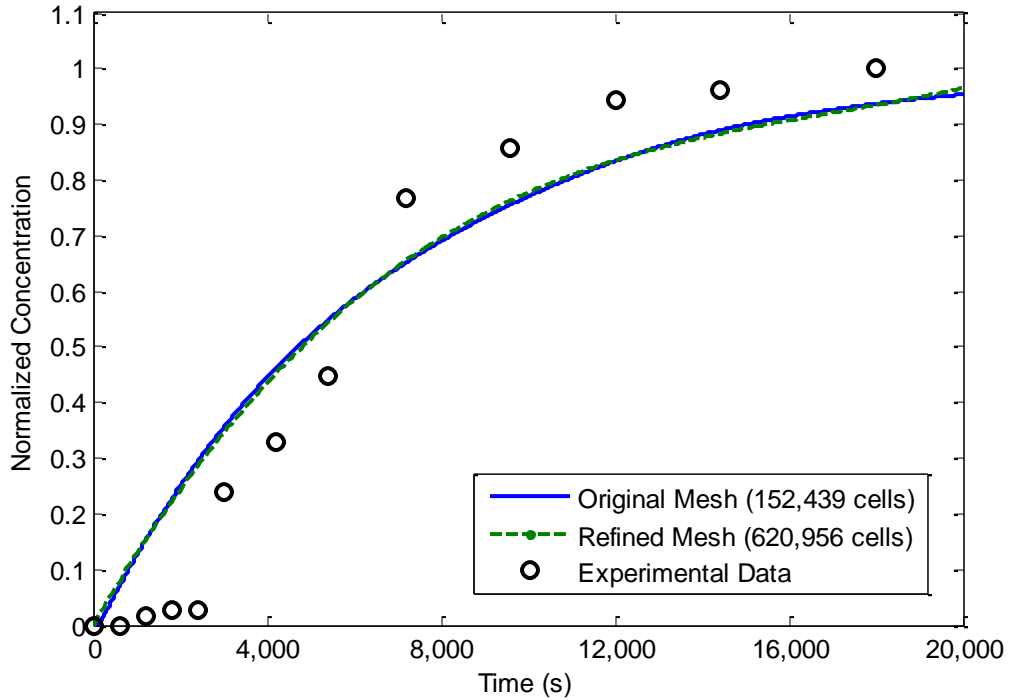


Figure C.4 Comparison of RTD curves for differing levels of grid refinement for vertical open surface tank system operating at 0.000316 m³/s (5 gpm).

The refined grid did not significantly alter the computational model behavior thus the grid of 152,439 cells was used to expedite model results without sacrificing accuracy.

The original mesh for the horizontal open surface tank contained 173,378 unstructured tetrahedral cells again using the automated feature within ANSYS Meshing. The grid was refined once to 781,209 unstructured tetrahedral cells. Table C.5 presents the tabulated data for the original and refined meshes. Figure C.5 presents a graphical comparison of

the RTD curves produced from these different meshes at an operational flow rate of $0.000631 \text{ m}^3/\text{s}$.

Table C.5 Grid refinement parameters for horizontal open surface tank system operating at $0.000631 \text{ m}^3/\text{s}$ (10 gpm).

No. of Cells	t_{10} (s)	t_{90} (s)	BF	t_{10}/t_{90}	Flow Rate (m^3/s)
173,378	950.4	17,127.5	0.15	0.06	0.000631
781,209	852.6	16,689.2	0.14	0.05	0.000631

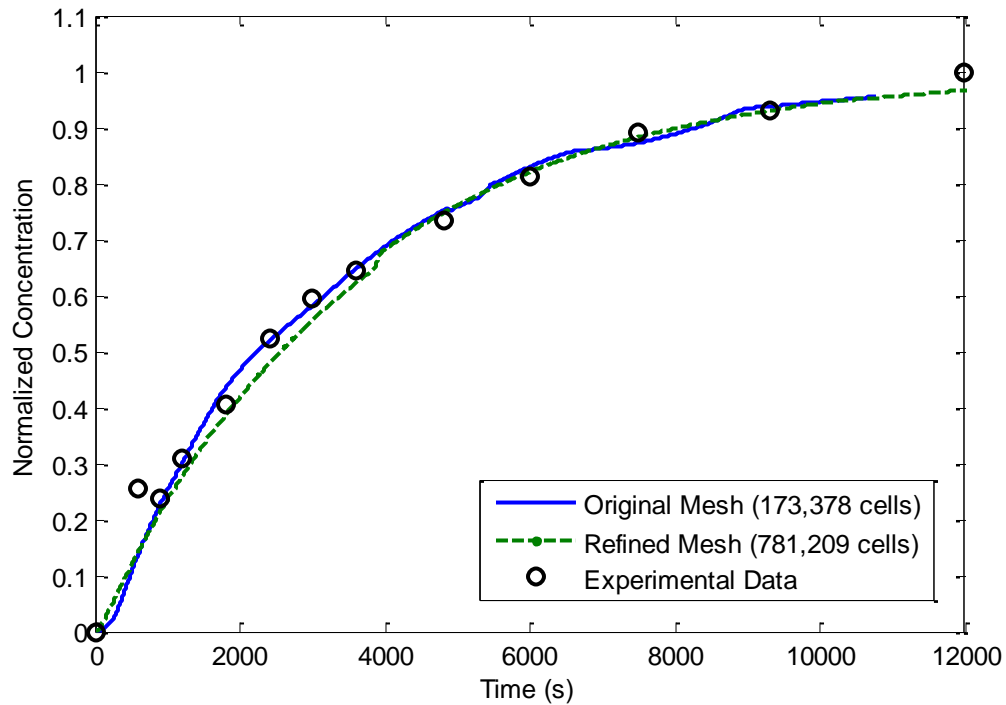


Figure C.5 Comparison of RTD curves for differing levels of grid refinement for horizontal open surface tank system operating at $0.000631 \text{ m}^3/\text{s}$ (10 gpm).

The refined grid did not significantly alter the computational model behavior thus the grid of 173,378 cells was used to expedite model results without sacrificing accuracy.

Baffled Tank System

Qing Xu performed an extensive grid independence study for her computational model and can be found in her Masters Thesis *Internal Hydraulics of Baffled Disinfection Contact Tanks Using Computational Fluid Dynamics*.

APPENDIX D

Hydraulic model of pressurized tank systems

Introduction

The objective of this model is to accurately predict the local losses in a system of vertical 80 gallon tanks in series. These tanks are connected to a water supply that flows at a constant rate. The flow first passes through a static mixer, then a multi-jet flow meter and finally through one tank, out the top of the tank and down to another tank. Throughout this journey the water flows through several threaded unions, open ball valves, and tees. This model is designed to predict the pressure loss of the water as it flows through various number of tanks.

Theory

Local losses in pressure are those that are due to bents, joints, valves and other various fittings. In turbulent flow the head loss past a particular fitting varies as the square of the velocity. This equation is given as:

$$h_L = k \cdot \frac{(Q/A)^2}{2g}, \quad (\text{D.1})$$

where h_L is the head loss, k is the loss coefficient, Q is the flow rate of water, A is the cross sectional area of the pipe, and g is the acceleration due to gravity.

The factor that varies from fitting to fitting is the local loss coefficient given to that particular type of fitting. For instance, an open ball valve would have a coefficient of 0.05 while a closed ball valve has a coefficient of 1. Many of these coefficients are well known and are available for reference while others, for the tanks and rotometers for instance are not available and are difficult to calculate. The pressure losses over the tanks,

rotometers and static mixer are found experimentally by measuring the pressure losses over various flows.

The friction losses in the system can be approximated using the Darcy-Weisbach equation. It is given as:

$$h_{L \text{ friction}} = f \frac{l V^2}{D 2g}, \quad (\text{D.2})$$

where $h_{L \text{ friction}}$ is the frictional head loss of the pipe, f is the friction factor, l is the length of the pipe, D is the diameter of the pipe, V is the velocity of the fluid, and g is the acceleration due to gravity.

The friction factor for this equation can be approximated using the Colebrook formula. It is given as:

$$\frac{1}{\sqrt{f}} = -1.8 \log \left[\left(\frac{\epsilon/D}{3.7} \right)^{1.11} + \frac{6.9}{Re} \right], \quad (\text{D.3})$$

where f is the friction factor, ϵ is the relative roughness of the pipe, D is the diameter of the pipe, and Re is the Reynolds number.

Equipment and Materials

1. Tank system setup - specifically three tanks in series with rotometers at the top and all the necessary pipes and fittings in order to connect the tanks.
2. A manometer that is capable of finding a pressure differential with a one hundredth of a psi precision.

3. A variable flowrate water source.

Procedure

To begin, the pipe system was set up in a way that it travels up and past all three tanks then down again to the drain. The manometer was attached at two spots, the first right before the static mixer, and the second right past the point where the third tank would normally be. The flow was set at a relatively low rate and adjusted slightly up in increments, each time noting the flowrate from the multi-jet flow meter and the pressure differential. These data points are then plotted and a curve fit performed in order to predict the pressure loss for any given flowrate. These pressure losses will be called the bypass pressure losses.

Next, the flow was directed through a single tank and the manometer was attached identically to the way it was for the bypass pressure loss test. The same steps were followed in order to create a curve of the pressure loss for any given flow rate. The pressure loss from the bypass prediction points were then subtracted from the tank pressure loss points in order to create a single curve that reflects only the pressure loss due to the tank and not its surrounding system. This was repeated for flows through two and three tanks as well.

Next, the rotometer was removed from the top of the tank that was tested previously and replaced by a straight pipe. The pressure differential was then measured the same way over various flow rates. A curve was constructed from these data points and this time the

tank pressure loss curve was subtracted so that the final curve reflected only the loss due to the rotometer.

The last step in the empirical determination of the pressure loss was to remove the static mixer and replace it with a straight section of pipe and route the flow through the bypass. The pressure taps were attached similarly to the bypass taps and the differential pressure was taken over several flow rates. Again, a curve was produced and was subtracted from the predicted values for the bypass pressure differentials at these points, leaving only the pressure loss due to the static mixer.

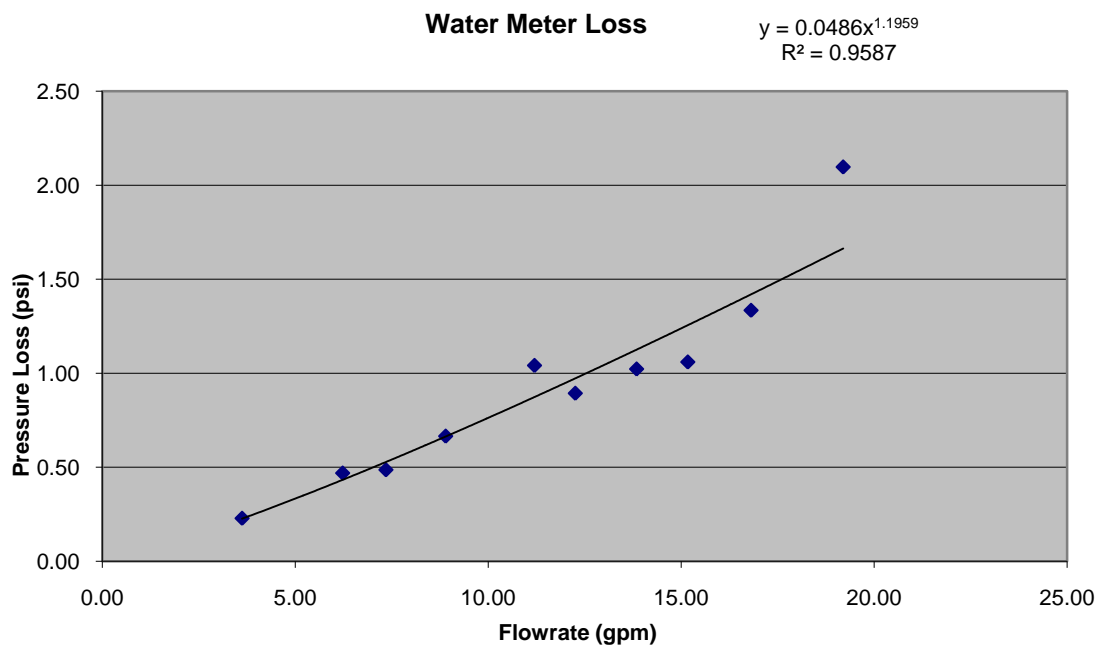
The model was created by first measuring all of the fittings and their distances from one another, making sure to include the diameters and the proper sequence of fittings. These fittings were listed out and all but the tank, rotometer, and static mixer were given a known loss coefficient and diameter. The local loss equation then can, from the flowrate, determine the pressure loss across each fitting. For the tank, rotometer, and static mixer, the pressure loss was found by using the second degree polynomial equation with its intercept at zero that fit each of their pressure loss curves the best.

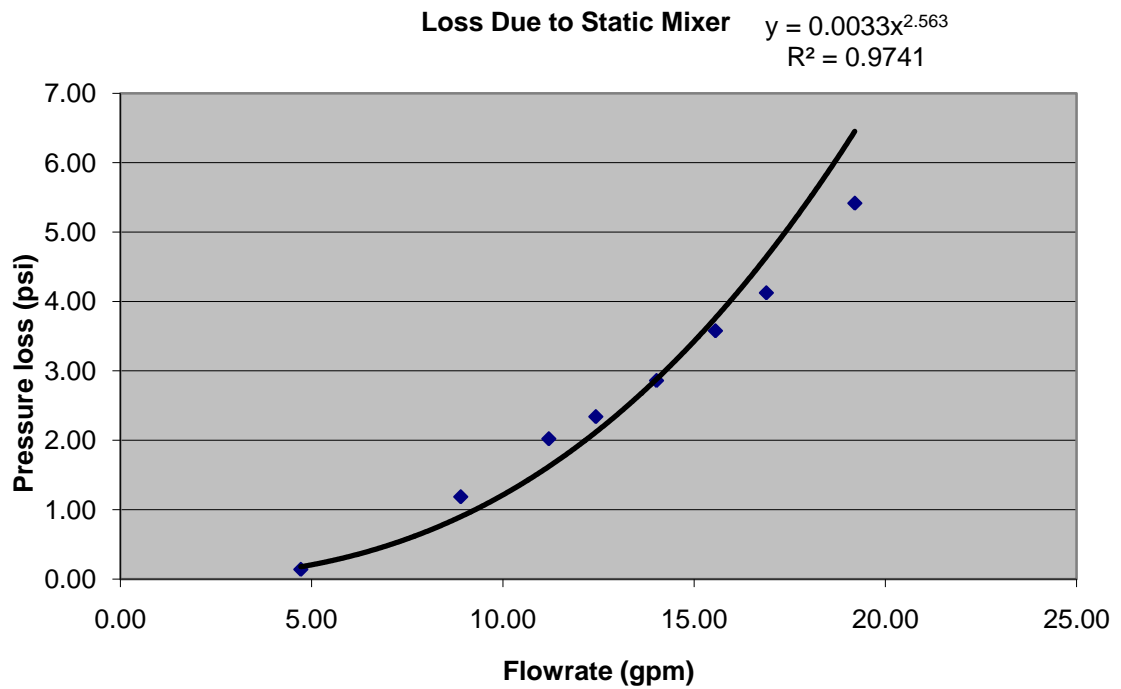
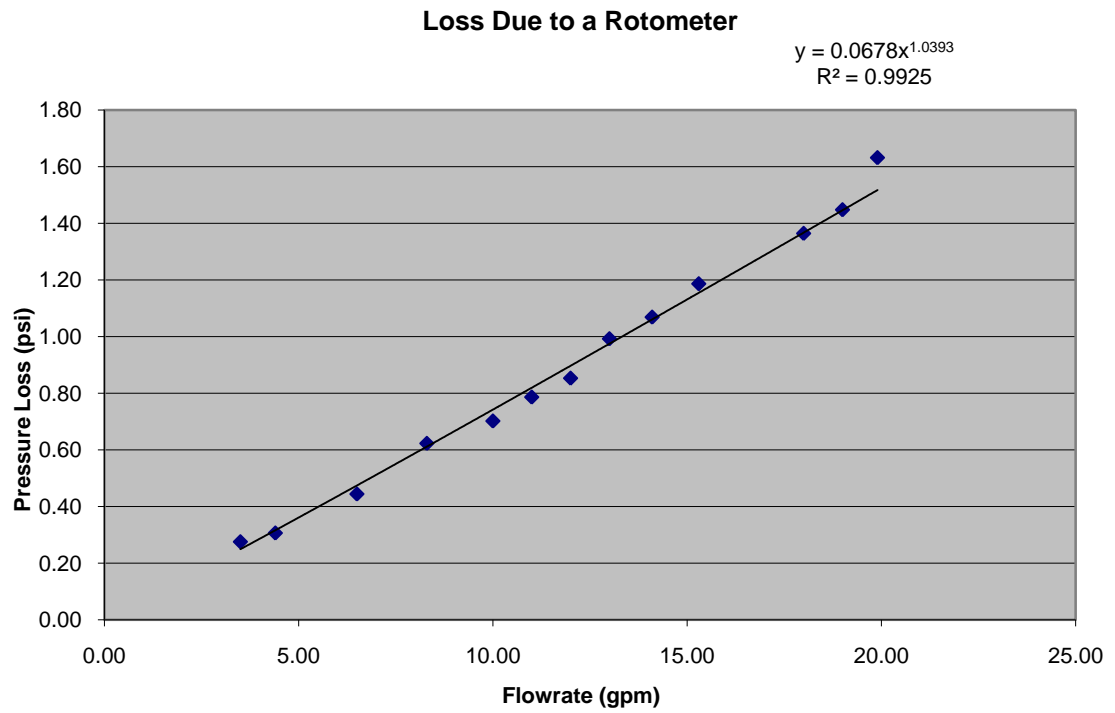
The losses due to friction were calculated in the model using the Colebrook formula and the Darcy-Weisbach equation. The dynamic viscosity that is used for the Reynolds number was determined by interpolation between known values for a dynamic viscosity for a given temperature.

Assumptions

This model works under the following assumptions. First, that the flow through the system is fully turbulent so that the local loss equation is valid. Second, the loss coefficients found accurately describe the loss of a particular fitting. Thirdly, it is assumed that the relative roughness of the PVC pipe is 0.0000015 m (or 0.000005 ft). Fourthly, it is assumed, for the friction loss calculations, that the diameter of the pipe remains constant at 0.03175 m. Fifth, the friction losses inside the tank, rotometer, and static mixer would be accounted for using the empirical method employed.

Results





Determination of the losses through these system components allowed for the computation of the losses seen through the tanks as seen in chapter 3.

APPENDIX E

Standard Operating Procedure (SOP) for conservative tracer analysis of small public
water disinfection systems

PURPOSE
<p>The purpose of this SOP is to layout a protocol for tracer studies on small scale contact tank facilities.</p>
SUMMARY
<p>The SOP describes the step necessary to perform a tracer study using lithium and fluoride conservative tracers on small water systems.</p> <p>There are two most common methods of tracer addition employed in water treatment evaluations: the step-dose method and the slug-dose method.</p> <p>In general, the step-dose procedure offers the greatest simplicity. However, both methods are theoretically equivalent for determining T_{10}. While either method is acceptable for conducting drinking water tracer studies, each has distinct advantages and disadvantages with respect to tracer addition procedures and analysis of results. The choice of the method may be determined by site-specific constraints.</p> <p>If possible, tracer studies should be conducted on each segment to determine the T_{10} for each segment. In order to minimize the time needed to conduct studies on each segment, the tracer studies should be started at the last segment of the treatment train prior to the first customer and completed with the first segment of the system. Conducting the tracer studies in this order will prevent the interference of residual tracer material with subsequent studies.</p>
RELATED SOPs
<p>None</p>
HEALTH AND SAFETY

Lithium Chloride (LiCl)

Hazards

Potential Acute Health Effects: Hazardous in case of skin contact (irritant), of eye contact (irritant), of ingestion, or inhalation.

Potential Chronic Health Effects:

CARCINOGENIC EFFECTS: Not available

MUTAGENIC EFFECTS: Mutagenic for mammalian somatic cells. Mutagenic for bacteria and/or yeast.

TERATOGENIC EFFECTS: Classified POSSIBLE for human

DEVELOPMENTAL TOXICITY: Classified Reproductive system/toxin/female, Reproductive system/toxin/male [POSSIBLE].

Repeated or prolonged exposure is not known to aggravate medical condition

First Aid

Eye Contact: Get medical attention immediately. Flush eyes with plenty of water for at least 15 minutes, occasionally lifting the upper and lower eyelids.

Skin Contact: Get medical attention immediately. Immediately wash skin with soap and water for at least 15 minutes and remove contaminated clothing. Wash clothing before reuse.

Serious Skin Contact: Wash with soap and cover the contaminated skin with an anti-bacterial cream. Seek immediate medical attention.

Inhalation: Remove from exposure to fresh air immediately. If breathing is difficult, give oxygen. Get medical attention if symptoms appear.

Ingestion: Get medical attention immediately. Do not induce vomiting. If the victim is conscious and alert, give 2-4 cupfuls of milk or water. Never give anything to an unconscious person.

Accidental Release Measures

Dispose of spilled solid in waste disposal container and clean surface with water avoiding skin contact.

Sodium Fluoride (NaF)

Hazards

Potential Acute Health Effects: Hazardous in case of skin contact (irritant), of eye contact (irritant, corrosive), of ingestion, or inhalation. Slightly hazardous in case of skin contact (corrosive). Severe over-exposure can result in death.

Potential Chronic Health Effects:

CARCINOGENIC EFFECTS: A4 (Not classifiable for human or animal) by ACGIH, 3 (Not classifiable for human) by IRAC

MUTAGENIC EFFECTS: Mutagenic for mammalian somatic cells. Mutagenic for bacteria and/or yeast.

TERATOGENIC EFFECTS: Not available

DEVELOPMENTAL TOXICITY: Not available

The substance may be toxic to kidneys, lungs, the nervous system, heart, gastrointestinal tract, cardiovascular system, bones, and teeth.

Repeated or prolonged exposure to the substance can produce target organs damage.

Repeated exposure to a highly toxic material may produce general deterioration of health by an accumulation in one or many human organs.

First Aid

Eye Contact: Get medical attention immediately. Flush eyes with plenty of water for at least 15 minutes, occasionally lifting the upper and lower eyelids.

Skin Contact: Get medical attention immediately. Immediately wash skin with soap and water for at least 15 minutes and remove contaminated clothing. Wash clothing before reuse.

Serious Skin Contact: Wash with soap and cover the contaminated skin with an anti-bacterial cream. Seek immediate medical attention.

Inhalation: Remove from exposure to fresh air immediately. If breathing is difficult, give oxygen. Get medical attention if symptoms appear.


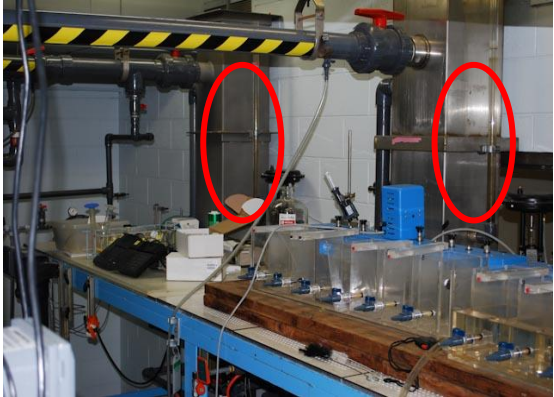
Serious Inhalation: Evacuate the victim to a safe area as soon as possible. Loosen tight clothing such as a collar, tie, belt, or waistband. Get immediate medical attention.

Ingestion: Get medical attention immediately. Do not induce vomiting. If the victim is conscious and alert, give 2-4 cupfuls of milk or water. Never give anything to an unconscious person.



Accidental Release Measures

Use appropriate tools to put spilled solid in waste disposal container.

PROCEDURE	
STEP NUMBER/NAME	VISUAL AID
1. Adjust flow rate for first desired analysis	Picture

<p>Adjust flow rate using PID controller or other control device</p>	 <p>PID Controller Interface</p>
<p>2. Verify flow rates</p>	<p>Picture</p>
<p>Verify the flow meter readings using drawdown columns</p>	 <p>Drawdown columns</p>
<p>3. Verify system volume and calculate HRT</p>	<p>N/A</p>
<p>Perform measurements as necessary.</p> $HRT = \frac{Volume}{Flow\ rate}$	
<p>4. Develop Sampling Protocol</p>	<p>N/A</p>

<p>The sampling protocol is largely dependent on the type of system analyzed</p> <ol style="list-style-type: none"> 1. For a pipe loop configuration (ie. plug flow), the sampling interval should be 30 seconds within ± 5 minutes of HRT and 5 minutes within ± 20 minutes of HRT 2. For baffled basin (ie. series tank), the sampling interval should be 5 minutes within ± 30 minutes of HRT and 10 minutes within ± 60 minutes of HRT 3. For open basin, the sampling interval should be 10 minutes with ± 90 minutes of HRT 	
<p>4. Determine injection and sampling points</p>	<p>Pictures</p>

<p>The injection point will be comprised of a 3/8 inch quick-connect fitting to accept the effluent hose from the injection pump.</p> <p>The sampling point should be easily accessible and contain a quarter-turn valve for ease of sampling</p>	 <p style="text-align: center;">Injection Point</p>  <p style="text-align: center;">Sampling Point</p>
<p>5. Determine background levels</p>	<p>N/A</p>
<p>Sample water prior to any tracer injection to determine the tracer solution concentration</p>	
<p>6. Set and calibrate injection pump</p>	<p>Picture</p>

- Fill bulk container with deionized water and attach to injection pump
- Attach effluent hose from injection pump to the system injection point
- Open valve to fill the calibration column, then close the valve
- Set pump stroke to 100 and speed to 80
- Turn pump on
- Open valve from calibration column to pump
- Time the drop in the column over a determine volume
- Turn off pump
- Calculate injection flowrate




Calibration Column





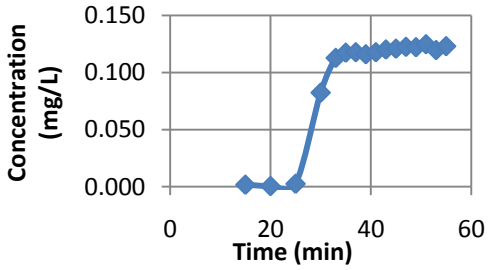
Injection pump

7. Prepare bulk tracer solution

Pictures

<ul style="list-style-type: none"> Determine the volume of tracer solution needed $Volume_{tracer} = Mean\ Resonance\ Time \times Injection\ Pump\ Rate$ Add the dry masses of <i>LiCl</i> and <i>NaF</i> to the determined volume of water in 7 and mix thoroughly 	 <p>Tracer Compounds in dry bulk form</p>
8. Determine the mass of <i>LiCl</i> added to tracer solution	N/A
<ul style="list-style-type: none"> Assume a system maximum of 0.04 mg/L based on background levels $\frac{0.04\ mg\ Li}{L} \times Volume_{system} = mass_{Li}$ $mass_{LiCl} = mass_{Li} \times \frac{42.394\ g\ LiCl}{6.941\ g\ Li}$ 	
9. Determine the mass of <i>NaF</i> added to tracer solution	N/A
<ul style="list-style-type: none"> Assume a system maximum of 1.00 mg/L based on background levels $\frac{mg\ F}{L} \times Volume_{system} = mass_F$ $mass_{NaF} = mass_F \times \frac{41.99\ g\ NaF}{18.998\ g\ F}$ 	
10. Add the dry masses of <i>LiCl</i> and <i>NaF</i> to the determined volume of water in 7 and mix thoroughly	N/A
11. Attach bulk tracer solution to injection pump	N/A
Attach the bulk tracer solution container to the inject pump and ensure that the valves are open allowing flow into the system	
12. Turn on injection pump	N/A

<p>Allow 2 minutes to pass before beginning to time for the sampling protocol. This allows for the DI water used to calibrate the pump to be flushed from the system</p>	
<p>13. Determine maximum tracer concentration in system</p>	<p>Picture</p>
<p>Sample at an intermediated point in the system well past the time estimated for the full concentration of the tracer to pass. This sample will provide the maximum tracer concentration in the system.</p>	<div data-bbox="1045 562 1276 1037" data-label="Image"> </div> <p data-bbox="974 1041 1344 1075">Intermediate Sampling Point</p>
<p>14. Sample according to protocol</p>	<p>N/A</p>
<ul style="list-style-type: none"> • Label containers appropriately • Place adequate sample in test tube for laboratory analysis of lithium • Place adequate sample in open container for on-site analysis of fluoride 	
<p>15. Analyze fluoride using Colormeter</p>	<p>Pictures</p>





<ul style="list-style-type: none"> • Place an adequate amount of DI water in an open container • Insert AccuVac sample and break off glass tip • Turn on colormeter • Program – 28 – enter • Remove colormeter cover, insert DI water AccuVac sample, replace cover, and press zero • Place new AccuVac into sample container, break off glass tip, press timer – enter on colormeter • When alarm sounds, remove colormeter cover, insert AccuVac sample, replace cover, press read, and record reading • Repeat steps for remaining samples 	<p>New AccuVac</p>  <p>Filled AccuVac</p> <p>AccuVac Samplers</p>  <p>DR890 Colormeter</p>																				
<p>16. Review results</p>	<p>Plot</p>																				
<p>Analyze colormeter fluoride results to ensure samples captured tracer breakthrough (RTD curve)</p>	 <table border="1"> <caption>Approximate data points from the RTD curve plot</caption> <thead> <tr> <th>Time (min)</th> <th>Concentration (mg/L)</th> </tr> </thead> <tbody> <tr><td>15</td><td>0.000</td></tr> <tr><td>20</td><td>0.000</td></tr> <tr><td>25</td><td>0.000</td></tr> <tr><td>30</td><td>0.080</td></tr> <tr><td>35</td><td>0.125</td></tr> <tr><td>40</td><td>0.125</td></tr> <tr><td>45</td><td>0.125</td></tr> <tr><td>50</td><td>0.125</td></tr> <tr><td>55</td><td>0.125</td></tr> </tbody> </table>	Time (min)	Concentration (mg/L)	15	0.000	20	0.000	25	0.000	30	0.080	35	0.125	40	0.125	45	0.125	50	0.125	55	0.125
Time (min)	Concentration (mg/L)																				
15	0.000																				
20	0.000																				
25	0.000																				
30	0.080																				
35	0.125																				
40	0.125																				
45	0.125																				
50	0.125																				
55	0.125																				
<p>17. Adjust sampling protocol (if necessary)</p>	<p>See Figure in 16.</p>																				
<p>If the RTD curve or a significant portion of the RTD curve are not captured, adjust the sampling to protocol</p>																					
<p>18. Repeat step 3-18 (if necessary)</p>	<p>See Figure in 16.</p>																				



Repeat these steps until an accurate RTD curve is captured	
19. Repeat steps 1-18	N/A
Repeat steps 1-18 for all considered flow rates	


APPENDIX F

Standard Operating Procedure (SOP) for conductivity analysis of small public water
disinfection systems

PURPOSE
<p>The purpose of this SOP is to layout a protocol for conductivity studies on small-scale contact tank facilities.</p>
SUMMARY
<p>The SOP describes the steps necessary to perform a conductivity study using NaCl on small water system using a step-dose method of introduction.</p> <p>There are two most common methods of tracer addition employed in water treatment evaluations: the step-dose method and the slug-dose method. In general, the step-dose procedure offers the greatest simplicity. However, both methods are theoretically equivalent for determining T_{10} and the determination of methods is often site specific depending upon available resources.</p>
RELATED SOPs
<p>Tracer Study Procedure (04-08-10)</p>
HEALTH AND SAFETY
<p>Sodium Chloride (NaCl)</p> <p><u>Hazards</u> May cause eye irritation.</p> <p>Not believed to present a significant hazard to health.</p>

PROCEDURE	
STEP NUMBER/NAME	VISUAL AID
1. Adjust flow rate for first desired analysis	(a) Rotameter and (b) Water meter
<p>Verify the flow rate using rotameter (if available) and/or water meter.</p> <p>Note: The accuracy of the rotameter is 2% of the full scale (or +/- 0.4 gpm) whereas the accuracy of the water meter is unknown</p>	<div style="display: flex; justify-content: space-around; align-items: center;"> <div style="text-align: center;">  <p>(a)</p> </div> <div style="text-align: center;">  <p>(b)</p> </div> </div>
2. Verify system volume and calculate HRT	N/A
<p>Perform measurements as necessary.</p> $HRT = \frac{Volume}{Flow\ rate}$	
3. Determine injection and sampling points	(a) Injection point and (b) sampling point
<p>The injection point is located immediately upstream of the static mixer and has a quarter-turn valve for operational ease.</p> <p>The sampling point is located immediately after the tank in consideration. Flexible tubing transports the flow to the bottom of the apparatus pictured in figure (b) and allows for the conductivity probe to be fully submerged.</p>	<div style="display: flex; justify-content: space-around; align-items: center;"> <div style="text-align: center;">  <p>(a)</p> </div> <div style="text-align: center;">  <p>(b)</p> </div> </div>
4. Determine background levels	N/A

<p>Turn on the conductivity meter and press [mode] until the [°C] is blinking indicating that the temperature compensated mode is turned selected.</p> <p>Place the conductivity probe in the sampling apparatus and open the sample tap allowing flow to pass over the probe. Record the baseline conductivity reading. Leave this assembly as is to record the conductivity measurements subsequent to step 9.</p>	
<p>5. Set and calibrate injection pump</p>	<p>(a) Calibration column and (b) injection pump</p>
<ul style="list-style-type: none"> • Fill bulk container with water and attach to injection pump • Attach effluent hose from injection pump to the system injection point • Open valve to fill the calibration column, then close the valve • Set pump stroke to 100 and speed to 80 • Turn pump on (using the breaker switch on the electrical plug outlet) • Open valve from calibration column to pump • Time the drop in the column over a determine volume • Turn off pump • Calculate injection flowrate 	<div style="display: flex; justify-content: space-around; align-items: center;"> <div style="text-align: center;">  <p>(a)</p> </div> <div style="text-align: center;">  <p>(b)</p> </div> </div>
<p>7. Prepare salt (NaCl) solution</p>	<p>N/A</p>

<p>For systems up to 550 US gallons, add 100 grams of NaCl to 1 gallon of water or until the stock solution reaches a conductivity of approximately 40 mS. Ensure that the NaCl is thoroughly mixed and does not accumulate significantly at the bottom of the stock solution bottle.</p>	
<p>8. Attach salt solution to injection pump</p>	<p>N/A</p>
<p>Attach the salt solution container to the injection pump and ensure that the valves are open allowing flow into the system. Turn on the injection pump allowing the salt solution to recirculate into the container until all air has been flushed from the system. Turn injection pump off.</p>	
<p>9. Attach injection pump to the system and begin conductivity study</p>	<p>Injection pump assembly connected to system inlet</p>
<p>Insert the feed line from the injection pump assembly into the system inlet. Open the valve. Simultaneously turn on the injection pump and start a timer, as the time is needed to incrementally record the conductivity readings to produce an RTD curve of the system.</p>	
<p>10. Record conductivity measurements</p>	<p>N/A</p>
<p>Record the conductivity readings and corresponding time of reading as appropriate. The system has effectively reached a steady state when readings vary +/- 0.1 μS over a 5-minute period.</p> <p>Note: Temperature readings are not necessary as the meter is in the temperature compensated mode.</p>	

<p>11. Repeat step 7-10 for same flow rate</p>	<p>N/A</p>																																										
<p>For consistency, ensure that the data from a minimum of 2 runs compare closely before testing the system at a different flow rate and/or different configuration.</p>	<p>The graph displays Normalized Conductivity on the y-axis (ranging from 0 to 1.1) against Time in minutes on the x-axis (ranging from 0 to 80). Two data series are plotted: Run 1 (blue line) and Run 2 (purple line). Both series follow a very similar sigmoidal curve, starting at 0 at time 0, rising steeply between 10 and 30 minutes, and leveling off to a plateau of approximately 0.95 after 40 minutes. The two lines are nearly indistinguishable, indicating high consistency between the two runs.</p> <table border="1"> <caption>Estimated data points from the graph</caption> <thead> <tr> <th>Time (min)</th> <th>Run 1 Normalized Conductivity</th> <th>Run 2 Normalized Conductivity</th> </tr> </thead> <tbody> <tr><td>0</td><td>0.00</td><td>0.00</td></tr> <tr><td>5</td><td>0.05</td><td>0.05</td></tr> <tr><td>10</td><td>0.15</td><td>0.15</td></tr> <tr><td>15</td><td>0.35</td><td>0.35</td></tr> <tr><td>20</td><td>0.55</td><td>0.55</td></tr> <tr><td>25</td><td>0.75</td><td>0.75</td></tr> <tr><td>30</td><td>0.85</td><td>0.85</td></tr> <tr><td>35</td><td>0.90</td><td>0.90</td></tr> <tr><td>40</td><td>0.93</td><td>0.93</td></tr> <tr><td>45</td><td>0.94</td><td>0.94</td></tr> <tr><td>50</td><td>0.95</td><td>0.95</td></tr> <tr><td>60</td><td>0.95</td><td>0.95</td></tr> <tr><td>70</td><td>0.95</td><td>0.95</td></tr> </tbody> </table>	Time (min)	Run 1 Normalized Conductivity	Run 2 Normalized Conductivity	0	0.00	0.00	5	0.05	0.05	10	0.15	0.15	15	0.35	0.35	20	0.55	0.55	25	0.75	0.75	30	0.85	0.85	35	0.90	0.90	40	0.93	0.93	45	0.94	0.94	50	0.95	0.95	60	0.95	0.95	70	0.95	0.95
Time (min)	Run 1 Normalized Conductivity	Run 2 Normalized Conductivity																																									
0	0.00	0.00																																									
5	0.05	0.05																																									
10	0.15	0.15																																									
15	0.35	0.35																																									
20	0.55	0.55																																									
25	0.75	0.75																																									
30	0.85	0.85																																									
35	0.90	0.90																																									
40	0.93	0.93																																									
45	0.94	0.94																																									
50	0.95	0.95																																									
60	0.95	0.95																																									
70	0.95	0.95																																									

APPENDIX G

Additional results for pressurized tank systems

This appendix contains additional plots showing the comparison of CFD and physical tracer study results depicting through RTD curves for both the 3 and 6 series pressurized tank systems. As mentioned in the text, the results for the tracer test for the 6 series system operating at $0.000946 \text{ m}^3/\text{s}$ were skewed because of a residual left in the system. The results of this error can be observed in Figures F.4 (a), (b), and (c).

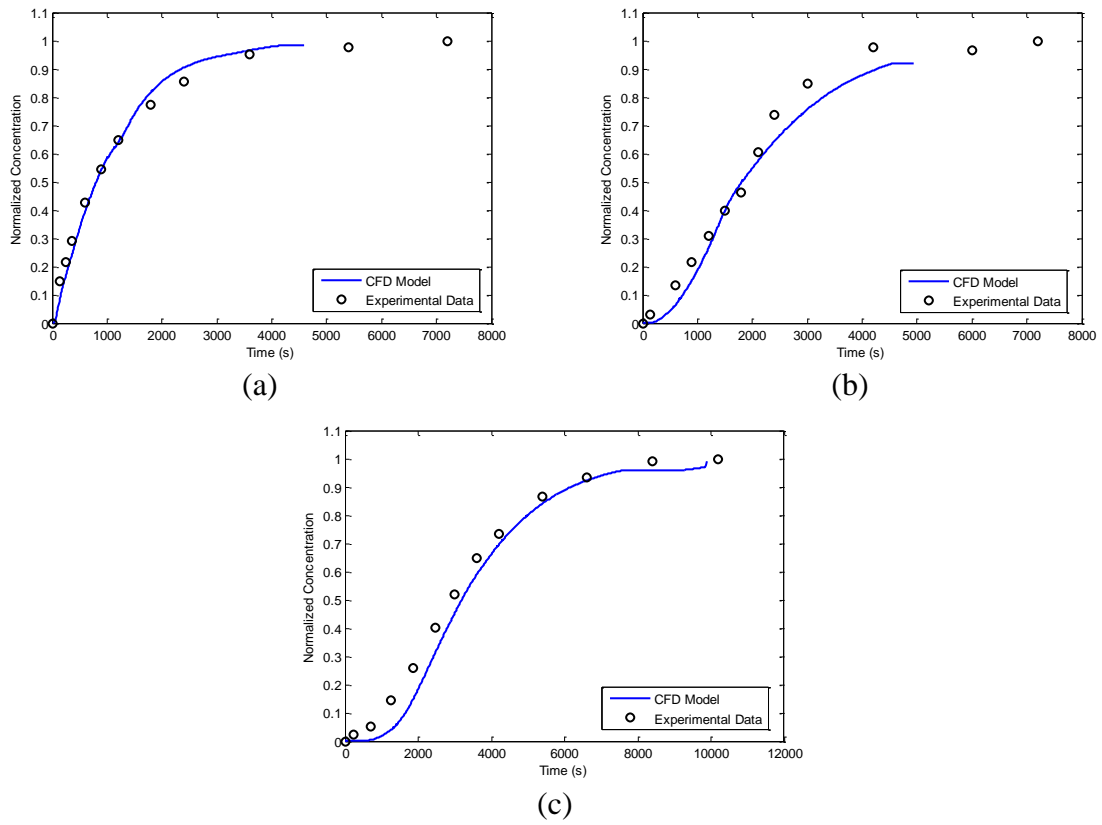


Figure F.1 Comparison of CFD model and tracer study RTD curves for $0.000316 \text{ m}^3/\text{s}$ (5 gpm) through (a) 1 tank, (b) 2 tanks and (c) 3 tanks in series.

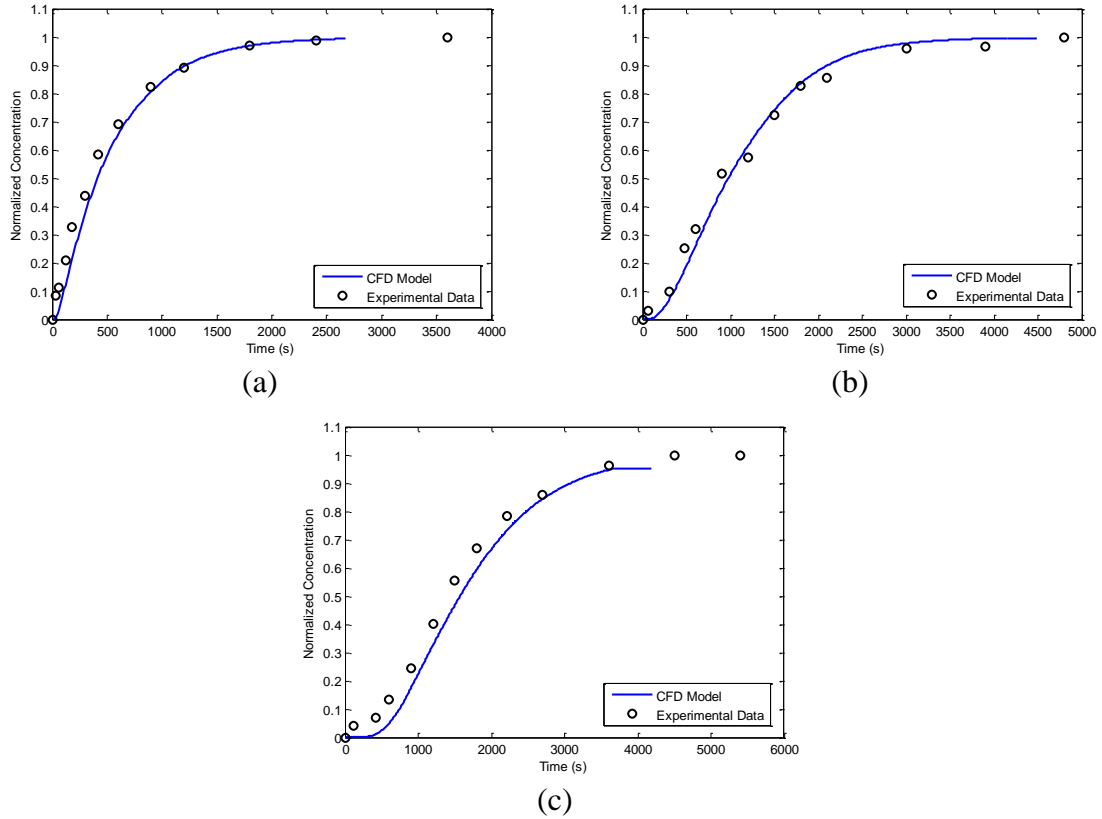


Figure F.2 Comparison of CFD model and tracer study RTD curves for $0.000631\text{m}^3/\text{s}$ (10 gpm) through (a) 1 tank, (b) 2 tanks and (c) 3 tanks in series.

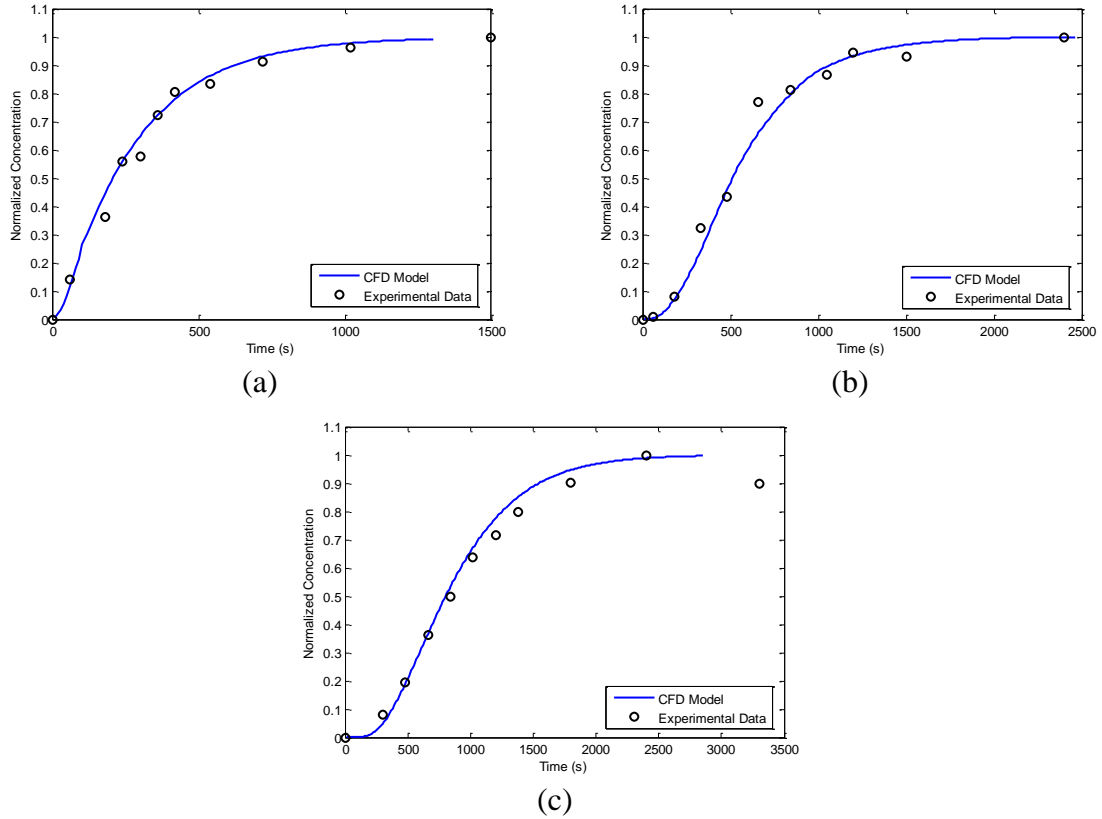


Figure F.3 Comparison of CFD model and tracer study RTD curves for 0.001262 m³/s (20 gpm) through (a) 1 tank, (b) 2 tanks and (c) 3 tanks in series.

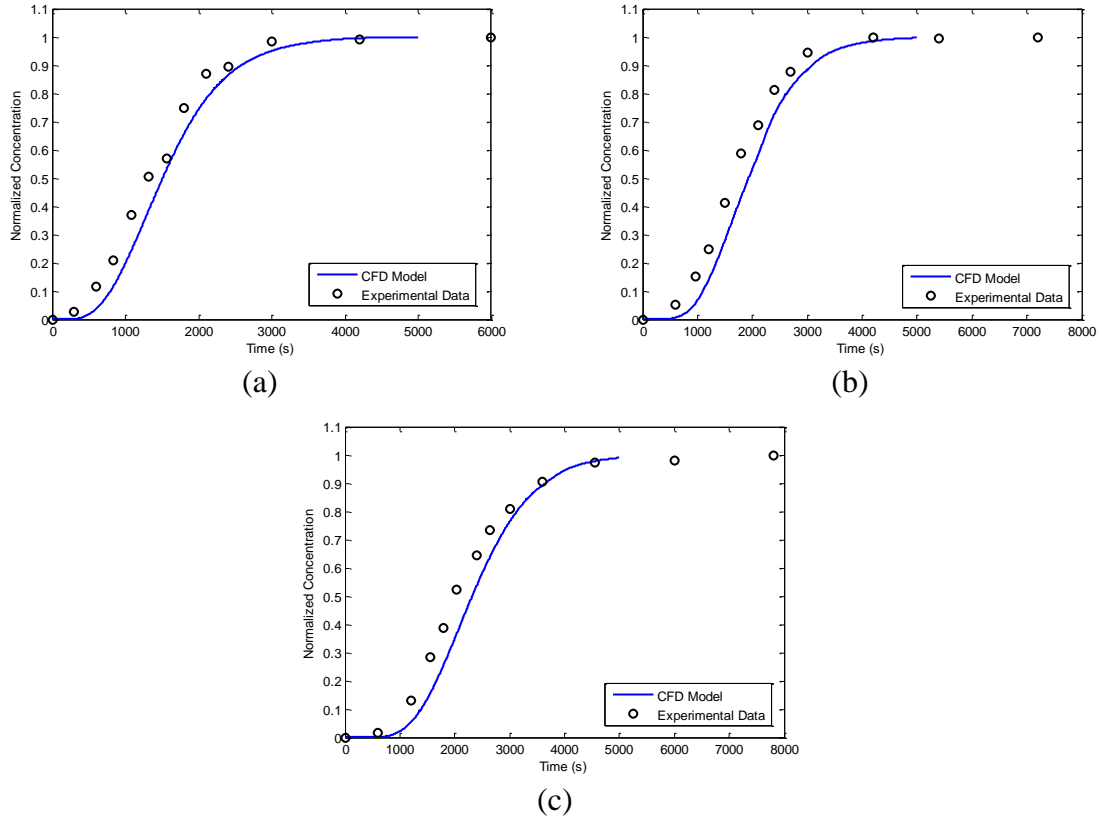


Figure F.4 Comparison of CFD model and tracer study RTD curves for $0.000946 \text{ m}^3/\text{s}$ (15 gpm) through (a) 4 tanks, (b) 5 tanks and (c) 6 tanks in series.

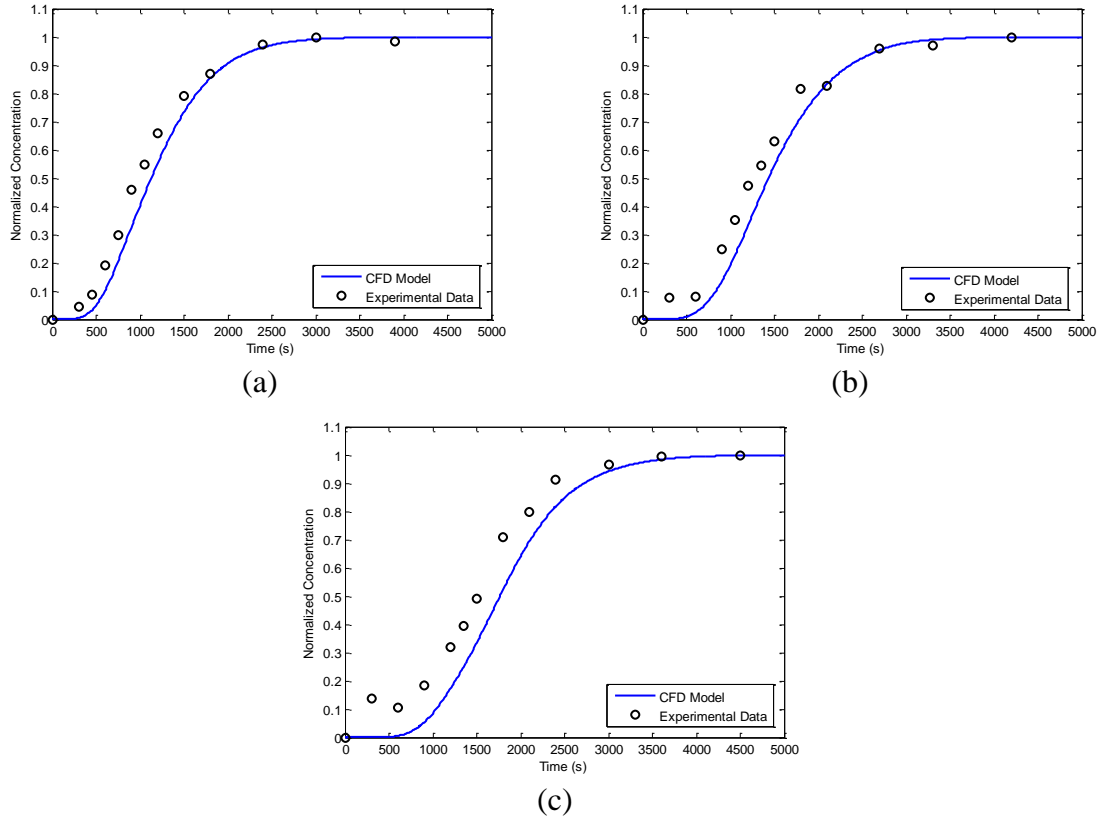


Figure F.5 Comparison of CFD model and tracer study RTD curves for 0.001262 m³/s (20gpm) through (a) 4 tanks, (b) 5 tanks and (c) 6 tanks in series

APPENDIX H

Sample pre-engineered small public water disinfection systems utilizing series
pressurized tank systems

The following pre-engineered pressurized series tanks systems were determined using the procedure described in the *LTIESWTR Disinfection Profiling and Benchmarking Technical Guidance Manual* in addition to the hydraulic efficiency data obtained through both physical tracer studies and CFD analysis of the prototype systems. These sample systems assume that the assumed BFs will remain constant over a range of tank volumes (primarily 40, 80, and 120 gallon tanks). In these systems the English systems of units is used.

The following gives a sample calculation to evaluate log inactivation for a series of 6 pressurized tanks with a chlorine residual of 0.7 mg/L, inflow temperature of 7°C, inflow pH between 6 and 9, and operational flow rate of 5 gpm.

$$\text{Virus log inactivation } (\geq 4) = \frac{CT}{CT_{99.99}}$$

where C is the free chlorine residual (mg/L), T , or t_{10} , is the contact time obtained from the product of BF and TDT (min), and $CT_{99.99}$ is the contact time required for 4-log inactivation (min).

For this example:

$$C = \mathbf{0.7 \text{ (mg/L)}}$$

$$T = BF * TDT = 0.65 * 96 \text{ (min)} = \mathbf{62.4 \text{ (min)}}$$

$$CT = \mathbf{43.7 \text{ (mg-min/L)}}$$

$$CT_{99.99} = \mathbf{7.2 \text{ (mg-min/L)}}$$

$$\frac{CT}{CT_{99.99}} = \frac{43.7 \text{ (mg} \frac{\text{min}}{\text{L}})}{7.2 \text{ (mg} \frac{\text{min}}{\text{L}})} = \mathbf{6.07}$$

The result of 6.07-log inactivation is greater than the required 4-log inactivation thus this system design for the given operation conditions is acceptable under the Ground Water Rule.

Pressurized Tank Systems	Temp. (°C)	7 to 12	Free Chlorine Residual	0.7 mg/L
Operational Flow Rate (gpm)	Number of Tanks in Series		Volume of Tanks (gal)	
5	4,5,6		120	
5	5,6		80	
10	6		120	

Pressurized Tank Systems	Temp. (°C)	7 to 12	Free Chlorine Residual	0.8 mg/L
Operational Flow Rate (gpm)	Number of Tanks in Series		Volume of Tanks (gal)	
5	4,5,6		120	
5	5,6		80	
10	6		120	

Pressurized Tank Systems	Temp. (°C)	7 to 12	Free Chlorine Residual	0.9 mg/L
Operational Flow Rate (gpm)	Number of Tanks in Series		Volume of Tanks (gal)	
5	4,5,6		120	
5	5,6		80	
10	6		120	

Pressurized Tank Systems	Temp. (°C)	7 to 12	Free Chlorine Residual	1.0 mg/L
Operational Flow Rate (gpm)	Number of Tanks in Series		Volume of Tanks (gal)	
5	4,5,6		120	
5	4,5,6		80	
5	6		40	
10	5,6		120	
10	6		80	

Pressurized Tank Systems	Temp. (°C)	7 to 12	Free Chlorine Residual	1.1 mg/L
Operational Flow Rate (gpm)	Number of Tanks in Series		Volume of Tanks (gal)	
5	4,5,6		120	
5	4,5,6		80	
5	6		40	
10	5,6		120	
10	6		80	

Pressurized Tank Systems	Temp. (°C)	7 to 12	Free Chlorine Residual	1.2mg/L
Operational Flow Rate (gpm)	Number of Tanks in Series		Volume of Tanks (gal)	
5	3,4,5,6		120	
5	4,5,6		80	
5	5,6		40	
10	4,5,6		120	
10	5,6		80	